NYS00488A
Submitted: June 9, 2015

NUREG/CR-7184
ANL-12/56

Crack Growth Rate and Fracture Toughness Tests on Irradiated Cast Stainless Steels

Y. Chen, B. Alexandreanu, and K. Natesan

Nuclear Engineering Division
Argonne National Laboratory

A. S. Rao, NRC Project Manager

Draft Manuscript: March 2014
Revised Manuscript: December 2014

ABSTRACT

Cast austenitic stainless steel, which has a ferrite-austenite duplex microstructure, is used in the cooling system of light water reactors for components with complex shapes, such as pump casings, valve bodies, and coolant piping. In the present study, crack growth rate and fracture toughness J-R curve tests were performed on irradiated cast stainless steels and unirradiated control samples in low-corrosion-potential environments (high-purity water with low dissolved oxygen or simulated pressurized water reactor) at 320°C. Both as-received and thermally aged materials were included to investigate the combined effect of thermal aging and irradiation embrittlement on the fracture behavior of cast stainless steels. The samples were irradiated to approximately 0.08 dpa at the Halden reactor. Good resistance to corrosion fatigue and stress corrosion cracking was observed for all cast stainless steel specimens. Thermal aging had little effect on the crack growth behavior at 0.08 dpa. Cleavage-like fracture was the dominant cracking morphology during the crack growth rate tests, and the ferrite phase was deformed to a lesser extent compared with the surrounding austenite phase. The fracture toughness results showed a dominant effect of neutron irradiation, and the fracture resistances were decreased considerably for all cast specimens regardless of their thermal aging. The reduction in fracture toughness was more significant in the unaged than thermally aged specimens. Nonetheless, the fracture toughness values of thermally aged specimens were 20-30% lower than their unaged counterparts, suggesting a combined effect of thermal aging and neutron irradiation in cast stainless steel.

FOREWORD

Cast austenitic stainless steel (CASS) is used in the cooling system of light water reactors for components with complex shapes, such as pump casings, valve bodies, coolant piping, control rod guide tubes and housing, etc. The ferrite phase is vulnerable to thermal aging embrittlement after long-term exposure to reactor coolant. In addition, neutron irradiation can decrease the fracture resistance of CASS significantly. It is suspected that a combined effect of thermal aging and irradiation embrittlement could reduce the fracture resistance even further to a level neither of these degradation mechanisms can impart alone.

In the early 1990s, NRC has conducted research on investigating the long term embrittlement of cast duplex stainless steels under LWR systems. Under those programs, experimental data was collected on the microstructure and the mechanical properties of cast steels were subjected to commercial and experimental heats as well as reactor aged cast steels (such as CF-3, CF-8 and CF-8M). The tests concluded that the chemical composition of the steels and the ferrite morphology strongly affect the kinetics of the embrittlement of steels. For example, while the low carbon cast steels (CF-3) are most resistant to embrittlement, the high carbon cast steels with molybdenum (CF-8M) are the most susceptible to embrittlement. The delta ferrite content of these steels ranged between 3 to 30%, and the steels containing > 5% ferrite ~~in the steels~~ have either a lacy or ~~acicular~~ vermicular ~~ferrite~~ morphology. The embrittlement in these steels was found to occur when the failure is dominated by brittle fracture that is associated with either cleavage of ferrite and or the separation of ferrite/austenite phase boundaries.

While the thermal aging embrittlement of CASS has been studied extensively, there are no data available at present with regard to the ~~synergistic~~ combined effect of thermal aging and irradiation embrittlement. In response to a 2009 request from the Office of Nuclear Regulatory Research, a test program has been initiated to investigate the joint effect of thermal aging and irradiation damage on the cracking susceptibility and fracture resistance of CASS.

Crack growth rate (CGR) and fracture toughness J-R curve tests were conducted on three grades of CASS (CF-3, CF-8 and CF-8M) containing high levels of delta ferrite (>23%). These samples were irradiated at the Halden reactor to a low dose of 0.08 displacements per atom (dpa). Both as-received (labeled as un-aged) and thermally aged specimens were investigated to determine the combined effect of thermal aging and irradiation embrittlement. The CGR tests were conducted in a low dissolved oxygen (DO) water environment or a pressurized water reactor (PWR) environment at 320°C. Following the CGR tests, the fracture toughness - J-R curve tests were performed on the same samples in the test environments.

The CASS materials showed good resistance to both corrosion fatigue and stress corrosion cracking (SCC) at the 0.08 dpa dose level. Trans-granular cleavage-like cracking was the dominant fracture mode during the CGR tests, and it was found that the extent of deformation of ferrite phase was significantly lesser than the surrounding austenite phase of the steel. The neutron irradiation even at low dose of 0.08 dpa significantly affected on the fracture toughness of both aged and un-aged CASS. The extent of irradiation-induced embrittlement is more evident in the un-aged than aged CASS alloys.

Brian Thomas, Director (Acting)
Division of Engineering

Office of Nuclear Regulatory Research

U.S. Nuclear Regulatory Commission

TABLE OF CONTENTS

Abstract iii
Foreword v
Figures ix
Tables xiii
Executive Summary xv
Acknowledgments xvii
Acronyms and Abbreviations xix
1 Introduction 1
2 Experimental 5
2.1 Materials and Specimens 5
2.2 Irradiation 7
2.3 Test Facility 9
2.4 Crack Growth Rate and Fracture Toughness J-R curve Tests 10
2.4.1 Crack Growth Rate Test 10
2.4.2 Fracture Toughness J-R curve Test 12
2.4.3 Fractographic Examination 14
3 Results 15
3.1 CF-3 Cast Stainless Steel 15
3.1.1 Unaged CF-3 CASS 15
3.1.2 Thermally Aged CF-3 CASS 44
3.2 CF-8 Cast Stainless Steel 67
3.2.1 Unaged CF-8 CASS 67
3.2.2 Thermally Aged CF-8 CASS 89
3.3 CF-8M Stainless Steel 111
3.3.1 Unaged CF-8M CASS 111
3.3.2 Thermally Aged CF-8M CASS 123
4 Discussion 135
4.1 Cyclic Crack Growth Rates 136
4.2 Constant-load Crack Growth Rates 139
4.3 Fracture Toughness 141
5 Summary 145
References 147

LIST OF FIGURES

1. Metallurgical images of the unaged and thermally aged CASS materials. 6
2. Schematic of 1/4T-CT specimen used in this study (red lines represent electrical leads). ... 7
3. Irradiation capsule of low-dose Halden irradiation. 8
4. Recirculation water loop for Cell 1 of the IML (items in red are safety significant components) 10
5. Schematic for inducing environmentally assisted cracking in test environment. 12
6. Crack-length-vs.-time plot for specimen A-N1 (unirradiated and unaged CF-3 with 24% ferrite): test periods (a) a-c, (b) d-j, (c) k-p, (d) q-u, (e) v-aa, and (f) 1 17
7. Cyclic CGRs of specimen A-N1. 19
8. The J-R curve for specimen A-N1. 20
9. Fracture surface of specimen A-N1 tested in low-DO high-purity water. 21
10. Fracture surface of specimen A-N1 along the sample central line. 22
11. Transgranular fracture in the precracking region of specimen A-N1. 23
12. Ductile dimple fracture in JR test region of specimen A-N1. 24
13. Crack-length-vs.-time plot for specimen A-1 (0.08-dpa unaged CF-3 with 24% ferrite): test periods (a) a-e, (b) f-j, (c) k-m, and (d) 1. 26
14. Cyclic CGRs of specimen A-1. 28
15. Fracture surface of specimen A-1 tested in PWR water 29
16. Fracture surface of specimen A-1 along the sample central line 30
17. Cleavage-like fracture in specimen A-1: (a) pre-cracking, and (b) end of the CGR test. Crack propagation from bottom to top 31
18. Fracture surface of specimen A-1 showing that delta ferrite deformed to a lesser extent than austenite. Crack propagation from bottom to top. 33
19. Crack-length-vs.-time plot for specimen A-2 (0.08-dpa unaged CF-3 with 24% ferrite) tested in low-DO high-purity water environment: test periods (a) a-e, (b) f-j, (c) k-o, (d) p-s, and (e) 1-2. 35
20. Cyclic CGRs of specimen A-2. 37
21. The J-R curve for specimen A-2. 38
22. Fracture surface of specimen A-2 tested in low-DO high-purity water. 39
23. Fracture surface of specimen A-2 along the sample central line 40
24. Cleavage-like steps at the beginning of CGR test of specimen A-2. Crack propagation from bottom to top. 41
25. Fracture surface of specimen A-2 showing that ferrite deformed to a lesser extent than austenite. Crack propagation from bottom to top. 42
26. Ductile dimple morphology in the JR test region of specimen A-2. Crack propagation from bottom to top. 43
27. Crack-length-vs.-time plot for specimen B-N1 (unirradiated, aged CF-3 with 24% ferrite) in PWR water: test periods (a) a-d, (b) e-h, (c) i-n, (d) o-s, (e) t-w, (f) x-aa, and (g) 1a-1b. 45
28. Cyclic CGRs of specimen B-N1. 48
29. The J-R curve for specimen B-N1 48

30. Fracture surface of specimen B-N1 tested in PWR water. 50
31. Fracture surface of specimen B-N1 along the sample central line. 51
32. Transgranular fracture in specimen B-N1 at the beginning of the precracking. Crack propagation from bottom to top. 52
33. Transgranular fracture in specimen B-N1 at the end of the precracking. Crack propagation from bottom to top. 53
34. Ductile dimple fracture in the JR test region of specimen B-N1. Crack propagation from bottom to top. 54
35. Crack-length-vs.-time plot for specimen B-1 (0.08-dpa aged CF-3 with 24% ferrite) in PWR water: test periods (a) a-e, (b) f-k, (c) l-u, (d) v-y, (e) z-ac, (f) ad-ag, (g) ah-al, and (h) am-1. 57
36. Cyclic CGRs of specimen B-1. 60
37. SCC CGRs of unaged and thermally aged CF-3 with 24% ferrite. 60
38. The J-R curve for specimen B-1. 61
39. Fracture surface of specimen B-1 tested in PWR water. 62
40. Fracture surface of specimen B-1 along the sample central line. 63
41. Deformation steps in the pre-cracking region of specimen B-1. Crack propagation from bottom to top. 64
42. Delta ferrite at dendrite cores in specimen B-1. Crack propagation from bottom to top. . 65
43. Fracture surface of specimen B-1 showing that delta ferrite is surrounded by heavily deformed austenite phase. Crack propagation from bottom to top. 66
44. Crack-length-vs.-time plot for specimen E-N1 (unirradiated, unaged CF-8 with 23% ferrite): test periods (a) a-c, (b) d-f, (c) g-i, (d) j-m, (e) n-q, (f) r-u, and (g) 1a-1b. 68
45. Cyclic CGRs of specimen E-N1. 71
46. J-R curve data of specimen E-N1. 72
47. Fracture surface of specimen E-N1 tested in low-DO high-purity water. 73
48. Transgranular fracture at the beginning of the precracking for specimen E-N1. Crack propagation from bottom to top. 74
49. Transgranular fracture at the end of the CGR test for specimen E-N1. Crack propagation from bottom to top. 75
50. Ductile dimple fracture in the JR test region of specimen E-N1. Crack propagation from bottom to top. 77
51. Crack-length-vs.-time plot for specimen E-1 (0.08-dpa unaged CF-8 with 23% ferrite): test periods (a) a-d, (b) e-f, (c) g-j, (d) k-o, and (e) p-2. 79
52. Cyclic CGRs of specimen E-1. 81
53. The J-R curve of specimen E-1. 82
54. Fracture surface of specimen E-1 tested in low-DO high-purity water. 83
55. Fracture surface of specimen E-1 along the sample central line. 84
56. Cleavage-like cracking at the beginning of the CGR test of specimen E-1. Crack propagation from bottom to top. 85
57. Cyclic CGR test region of specimen E-1. Crack propagation from bottom to top. 86

58. Smooth fracture surface at the end of the CGR test in specimen E-1. Crack propagation from bottom to top. 87
59. Ductile dimple fracture in the J-R test region of specimen E-1. Crack propagation from bottom to top. 88
60. Crack-length-vs.-time plot for specimen F-N1 (unirradiated, aged CF-8 with 23% ferrite): test periods (a) a-d, (b) e-h, (c) i-m, (d) n-q, and (e) 1a-1b. 90
61. Cyclic CGRs of specimen F-N1. 92
62. The J-R curve of specimen F-N1. 93
63. Fracture surface of specimen F-N1 tested in low-DO high-purity water. 94
64. Fracture surface of specimen F-N1 along the sample central line. 95
65. Transgranular fracture in the CGR test of specimen F-N1: (a) in the precracking region and (b) at the end of CGR test. Crack advance direction from bottom to top. 96
66. Transition region from CGR to J-R curve tests of specimen F-N1. Crack advance direction from bottom to top. 98
67. Ductile dimple fracture in the JR test region of specimen F-N1. Crack advance direction from bottom to top. 100
68. Crack-length-vs.-time plot for specimen F-1 (0.08-dpa aged CF-8 with 23% ferrite): test periods (a) a-f, (b) g-j, (c) k-m, and (d) 1. 102
69. Cyclic CGRs of specimen F-1. 103
70. SCC CGRs of unaged and aged CF-8 CASS with 23% ferrite. 104
71. The J-R curve of specimen F-1. 105
72. Fracture surface of specimen F-1 tested in low-DO high-purity water. 106
73. Fracture surface of specimen F-1 along the sample central line. 107
74. Fracture surface of the CGR region in specimen F-1. Crack propagation from bottom to top. 108
75. Deformation steps in austenite grain around ferrite phase in the CGR test region of specimen F-1. Crack propagation from bottom to top. 109
76. Dimple fracture in the JR test region of specimen F-1. Crack propagation from bottom to top. 110
77. Crack-length-vs.-time plot for specimen I-1 (0.08-dpa unaged CF-8M with 28% ferrite): test periods (a) a-f, (b) g-k, (c) l-o, (d) p-r, (e) s-v, (f) w-z, (g) aa-ac, and (h) 1.. 113
78. Cyclic CGRs of specimen I-1. 116
79. The J-R curve of specimen I-1. 116
80. Fracture surface of specimen I-1 tested in low-DO high-purity water. 118
81. Fracture surface of specimen I-1 along the sample central line. 119
82. Precracking region in the CGR test of specimen I-1. Crack propagation from bottom to top. 120
83. Fracture surface at the end of CGR test of specimen I-1. Crack propagation from bottom to top. 121
84. Heavily deformed microstructure in the JR test region of specimen I-1 122
85. Crack-length-vs.-time plot for specimen J-1 (0.08-dpa aged CF-8M with 28% ferrite): test periods (a) a-g, (b) h-n, (c) o-r, (d) s-u, (e) 1a-1b, and (f) 2a-2c. 124

86. Cyclic CGRs of specimen J-1. 127
87. SCC CGRs of unaged and aged CF-8M CASS, irradiated to 0.08 dpa. 127
88. The J-R curve of specimen J-1. 128
89. Fracture surface of specimen J-1 tested in low-DO high-purity water. 129
90. Fracture surface of specimen J-1 along the sample central line. 130
91. Precracking region of specimen J-1. Crack propagation from bottom to top. 131
92. Ferrite microstructure at the end of CGR test of specimen J-1. Crack propagation from bottom to top. 132
93. Cleavage-like fracture at the end of CGR test of specimen J-1. Crack propagation from bottom to top. 133
94. Fracture along ferrite at dendrite core in the JR test region of specimen J-1. Crack propagation from bottom to top. 134
95. Best-fit curves of cyclic CGRs at 0.08-dpa dose: (a) unaged and aged CF-3, (b) unaged and aged CF-8, and (c) unaged and aged CF-8M. 137
96. Fitting coefficient A for the corrosion fatigue superposition model. 139
97. Constant-load CGRs of the low-dose CASS with more than 23% ferrite in low-DO high-purity and PWR water environments. 140
98. Fracture toughness values of unirradiated and irradiated CASS in unaged and aged conditions. Note that most of the results are from 1/4T-CT specimens tested at ~320°C in water environments. The unirradiated results for CF-8M CASS are from 1T-CT specimens tested at ~290°C in an air atmosphere. 142

LIST OF TABLES

1. Chemical compositions of the cast stainless steels examined in this study. 5
2. Thermal aging conditions for the cast stainless steels in this study. 5
3. Test matrix of unirradiated and irradiated low-dose CASS specimens. 15
4. Crack growth rates of specimen A-N1 (unirradiated and unaged CF-3 with 24% δ ferrite) in low-DO high-purity water. 16
5. Crack growth rates of specimen A-1 (0.08-dpa unaged CF-3 sample with 24% δ ferrite) in PWR water. 25
6. Crack growth rates of specimen A-2 (0.08-dpa unaged CF-3 with 24% δ ferrite) in low-DO high-purity water environment. 34
7. CGR test of specimen B-N1 (unirradiated, thermally aged CF-3 with 24% δ ferrite) in PWR water. 44
8. CGR test of specimen B-1 (0.08-dpa aged CF-3 with 24% δ ferrite) in PWR water. 56
9. CGR test of specimen E-N1 (unirradiated, unaged CF-8 with 23% δ ferrite) in low-DO high-purity water. 67
10. CGR test of specimen E-1 (0.08-dpa unaged CF-8 with 23% δ ferrite) in low-DO high-purity water. 78
11. Crack growth rates of specimen F-N1 (unirradiated, aged CF-8 with 23% δ ferrite) in a low-DO high-purity water environment. 89
12. Crack growth rates of specimen F-1 (0.08-dpa aged CF-8 with 23% δ ferrite) in a low-DO high-purity water environment. 101
13. Crack growth rates of specimen I-1 (0.08-dpa unaged CF-8M with 28% δ ferrite) in a low-DO high-purity water environment. 112
14. Crack growth rates of specimen J-1 (0.08-dpa aged CF-8M with 28% δ ferrite) in a low-DO high-purity water environment. 123
15. CGR test results at ~320°C for CASS specimens with high ferrite contents. 135
16. Fracture toughness JR test results for CASS with high ferrite contents. 136

EXECUTIVE SUMMARY

Cast austenitic stainless steel (CASS) is used in the cooling system of light water reactors for components with complex shapes, such as pump casings, valve bodies, coolant piping, and control rod guide tube spacers. In contrast to a fully austenitic microstructure of wrought stainless steel (SS), CASS consists of a ferrite-austenite duplex microstructure. A certain amount of delta ferrite phase is intentionally designed into CASS and SS weld metals to engineer against hot cracking. However, the ferrite phase is vulnerable to thermal aging embrittlement after long-term exposure to reactor coolant. In addition, neutron irradiation can decrease the fracture resistance of CASS significantly. It is suspected that a combined effect of thermal aging and irradiation embrittlement could reduce the fracture resistance even further to a level neither of these degradation mechanisms can impart alone. While the thermal aging embrittlement of CASS has been studied extensively, no data are available at present with regard to the combined effect of thermal aging and irradiation embrittlement. A test program has been initiated to investigate the joint effect of thermal aging and irradiation damage on the cracking susceptibility and fracture resistance of CASS.

Crack growth rate (CGR) and fracture toughness J-integral resistance (J-R) curve tests were conducted on three grades of CASS (CF-3, CF-8, and CF-8M) containing high levels of delta ferrite (>23%). The samples were irradiated at the Halden reactor to a low dose of 0.08 displacements per atom (dpa) or 5.56×10^{19} n/cm^2 (E > 1 MeV). Both as-received and thermally aged specimens were included to determine the combined effect of thermal aging and irradiation embrittlement. The CGR tests were conducted at ~320°C on the irradiated and unirradiated control samples in a high purity water environment with low dissolved oxygen (DO) or a pressurized water reactor (PWR) environment. Following the CGR tests, the fracture toughness J-R curve tests were performed on the same samples in the test environments.

Cyclic CGRs and constant-load CGRs were measured to evaluate the corrosion fatigue and stress corrosion cracking (SCC) of the CASS specimens. In the cyclic CGR tests, environmental enhanced cracking was more difficult to establish in the CASS specimens than in wrought SSs. In SCC CGR tests, only moderate CGRs, in the range of 10^{-11} m/s, were recorded in most of the CASS specimens regardless of their thermal aging history. In general, the CASS materials showed good resistance to both corrosion fatigue and SCC without irradiation and at 0.08 dpa. Transgranular cleavage-like cracking was the dominant fracture mode during the CGR tests, and the ferrite phase was often deformed to a less extent compared with its surrounding austenite phase. This observation supports the hypothesis that the beneficial effect of ferrite for SCC resistance arises, in part, from the low plastic deformation of ferrite phase compared to austenite.

A previous study showed that the SCC CGRs of thermally aged CASS were one order of magnitude higher than those of unaged materials at high DO concentrations (>1 ppm). In contrast, a similar cracking behavior between thermally aged and unaged materials was observed for irradiated and unirradiated control specimens in the low-DO high-purity water and simulated PWR water. The lack of sensitivity to thermal aging history in these tests might be a result of the low-corrosion-potential environments employed. The effect of neutron irradiation on the SCC behaviors of CASS materials was not clear in the present study.

Neutron irradiation did significantly affect the fracture toughness of CASS. At 0.08 dpa, the fracture toughness values of unaged specimens were much lower than their initial unirradiated values. Fracture toughness was also reduced by 20-30% for thermally aged specimens after irradiation. This observation suggests an interaction between thermal aging and irradiation damage. When both conditions of thermal aging and irradiation damage are present, the combined effect is not a simple addition of both degradations. The interaction between thermal aging and irradiation damage can lead to different microstructural evolutions in CASS materials (viz. by prompting G-phase formation through radiation-induced segregations of minor elements), reducing the fracture resistance to a higher extent than either one of them can achieve alone. Neutron irradiation appears to affect not only the kinetics of thermal aging embrittlement, but also the lower bound values of fracture toughness (i.e., the saturation state). For this reason, the effects of neutron irradiation should be considered when the degree of thermal aging embrittlement is ~~being~~ evaluated for CASS components.

ACKNOWLEDGEMENTS

The authors would like to thank Drs. O. K. Chopra and W. J. Shack for their invaluable contribution to this project. Our special thanks go out to Ms. T. M. Karlsen, OECD Halden Reactor Project, Halden, Norway, for reactor irradiation experiments and sample transfer. L. A. Knoblich, E. E. Gruber, R. Clark, and E. J. Listwan of Argonne, Y. Yang of University of Florida, and J. Pakarinen and Y. Huang of University of Wisconsin-Madison are acknowledged for their contributions to the experimental effort. We are also grateful to Drs. R. Tregoning and W. J. Shack for their careful reviews and comments on the manuscript. This work is sponsored by the Office of Nuclear Regulatory Research, U.S. Nuclear Regulatory Commission, under Job Code N6519 and V6454; Program Manager: A. S. Rao.

ACRONYMS AND ABBREVATIONS

ASTM	American Society for Testing and Materials
BWR	Boiling Water Reactor
CASS	Cast Austenitic Stainless Steels
CGR	Crack Growth Rate
CT	Compact Tension
DCPD	Direct Current Potential Drop
DO	Dissolved Oxygen
ECP	Electrochemical Potential
HWC	Hydrogen Water Chemistry
IASCC	Irradiation-Assisted Stress Corrosion Cracking
IGSCC	Intergranular Stress Corrosion Cracking
IML	Irradiated materials Laboratory
J-R	J-Integral Resistance
LVDT	Linear Voltage Displacement Transducer
LWR	Light Water Reactor
NWC	Normal Water Chemistry
PPU	Periodical Partial Unloading
PWR	Pressurized Water Reactor
SCC	Stress Corrosion Cracking
SEM	Scanning Electron Microscopy
SS	Stainless Steel
TG	Transgranular

Units of Measure

°C	degrees centigrade
cm	centimeter
dpa	displacement per atom
hr	hour
J	joule
m	meter
mm	millimeter
MPa	megapascal
ppb	part per billion
ppm	part per million
psig	pound per square inch gauge
s	second
µ	micron

1 Introduction

Stainless steel is an important class of engineering materials used in light water reactors (LWRs). While the main structure of reactor core internals is constructed from wrought stainless steels (SSs), components with complex shapes, such as pump casings, valve bodies, coolant piping, elbows, and control rod guide tube spacers, are often made of cast austenitic stainless steels (CASS).[1] The CF grades of CASS whose compositions are similar to those of 300-series austenitic SSs are the most widely used corrosion-resistant CASS. The CF-3 and CF-8 grades contain nominal 19% Cr and 9% Ni and are the cast equivalents of Types 304L and 304 SSs, respectively. In addition, the CF-3M and CF-8M grades are the molybdenum-containing cast versions of 316L and 316 SSs, respectively. Like their wrought equivalents, the CF grades of CASS possess excellent corrosion resistance and mechanical properties,[2] and, thus, are ideal for LWR applications in aqueous environments. The strength and ductility of CF grades are comparable to those of wrought SSs. At room temperature, the yield and tensile strengths of CF-3 and CF-8 grades are greater than 200 MPa and 480 MPa,[3] respectively, similar to those of solution-annealed SSs. A good combination of strength and ductility also gives rise to excellent fracture toughness. Stable tearing occurs in CASS samples well above their yield strength before final fracture. Chopra and Sather[4] showed that the crack initiation toughness of CF-3 and CF-8 CASS varies from ~200 kJ/m^2 to over 1000 kJ/m^2 at room temperature; these values are comparable to those of wrought SSs reported by Mills.[5]

In contrast to the fully austenitic microstructure of wrought SSs, CASS consists of a ferrite-austenite duplex microstructure. It is common that a certain amount of δ ferrite is present along with austenite (γ) in the solidification microstructure such as CASS or weld metals. The precise fractions of ferrite and austenite phases depend on the chemical composition and casting thermal history. Experimental methods, such as quantitative metallography and ferromagnetic measurement, can be used to determine the ferrite content in CASS or weld metals.[6,7] Empirical models have also been developed to predict and control phase content with alloy composition. Based on the phase-stabilizing effects of Cr and Ni in Fe-Cr-Ni systems, several constitution diagrams have been established to estimate phase content.[8,9,10] The contributions of minor alloying elements are incorporated with Cr and Ni equivalent numbers and computed with empirical equations. The applicable range of composition, incorporated alloying elements, and weighing factors vary in these models, and thus the predicted phase contents differ among them to some extent.[11] For steel castings of CF grades, use of the Scheofer diagram, which is a modified version of the Schaeffler diagram[8], is recommended by the American Society for Testing and Materials (ASTM) for estimating ferrite content.[12]

The ferrite phase is critical for the mechanical properties and corrosion resistance of CASS and weld metals. Since hardening mechanisms by thermal-mechanical treatments cannot be easily implemented in castings, the strength of CASS mainly relies on the ferrite-austenite duplex microstructure. Beck et al.[13] showed that the tensile and yield strengths of CASS increase with δ ferrite content up to 40% at both room and elevated temperatures. The strengthening effect of ferrite phase is attributed to ferrite-austenite boundaries and can be explained with the Hall-Petch model.[14] Ferrite phase is also crucial for the soundness and weldability of steel castings. A minimum ferrite content is often specified for SS welds to reduce the tendency of hot cracking. In addition, the presence of ferrite phase can improve the resistance to

sensitization and stress corrosion cracking (SCC).[15] In susceptible environments, CASS tends to be more resistant to SCC than the same grade of wrought SS. This beneficial effect of ferrite was clearly demonstrated by Hughes et al.[16] in boiling water reactor (BWR) environments. Using slow strain rate tests, they showed that CF-3, CF-3A, and CF-8 have an exceptional resistance to intergranular SCC (IGSCC) in high-purity (HP) water containing 6-8 ppm dissolved oxygen (DO).

While the presence of δ ferrite in CASS is mostly beneficial, ferrite phase can also exert a detrimental effect on the fracture resistance of CASS under certain conditions. Exposed to temperatures of 300-500°C, ferrite phase is vulnerable to a low-temperature thermal aging phenomenon known as "475°C embrittlement."[17,18] The consequences of the thermal aging embrittlement are an increased tensile strength and reduced ductility.[19,20] The upper-shelf impact energy is also reduced, and the ductile-to-brittle transition temperature shifts higher.[20]

Because of thermal aging embrittlement, the long-term performance of CASS materials at elevated service temperatures is of concern. The degradation of CASS components resulting from thermal aging embrittlement has been recognized as a potential issue for aging reactors.[21] Several research programs have been conducted to assess Charpy impact properties and JR resistance curves of thermally aged CASS.[22,23] It was found that thermal aging at 290-450°C up to 30,000 hr leads to a significant deterioration in the fracture properties of CASS. The lower bound of impact energy and fracture toughness (J_{IC}) can be as low as 20 J/cm^2 and 25 kJ/m^2, respectively, at room temperature. The ductile-to-brittle transition temperature of CASS is also shifted to around 0°C for the thermally aged CASS. The extent of the thermal aging embrittlement increases with ferrite content and is sensitive to ferrite morphology.[22]

The mechanism of thermal aging of duplex SSs has been studied extensively.[17-20, 22-28] It is widely accepted that embrittlement is caused by the instability of the ferrite phase under thermal aging. The main reasons of the hardening and loss of toughness are (1) the formation of Cr-rich α' phase through spinodal decomposition, and (2) the precipitation and growth of carbides and G-phase at ferrite-austenite phase boundaries. Obviously, these microstructural changes are thermally activated and are fundamentally controlled by solid-state diffusion. Therefore, the thermal aging time for a given extent of degradation (e.g., an increase in hardness or decrease in toughness) follows an Arrhenius-type relationship.[24]

Besides thermal aging, neutron irradiation can also affect the microstructural evolution of CASS profoundly. Under fast neutron bombardment, lattice atoms in a crystalline material are displaced from their original sites by cascade damage. An avalanche of lattice displacements gives rise to point defect supersaturation, which does not exist under thermal equilibrium.[29],[30] These point defects evolve at irradiation temperatures to form irradiation defects, giving rise to irradiation hardening and embrittlement. The irradiation embrittlement can generate further degradation in the ferrite phase, leading to an additional loss of fracture toughness. Furthermore, the presence of nonequilibrium point defects in irradiated microstructures can enhance the transportation of solutes in materials by radiation-enhanced diffusion.[30] The elevated diffusivity under neutron irradiation could certainly affect the kinetics of thermal aging.

Thus, a combined effect of irradiation embrittlement and thermal aging could not only produce a higher degree of embrittlement, but also affect the rate of degradation development.

While the thermal aging embrittlement of CASS has been studied extensively, very limited data exist in the open literature for neutron-irradiated CASS.[55,31~~31~~,32~~32~~] Two tests conducted on thermally aged and irradiated CF-8M showed a higher degree of embrittlement in the CASS material than wrought SSs.[31~~31~~] It is not clear, however, if the simultaneous exposure to irradiation and thermal aging would reduce the fracture resistance to a lower level than either of the degradation mechanisms can impart alone. If so, the combined effect is not only important for internal components made of CASS, but also for SS weld metals that possess a similar austenite-ferrite duplex microstructure. While weld metals may contain less ferrite phase than that in CASS materials, a minimum ferrite content is usually specified for weld metals to engineer against hot cracking. Thus, weld metals may be subjected to the same type of degradation as CASS. A better understanding of the combined effect of thermal aging and irradiation would also be helpful to address issues concerning SS weld metals.

Formatte
and gram
Formatte
and gram
Formatte
and gram
Formatte
and gram

In the current study, several CF grades of CASS were irradiated to approximately 0.08 displacements per atom (dpa). Both as-received and thermally aged specimens are included. Fracture toughness J-integral resistance (J-R) curve tests were conducted on the irradiated and unirradiated control samples to assess the extent of embrittlement resulting from neutron irradiation and thermal aging. Additionally, crack growth rate (CGR) tests were carried out prior to the fracture toughness tests in low electrochemical potential (ECP) environments to evaluate their SCC performance. At 0.08 dpa, irradiation embrittlement of ferrite phase is anticipated to some extent, but little effect either on embrittlement or stress corrosion susceptibility would be expected for austenite phase. Thus, the current work is focused on the effects of thermal aging and irradiation on the ferrite phase. At higher irradiation levels, additional effect would occur due to embrittlement and increased SCC susceptibility of austenite phase. Since elevated susceptibility to irradiation-assisted stress corrosion cracking (IASCC) is unlikely at this low dose, the SCC CGR test durations were kept relatively short in the present study. Still, the CGR tests could provide corrosion fatigue starter cracks for the subsequent fracture toughness J-R curve tests, so that any environmental contribution to the fracture behavior of CASS could be detected.

2 Experimental

2.1 Materials and Specimens

Three experimental heats of corrosion-resistant CASS (CF-3, CF-8, and CF-8M) were obtained from a previous ANL research program.[44] The CASS heats are static cast slabs with dimensions of 610 x 610 x 76 mm. A ferrite scope measurement on these heats showed that the CF-3 and CF-8 heats contained approximately 24% and 23% delta ferrite, respectively, and the CF-8M heat had 28% delta ferrite. Table 1 gives the compositions of these materials. Both as-received (or unaged) and thermally aged specimens were prepared from these heats. The thermal aging conditions are given in Table 2. Figure 1 shows metallurgical images of the CASS materials used in this study. The samples were polished with SiC papers up to 1200 grit. After a final finish with 1 μm diamond slurry, the polished surfaces were etched with ferric chloride. Both the unaged and thermally aged microstructures are similar, as shown in Fig. 1. Note that a slight decline in ferrite content was reported for all grades of CASS after thermal aging.[44] For the aging conditions used in the current study (10,000 hr at 400°C), the decrease in ferrite content is insignificant. Thus, the average ferrite contents were considered unchanged after thermal aging.

Table 1. Chemical compositions of the cast stainless steels examined in this study.

Cast Grade	FerriteContent		Heat ID	Composition (wt. %)								
	Measured [a]	Calculated [b]		Mn	Si	P	S	Mo	Cr	Ni	N	C
CF-3	24%	21%	69	0.63	1.13	0.015	0.005	0.34	20.18	8.59	0.028	0.023
CF-8	23%	14%	68	0.64	1.07	0.021	0.014	0.31	20.46	8.08	0.062	0.063
CF-8M	28%	25%	75	0.53	0.67	0.022	0.012	2.58	20.86	9.12	0.052	0.065

a. Measured with a ferrite scope,Ref. [44].
b. Calculated with Hull's equations, Ref. [4]

Table 2. Thermal aging conditions for the cast stainless steels in this study.

Cast Grade	Ferrite [a]	Spec. Code	Heat ID	Thermal Aging Condition
CF-3	24%	A	69	Unaged
		B	69	10,000 hr at 400°C
CF-8	23%	E	68	Unaged
		F	68	10,000 hr at 400°C
CF-8M	28%	I	75	Unaged
		J	75	10,000 hr at 400°C

a. Measured with a ferrite scope,Ref. [44].

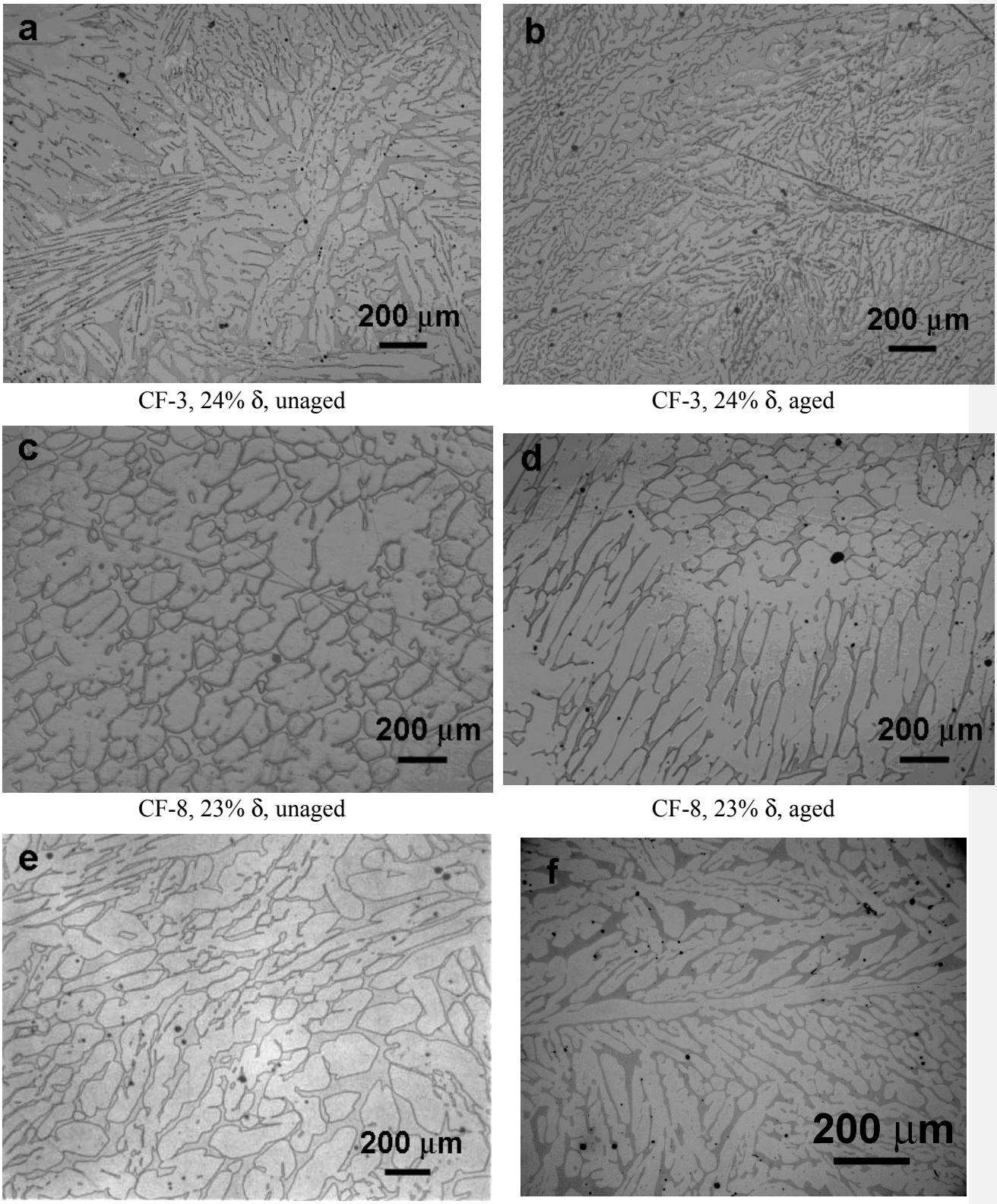

CF-3, 24% δ, unaged

CF-3, 24% δ, aged

CF-8, 23% δ, unaged

CF-8, 23% δ, aged

CF-8M, 28% δ, unaged (from ref. [44])

CF-8M, 28% δ, aged

Figure 1. Metallurgical images of the unaged and thermally aged CASS materials.

Constrained by irradiation space, sub-sized compact tension (CT) specimens were used in this study. The sample was about 6.5-mm thick (i.e., 1/4T-CT) and 14-mm high. The starter notch size was about 6 mm. To ensure an in-plane crack growth, side grooves approximately 5% of the thickness were machined on both sides of the sample. Figure 2 is a schematic of the sample used in this study. The red lines in the figure are electrical leads spot-welded on the specimen.

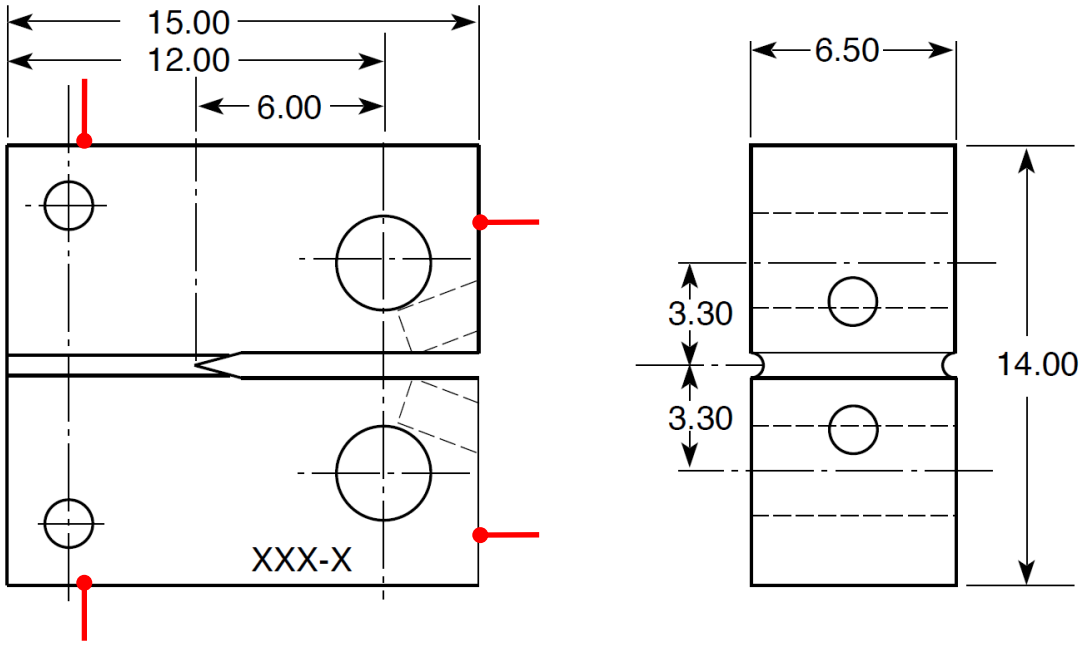

Figure 2. Schematic of 1/4T-CT specimen used in this study (red lines represent electrical leads).

Field Co

2.2 Irradiation

The CASS specimens were irradiated in a helium-filled capsule in the Halden reactor, a boiling heavy water reactor in Norway. Figure 3 shows the assembly of the irradiation capsule. Some disk-shaped samples for transmission electron microscopy analyses were also included in a cylindrical container in the irradiation capsule (item 7 in Fig. 3). The irradiation temperature was ~315°C, and two sets of melting alloy temperature monitors (item 5) were installed in the irradiation assembly.

During the irradiation experiment, three fluence monitor wires (Fe, Ni, and Al/Co alloy) were placed outside the irradiation capsule. After the irradiation, dosimetry was performed by the Halden researchers on these wires. Using the activation cross sections determined previously, they estimated the accumulated neutron fluence for the irradiation capsule. The obtained fast neutron fluence (E > 1MeV) was about 5.56 x 10^{19} n/cm^2, which corresponds to a displacement damage of 0.08 dpa for the samples.

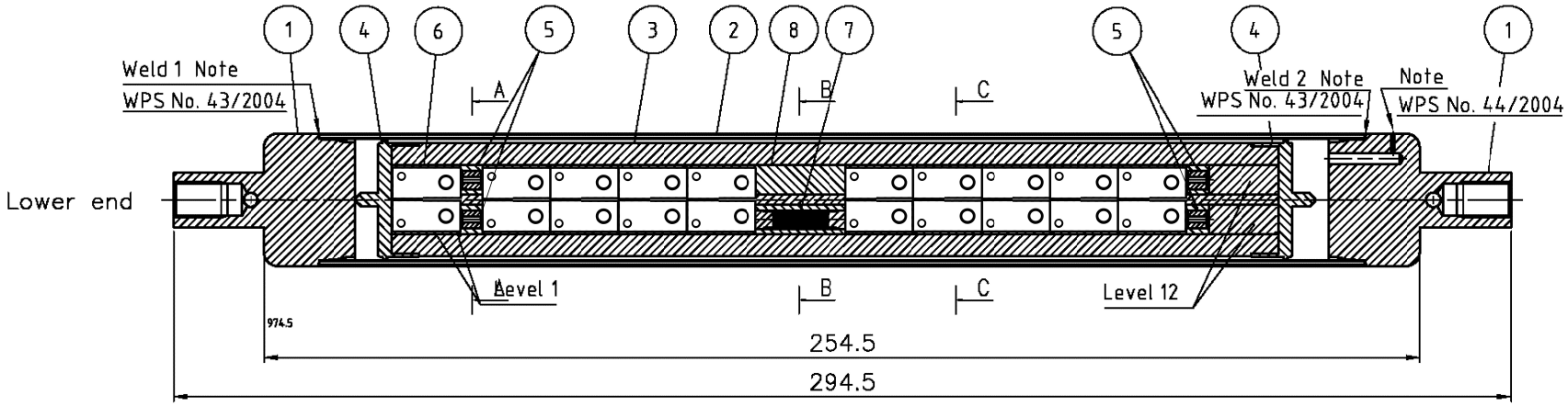

1. End Plug
2. Outer Capsule
3. Heat Transfer Body
4. End Guide Sleeve
5. Melting Alloy Assembly
6. CT Specimens
7. TEM Specimens Container
8. Spacer

Figure 3. Irradiation capsule of low-dose Halden irradiation.[3333]

Formatte
pt, Check
by 3 pt

Field Co

2.3 Test Facility

Two servo-hydraulic mechanical test systems located in the Irradiated Materials Laboratory (IML) at Argonne National Laboratory were used in this study. The IML is a radiological facility equipped with four air-atmosphere beta-gamma hot cells. The hot cells are maintained at a negative pressure with respect to the surroundings to maintain a proper radiological barrier. The two test systems are installed in separate hot cells. Each of the hot cells is equipped with its own loading frame, autoclave, load cell, linear voltage displacement transducer (LVDT), Instron control console, and data acquisition system.

In the current study, the tests were performed either in a simulated pressurized water reactor (PWR) environment or in a low-DO high-purity water environment. Both environments have low corrosion potentials, which are known to reduce the sensitivity of SSs to IASCC.[3434] The simulated PWR water contained ~2 ppm lithium, ~1000 ppm boron, and ~2 ppm hydrogen. The conductivity was about 20 μS/cm. The low-DO high-purity water contained less than 10 ppb dissolved oxygen, and the conductivity was kept below 0.07 μS/cm during the tests. The test environments were provided by two water recirculation loops, and a schematic diagram of loop #1 is shown in Fig. 4. Each loop consists of a storage tank, a high pressure pump, a regenerative heat exchanger, an autoclave, an ECP cell, a back-pressure regulator, two ion-exchange cartridges, and several heaters. The high-pressure section of the loop extends from the high-pressure pump (item 13 in Fig. 4) through the back-pressure regulator (item 10 in Fig. 4). The rest of the loop is kept at low pressure. Over-pressurization of the high-pressure portion of the system is prevented by two rupture disks (items 3 and 15 in Fig. 4) located at the downstream of the high-pressure pump. The autoclaves are one-liter Type 316 stainless steel autoclaves and rated to 2900 psig for 350°C. The loop for hot cell #1 is a PWR water system, and hydrogen is used as cover gas. A hydrogen leak detection/alarm unit (items 36 - 38 in Fig. 4) is installed. For the hot cell #2 loop, a low-corrosion-potential environment is simulated in high-purity water using a mixture of nitrogen with 4% hydrogen as cover gas. For both systems, water is circulated at a rate of 20-30 mL/min through the autoclaves. The water conductivity and pH can be monitored with inline sensors. During the tests, the temperature and pressure of the autoclaves were kept at ~320°C and ~1800 psig, respectively.

Formatte
and gram

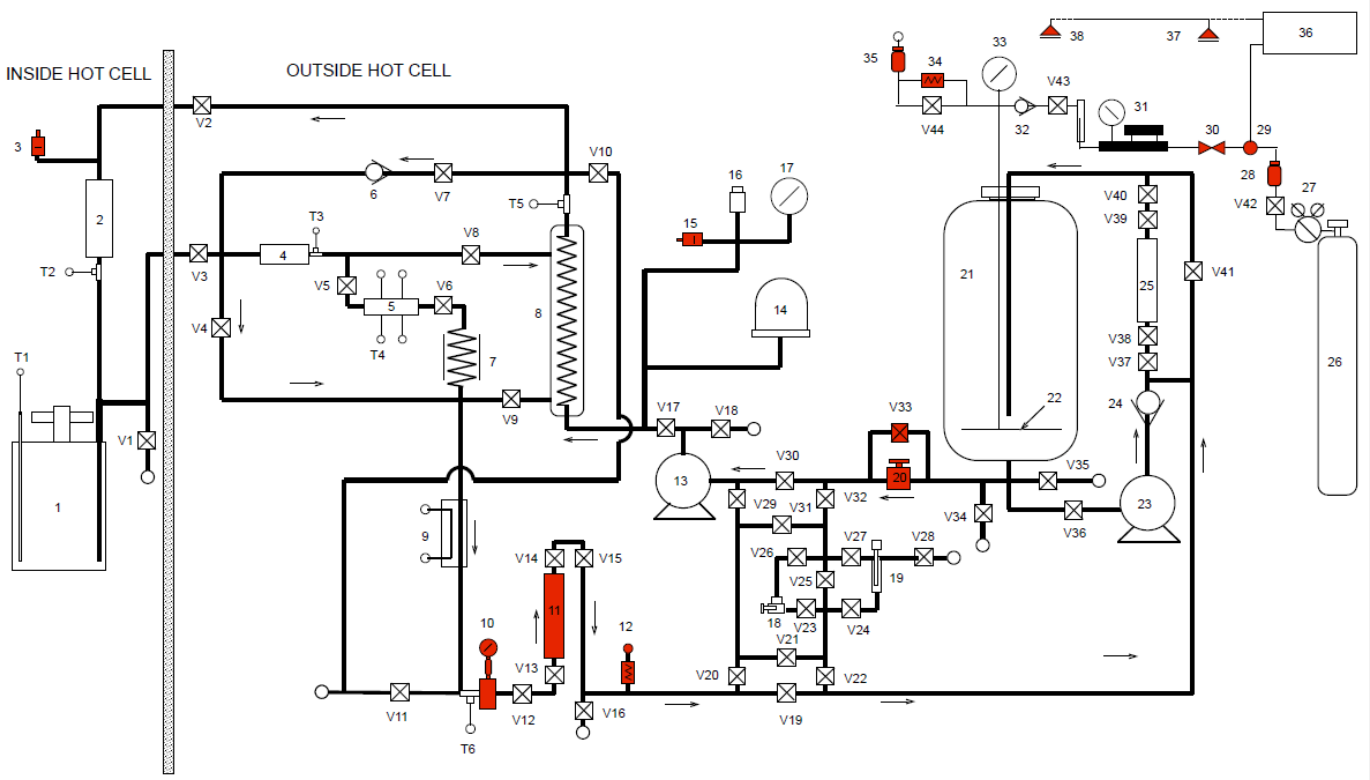

1. Autoclave
2. Autoclave preheater
3. Rupture disk
4. ECP preheater
5. ECP cell
6. Check valve
7. Air Cooled Coil
8. Heat exchanger
9. Chilled block
10. Back-pressure regulator
11. Ion exchange cartridge
12. Pressure relief valve
13. High-pressure pump
14. Accumulator
15. Rupture disk
16. Pressure transducer
17. High pressure gauge
18. Conductivity sensor
19. pH sensor
20. Solenoid valve
21. Feedwater storage tank
22. Sparge tube
23. Tank recirculation pump
24. Check valve
25. Ion exchange cartridge
26. Cover gas supply cylinder
27. High-pressure regulator
28. Flash arrestor
29. Solenoid valve
30. Excess flow valve
31. Low-pressure regulator
32. Check valve
33. Vacuum & pressure gauge
34. Pressure relief valve
35. Flash arrestor
36. Hydrogen alarm control panel
37. Hydrogen leak sensors
38. Hydrogen leak sensors
V = Valve
T = Thermocouples

Figure 4. Recirculation water loop for Cell 1 of the IML (items in red are safety significant components)

2.4 Crack Growth Rate and Fracture Toughness J-R curve Tests

2.4.1 Crack Growth Rate Test

All CGR tests in this study were performed on the 1/4T-CT samples described above. Crack extensions were monitored with the direct current potential drop (DCPD) method during the tests. With this method, four electrical leads were spot welded on the CT sample (red lines shown in Fig. 2). A constant current was passed through the sample, and the potential drop across the crack mouth was measured and related to the crack extension of the CT sample with a calibrated correlation curve.

The CGR tests were carried out in either a simulated PWR water environment or a low-DO high-purity water environment.

A typical CGR test is started with cyclic loading to pre-crack the sample in the test environment. A load ratio around 0.2-0.3, frequency of 1-2 Hz, and maximum stress intensity factor (K_{max}) between 10 and 16 MPa $m^{1/2}$ are used for pre-cracking. The objective of this step is to generate a sharp fatigue crack and to advance the crack tip passing beyond the area close to the machine notch. The properties at this area may have been altered by machining and do not represent the material's intrinsic behavior.

The stress intensity factor *K* for a CT specimen is calculated by:

$$K = \frac{P}{(B \cdot B_N \cdot W)^{1/2}} \cdot \frac{(2 + a/W)}{(1 - a/W)^{3/2}} \cdot f(\frac{a}{W}) \quad (1)$$

Field Co

where *P* is applied load; *B* is the specimen thickness; B_N is the net specimen thickness (or distance between the roots of the side grooves); *a* is crack length; and *W* is specimen width (measured from the load line to the back edge of the specimen). The geometry factor [f(a/W)] for a CT specimen is:

$$f(\frac{a}{W}) = 0.886 + 4.64\left(\frac{a}{W}\right) - 13.32\left(\frac{a}{W}\right)^2 + 14.72\left(\frac{a}{W}\right)^3 - 5.60\left(\frac{a}{W}\right)^4 \quad (2)$$

Field Co

Once a fatigue crack is initiated, a series of test steps is carried out with gradually increased rise times and load ratios. The measured CGRs in these test steps include the contributions from both mechanical fatigue and corrosion fatigue. With the change in loading conditions, the contribution of mechanical fatigue is gradually reduced while the environmental effect is enhanced. Figure 5 illustrates the principle of introducing environmentally assisted cracking in a test. The changes in test conditions should produce cyclic CGRs along the green line. The cyclic CGR test is transitioned to a SCC CGR test when a significant environmental enhancement is observed.

Because of the beneficial effects of ferrite and the reduced sensitivity to IASCC in low-corrosion-potential environments, relatively low CGRs are expected for the CASS specimens even after irradiation to 0.08 dpa. To measure SCC CGRs at such low growth rates, a considerable amount of time is needed to collect data for adequate measurements. Since the focus of this study was on embrittlement (i.e., loss of facture toughness), a limited amount of time was spent on collecting SCC CGR data.

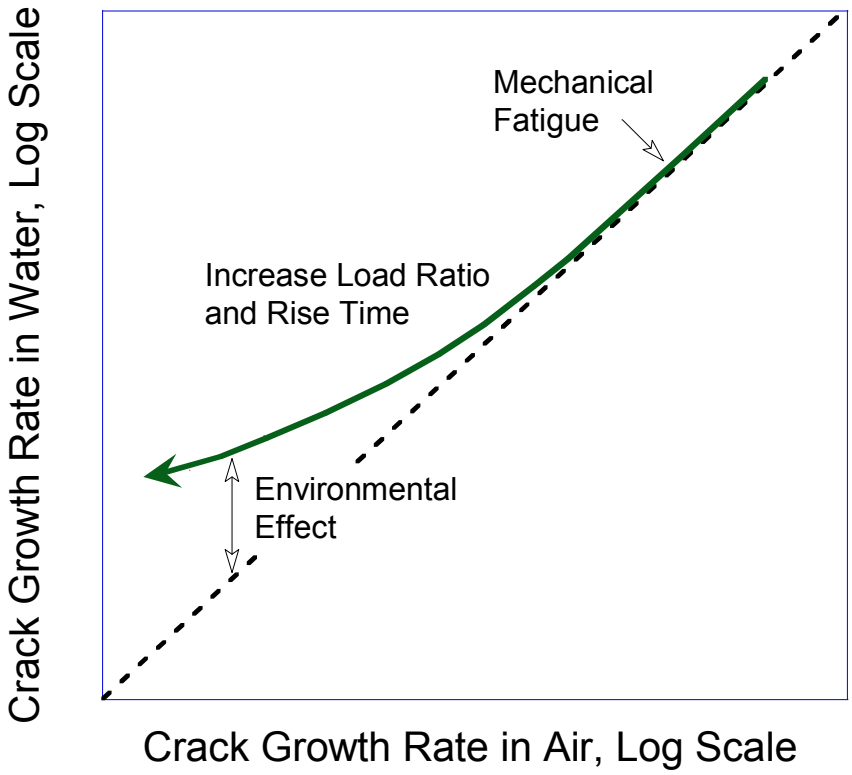

Figure 5. Schematic for inducing environmentally assisted cracking in test environment.

2.4.2 Fracture Toughness J-R curve Test

After each SCC CGR test, a fracture toughness J-R curve test was conducted on the same sample in the test environment. This test was performed with a constant stain rate of 0.43 μm/s, and the load and sample extension were recorded continuously outside the autoclave. The load-line displacement at load points was determined by subtracting the extension of the load train, which had been measured prior to the test. During the test, the loading was interrupted periodically, and the specimen was held at a constant extension to measure crack length with the DCPD method. Before each DCPD measurement, the sample stress was allowed to relax at a constant displacement for 30 s.

The J-integral was calculated from the load (P) vs. load-line displacement (v) curve according to ASTM Specification E 1820-8a.[35] The J is the sum of the elastic and plastic components,

$$J = J_{el} + J_{pl} \tag{3}$$

At a hold point i corresponding to a crack length a_i, as well as v_i and P_i on the load vs. load-line displacement curve, the elastic component $J_{el(i)}$ is given by:

$$J_{el(i)} = \frac{(K_{(i)})^2(1-\nu)^2}{E} \tag{4}$$

where ν is Poisson's ratio, and the stress intensity $K_{(i)}$ is calculated from Eqs. 11 and 22. The plastic component $J_{pl(i)}$ is given by:

$$J_{pl(i)} = \left[J_{pl(i-1)} + \left(\frac{\eta_{(i-1)}}{b_{(i-1)}} \right) \frac{A_{pl(i)} - A_{pl(i-1)}}{B_N} \right] \left[1 - \gamma_{(i-1)} \frac{a_{(i)} - a_{(i-1)}}{b_{(i-1)}} \right] \quad (5)$$

where $b_{(i-1)}$ is the remaining ligament at point *i-1*; $A_{pl(i)}$ is the area under the load vs. load-line displacement curve; and B_N is the net specimen thickness. In addition, $\gamma_{(i)}$ and $\eta_{(i)}$ are factors that account for the crack growth effects on J during the test and are expressed as:

$$\eta_{(i-1)} = 2.0 + 0.522 \frac{b_{(i-1)}}{W} \quad (6)$$

$$\gamma_{(i-1)} = 1.0 + 0.76 \frac{b_{(i-1)}}{W} \quad (7)$$

The quantity $A_{pl(i)}$ - $A_{pl(i-1)}$ is the increment of the plastic area under the load vs. load-line displacement curve between lines of constant plastic displacement at points *i - 1* and *i*. The plastic area under the load vs. load-line displacement curve is given by

$$A_{pl(i)} = A_{pl(i-1)} + \frac{[P_i + P_{i-1}]\left[v_{pl(i)} - v_{pl(i-1)} \right]}{2} \quad (8)$$

where the plastic components of the load-line displacement, $v_{pl(i)}$, are:

$$v_{pl(i)} = v_{(i)} - P_i C_{LL(i)} \quad (9)$$

In the above, $v_{(i)}$ is the total load-line displacement, and $C_{LL(i)}$ is the compliance required to give the current crack length a_i and can be determined as follows:

$$C_{LL(i)} = \frac{\left[1.62 + 17.80(a_i/W) - 4.88(a_i/W)^2 + 1.27(a_i/W)^3 \right]}{E' B_e [1 - (a_i/W)^2]} \quad (10)$$

where B_e is the specimen effective thickness given by $B - (B - B_N)^2/B$, and $E' = E/(1 - \upsilon^2)$.

A J-R curve is constructed by fitting the calculated J values and corresponding crack lengths to a power law relationship. The J value at the intersection of the power law curve and the 0.2-mm offset blunting line are reported. Note that a blunting line of four times flow stress ($4\sigma_f$) is recommended by Mills [55] for materials with high strain hardening coefficients, and has been used in the previous thermal aging studies on unirradiated CASS.[44] To be consistent with the previous analyses, the same blunting line (i.e., $J/4\sigma_f$) was also used in the current work.

In this study, the estimated flow stresses are approximately 280-340 MPa and 420-520 MPa for unirradiated and irradiated CASS materials, respectively. This relatively low strength allows a maximum J value of 280-360 kJ/m^2 for a typical 1/4T-CT specimen. The maximum crack extension is limited below ~1.3 mm in most cases. Because of the low strength and high fracture toughness of CASS materials, the required crack tip constraint and upper limit of J integral are often invalid with the 1/4T-CT specimen. This is especially true for the unirradiated CASS samples since the strength is even lower without irradiation hardening. For this reason, the J values determined from this study normally cannot be validated for J_{IC} per ASTM E182-8a.

2.4.3 Fractographic Examination

After each CGR/JR test, the final crack size was marked by fatigue cycling in an air atmosphere at room temperature. The specimen was then fractured, and the fracture surface was examined by scanning electron microscopy (SEM). Since the irradiated sample was highly radioactive, a two-step replication technique was developed for the fractographic examination. After cleaning the tested sample remotely using manipulators, we used a two-part synthetic compound to produce a negative replica of the fracture surface inside the hot cell. The negative replica was then removed from the hot cell and transferred to a radiological fume hood for decontamination. The second step of casting was to apply a low-viscosity epoxy on the surface of the negative replica. The cast was kept at approximately 70°C for several days to harden the epoxy replica. The negative replica was then removed. The obtained epoxy replica was coated with a layer of gold before it was transferred for SEM examination.

The CGR test and JR test regions were identified on the SEM images, and their fracture morphologies were analyzed. The physical crack length was also measured on the images, and a 9/8 averaging technique was used to account for the uneven extensions at the crack front. With this technique, nine measurements were taken along the crack front spaced across the width of the sample at equal intervals. The two near-surface measurements were averaged, and the resultant value was averaged with the remaining seven measurements to obtain the average crack length. All crack extensions determined from the DCPD method were scaled proportionately to match the final SEM-measured crack length.

3 Results

Seven irradiated and four unirradiated control specimens from three heats of CASS were tested in the current study. The test matrix is shown in Table 3. The specimens were unaged and thermally aged pairs. The irradiated samples received a displacement dose of ~0.08 dpa. The CF-3 specimens were tested in either low-DO high-purity water or PWR water, and all CF-8 and CF-8M specimens were tested in low-DO high-purity water.

Table 3. Test matrix of unirradiated and irradiated low-dose CASS specimens.

Sample ID	Dose (dpa)	Heat ID	Materials	Test Environment	Facility	CGR	JR	SEM
A-N1	-	69	CF-3, 24% δ, unaged	Low-DO high-purity	Cell 2	√	√	√
A-1	0.08	69	CF-3, 24% δ, unaged	PWR	Cell 1	√	-	√
A-2	0.08	69	CF-3, 24% δ, unaged	Low-DO high-purity	Cell 2	√	√	√
B-N1	-	69	CF-3, 24% δ, aged	PWR	Cell 1	√	√	√
B-1	0.08	69	CF-3, 24% δ, aged	PWR	Cell 1	√	√	√
E-N1	-	68	CF-8, 23% δ, unaged	Low-DO high-purity	Cell 2	√	√	√
E-1	0.08	68	CF-8, 23% δ, unaged	Low-DO high-purity	Cell 2	√	√	√
F-N1	-	68	CF-8, 23% δ, aged	Low-DO high-purity	Cell 2	√	√	√
F-1	0.08	68	CF-8, 23% δ, aged	Low-DO high-purity	Cell 2	√	√	√
I-1	0.08	75	CF-8M, 28% δ, unaged	Low-DO high-purity	Cell 2	√	√	√
J-1	0.08	75	CF-8M, 28% δ, aged	Low-DO high-purity	Cell 2	√	√	√

3.1 CF-3 Cast Stainless Steel

3.1.1 Unaged CF-3 CASS

3.1.1.1 Unirradiated specimen A-N1 tested in low-DO high-purity water

Crack growth rate test

Specimen A-N1 was an unirradiated control sample tested in low-DO high-purity water. The material was an unaged CF-3 CASS with ~24% ferrite (Heat 69). The objective of this test was to provide a baseline for the irradiated tests. The test conditions and results are summarized in Table 4, and a crack-length history plot is shown in Fig. 6.

Fatigue pre-crack was initiated at ~15.4 MPa $m^{1/2}$ with a triangular waveform of 1 Hz and a load ratio of ~0.16. A cyclic CGR slightly below the fatigue growth rate in air was readily obtained in this sample. After ~220-μm crack extension, the load ratio and rise time were increased slowly to induce environmentally assisted cracking. The environmental effect on CGR was difficult to establish, and the crack stalled several times in the following test periods. Nonetheless, elevated crack growth rates were observed for this CASS sample under cyclic

loading in the low-DO high-purity water. The cyclic CGR data obtained from this test are plotted against the fatigue CGRs in air in Fig. 7. The fatigue CGRs are estimated based on James and Jones[37] with the load ratios and rise times given in Table 4. A corrosion fatigue curve proposed by Shack and Kassner[38] for unirradiated SSs in 0.2-ppm DO water at 290°C is also included in the figure as a reference. Note that the data point above the reference line (from test period *z*) was due to a temperature increase in the autoclave during that test period. After the temperature was stabilized, a much lower CGR was measured in the next test period. It is clear that the corrosion fatigue response of this CASS sample is better than that of typical SSs in low-DO high-purity water.

After a total of ~900-µm crack extension, the test was set to a constant load with periodical partial unloading (PPU) every 2 hr. The SCC CGR was negligibly low and was below the detection limit of the DCPD measurement. The SCC behavior of this sample will be discussed at the end of this section along with the other CGR data obtained from the same heat.

Table 4. Crack growth rates of specimen A-N1 (unirradiated and unaged CF-3 with 24% δ ferrite) in low-DO high-purity water.

Test Period	Test Time, h	Test Temp., °C	Load Ratio	Rise Time, s	Return Time, s	Hold Time, s	Kmax, MPa $m^{1/2}$	ΔK, MPa $m^{1/2}$	CGR in Env., m/s	CGR in Air, m/s	Crack Length, mm
Start	0.3										5.978
A	3.2	317	0.16	0.39	0.39	0.11	15.4	12.9	5.94E-08	5.68E-08	6.204
B	5.1	317	0.29	0.36	0.36	0.14	14.5	10.3	1.98E-08	3.36E-08	6.257
C	9.1	317	0.40	0.69	0.69	0.31	14.3	8.6	1.01E-09	1.11E-08	6.265
D	21.8	317	0.21	0.38	0.38	0.12	16.0	12.6	7.14E-08	5.72E-08	6.419
E	24.5	317	0.30	0.74	0.74	0.26	16.5	11.6	3.02E-08	2.49E-08	6.528
F	29.4	317	0.45	0.68	0.68	0.32	16.8	9.3	1.35E-08	1.50E-08	6.611
G	43.2	317	0.60	3.04	3.04	1.96	16.6	6.7	3.02E-10	1.30E-09	6.618
H	50.7	317	0.50	1.65	1.65	0.85	16.9	8.5	5.37E-09	4.87E-09	6.664
I	66.6	317	0.50	6.57	1.31	3.43	16.8	8.4	6.07E-10	1.18E-09	6.685
J	80.2	317	0.49	9.91	3.30	5.09	16.9	8.5	6.25E-10	8.24E-10	6.702
K	97.4	317	0.49	19.9	3.31	10.1	17.0	8.6	3.28E-10	4.25E-10	6.713
L	118.2	317	0.49	39.7	7.94	20.3	17.1	8.7	2.68E-10	2.16E-10	6.728
M	145	317	0.49	99.7	7.98	50.3	17.3	8.8	1.57E-10	9.04E-11	6.737
N	170.5	317	0.49	199.8	7.99	100.2	17.3	8.9	7.96E-11	4.59E-11	6.742
O	196.2	317	0.48	333.6	8.01	166.4	17.3	8.9	1.51E-10	2.80E-11	6.751
P	236.1	318	0.48	667.8	8.01	332.2	17.3	8.9	negligible	1.42E-11	6.750
Q	285.6	318	0.49	133.3	8.00	66.7	17.4	8.9	6.58E-11	7.06E-11	6.758
R	308.1	318	0.49	66.6	7.99	33.4	17.5	8.9	8.93E-11	1.40E-10	6.763
S	316.7	318	0.44	34.2	8.21	15.8	17.4	9.7	3.90E-10	3.46E-10	6.769
t [a]	332.2	318	0.44	68.5	8.22	31.5	17.7	9.8	5.06E-10	1.81E-10	6.795
U	355.8	319	0.49	133.1	7.99	66.9	17.6	9.0	6.71E-11	7.25E-11	6.799
V	363.7	319	0.45	13.6	3.41	6.4	17.6	9.8	1.36E-09	8.90E-10	6.814
W	379.4	319	0.47	33.7	8.09	16.3	17.8	9.5	6.68E-10	3.33E-10	6.837
X	403.6	318	0.48	66.4	7.97	33.6	17.4	9.1	1.62E-10	1.48E-10	6.846
Y	430.8	318	0.49	133.2	8.00	66.8	17.8	9.2	8.67E-11	7.69E-11	6.851
z [b]	452.8	317	0.49	333.8	8.01	166.2	18.1	9.3	3.74E-10	3.19E-11	6.872
aa	500.3	319	0.48	669.5	8.03	330.5	18.1	9.4	3.65E-11	1.64E-11	6.876
1	811.3	318	0.50	12	12	7200	18.0	9.0	negligible	1.37E-12	6.880

[a] The CGR value was obtained from the later part of the test period.

[b] The autoclave temperature was unstable in the test period.

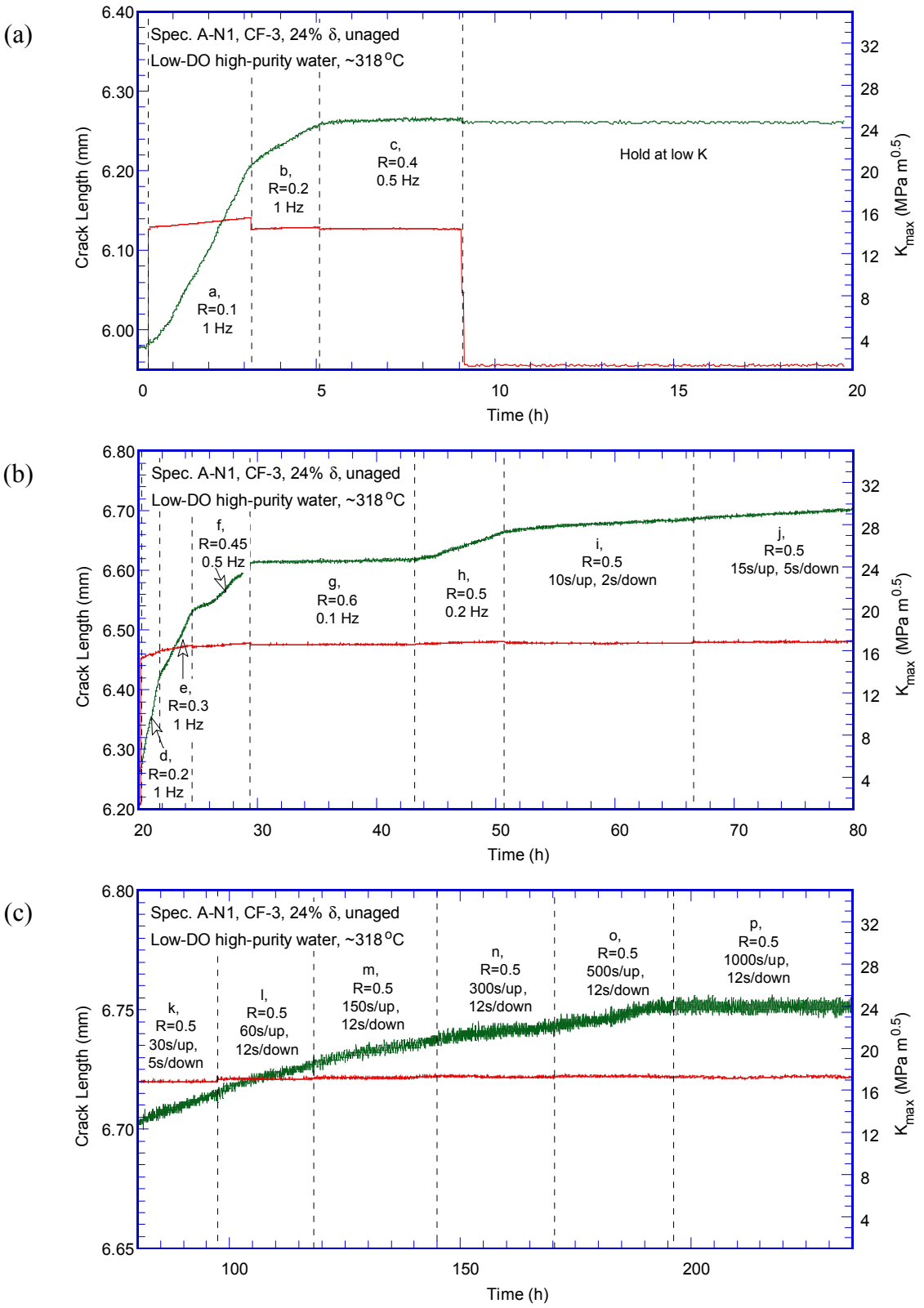

Figure 6. Crack-length-vs.-time plot for specimen A-N1 (unirradiated and unaged CF-3 with 24% ferrite): test periods (a) a-c, (b) d-j, (c) k-p, (d) q-u, (e) v-aa, and (f) 1.

(d)

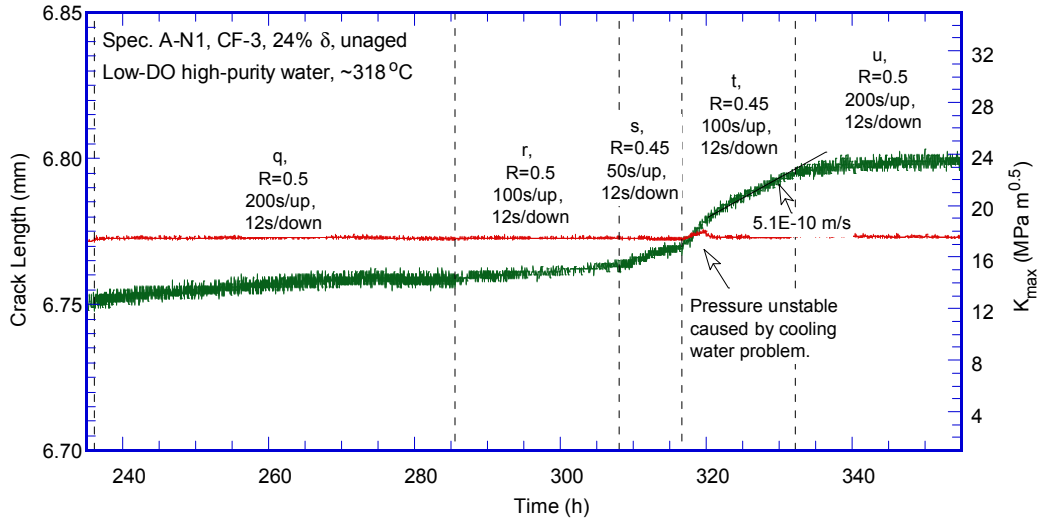

(e)

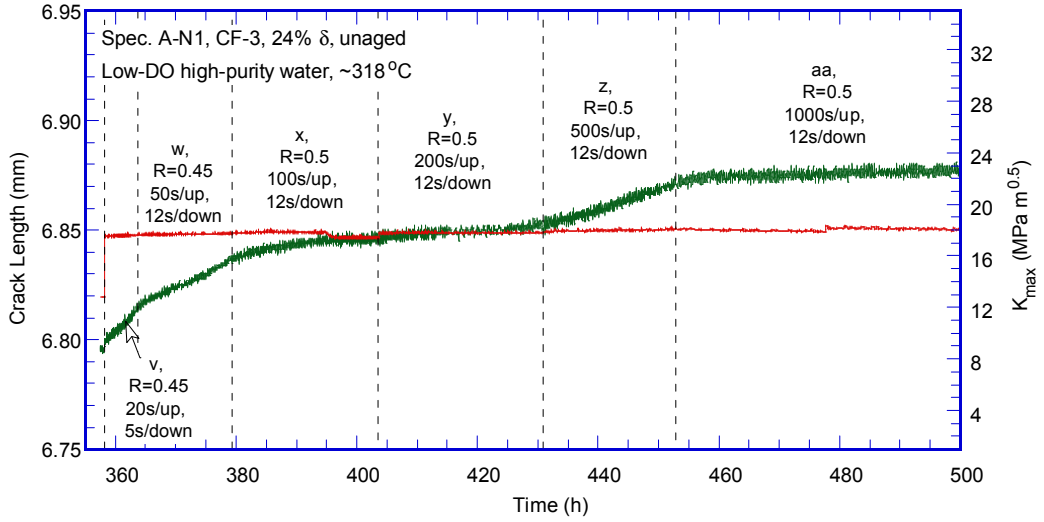

(f)

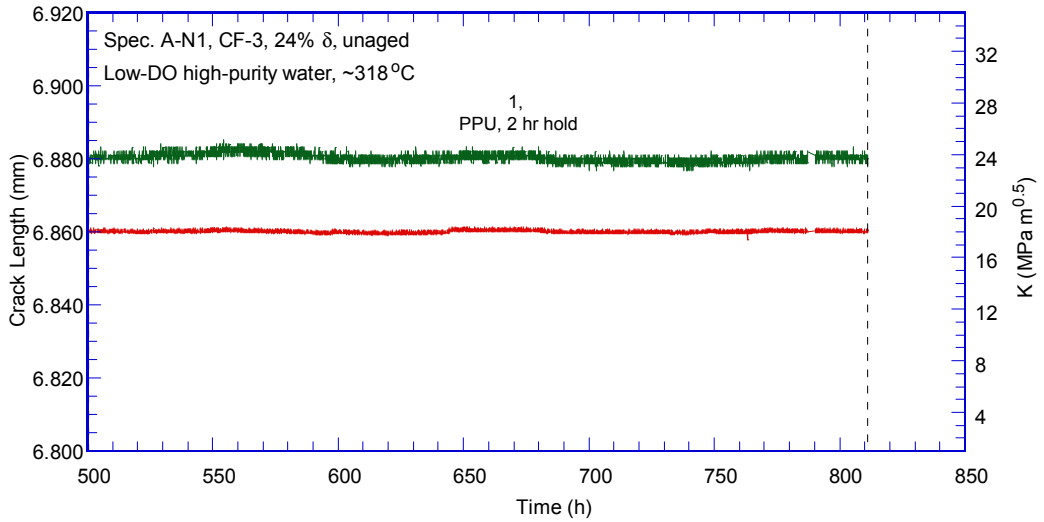

Figure 6. (Contd.)

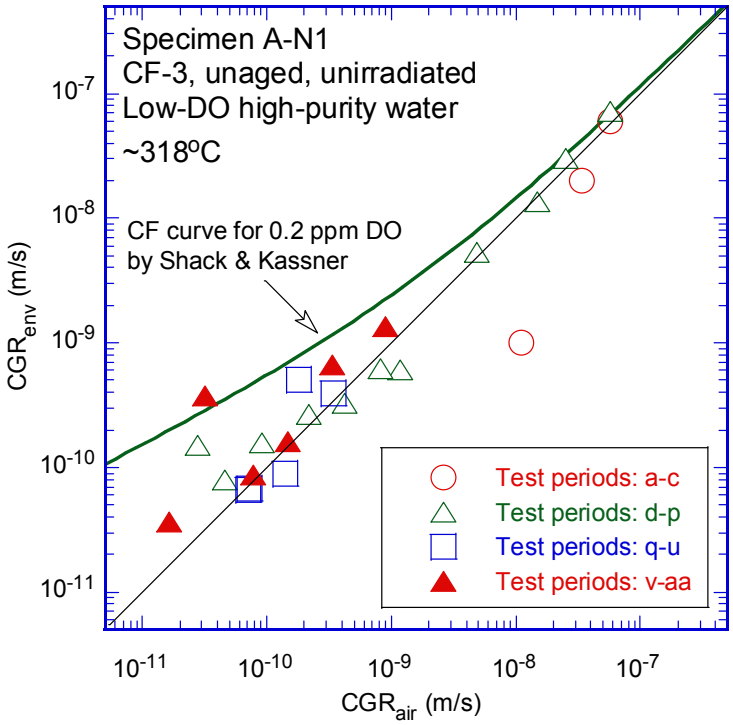

Figure 7. Cyclic CGRs of specimen A-N1.

Field Co

Fracture toughness J-R curve test

A fracture toughness J-R curve test was conducted on the sample in the low-DO high-purity water environment. The sample was loaded at a constant extension rate of 0.43 μm/s while the load and load-line displacement were recorded. During the test, loading was interrupted periodically to measure the crack extension by DCPD. The obtained J and crack extension data are plotted in Fig. 8. Note that the measurement capacity of 1/4T-CT samples is significantly lower than the fracture toughness anticipated for the CASS materials, and thus a validated J-R curve test is not possible for this sample. Nonetheless, the available data points fit to a power-law relationship, and the estimated J value at the 0.2-mm offset line is about 320 kJ/m^2. The straightness of the crack extension and the J_{max} requirement are not met in this analysis due to lack of constraint at the crack tip.

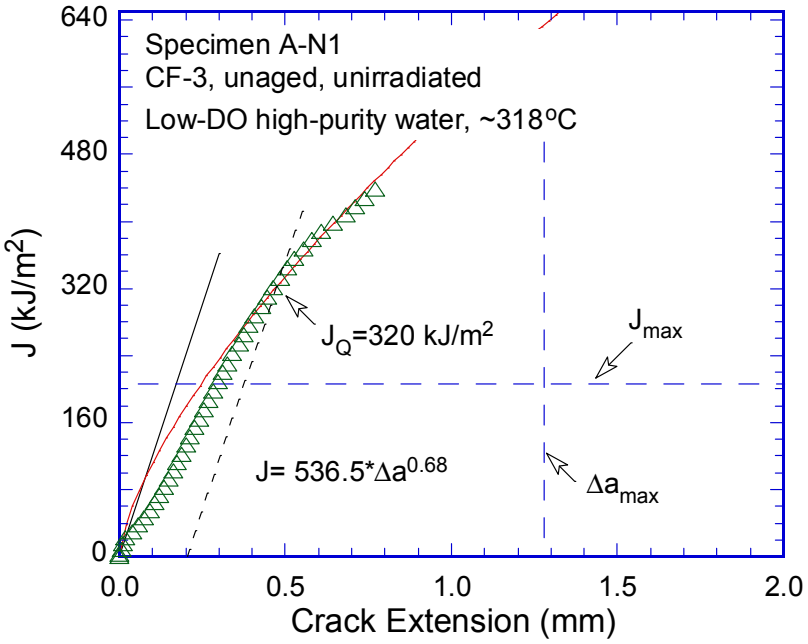

Figure 8. The J-R curve for specimen A-N1.

Field Co

Fractographic examination

After the J-R curve test, the sample was fatigued and broken open at room temperature in an air atmosphere. The fracture surface was examined with SEM (Fig. 9). While the CGR test region shows a transgranular (TG) morphology, the entire JR test region is covered with ductile dimples. A major secondary crack that covers nearly a half of the width of the sample can be seen at the machined notch. This large secondary crack may affect the crack propagation, leading to a curved crack front in the CGR test. Consequently, the final crack size of the JR test is also affected with a significantly higher crack extension on the right-hand side of the SEM image. Figure 10 shows an enlarged view of the fracture surface along the sample central line. More details of the CGR and JR test regions can be seen in Figs. 11 and 12, respectively.

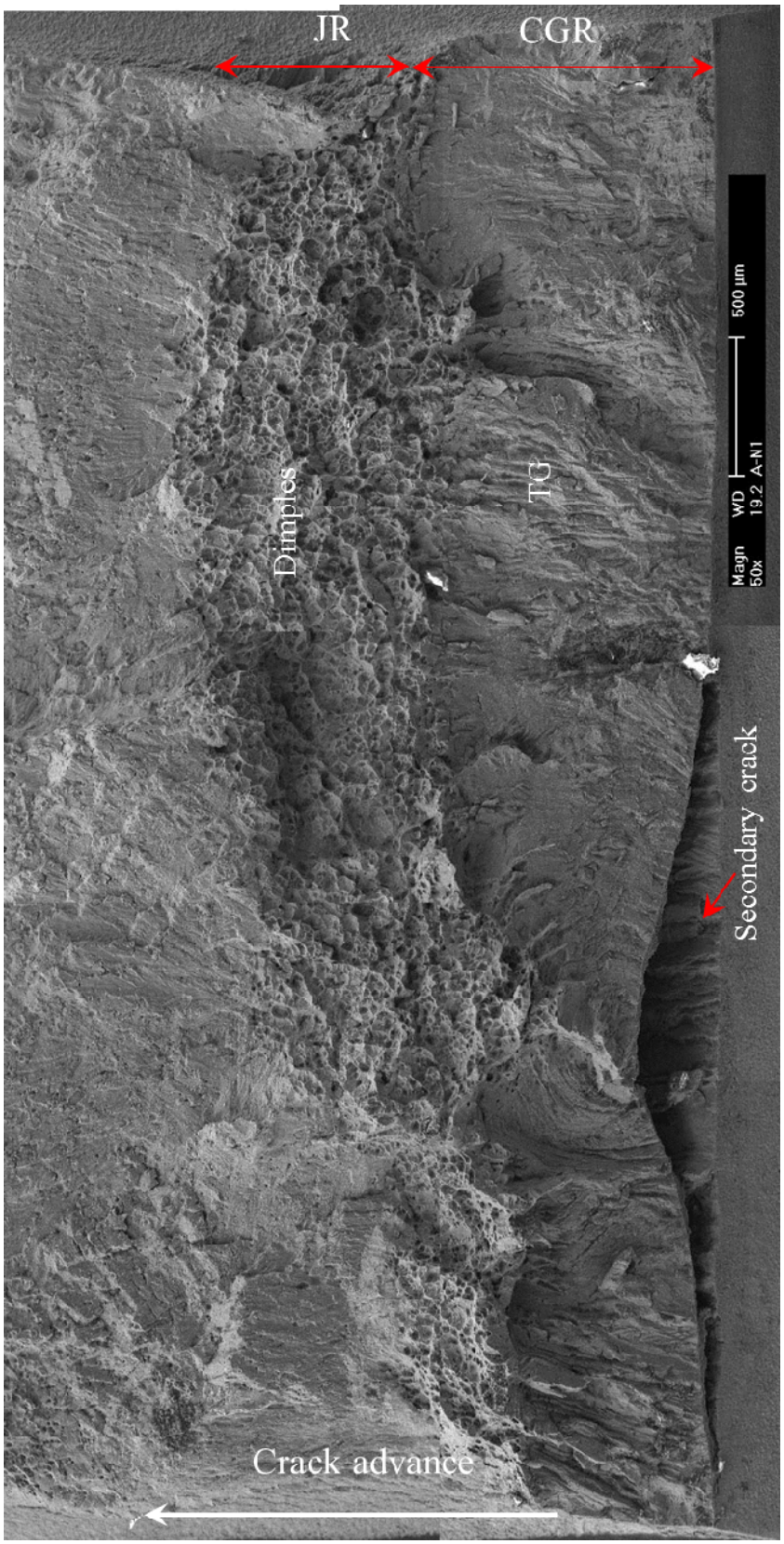

Figure 9. Fracture surface of specimen A-N1 tested in low-DO high-purity water.

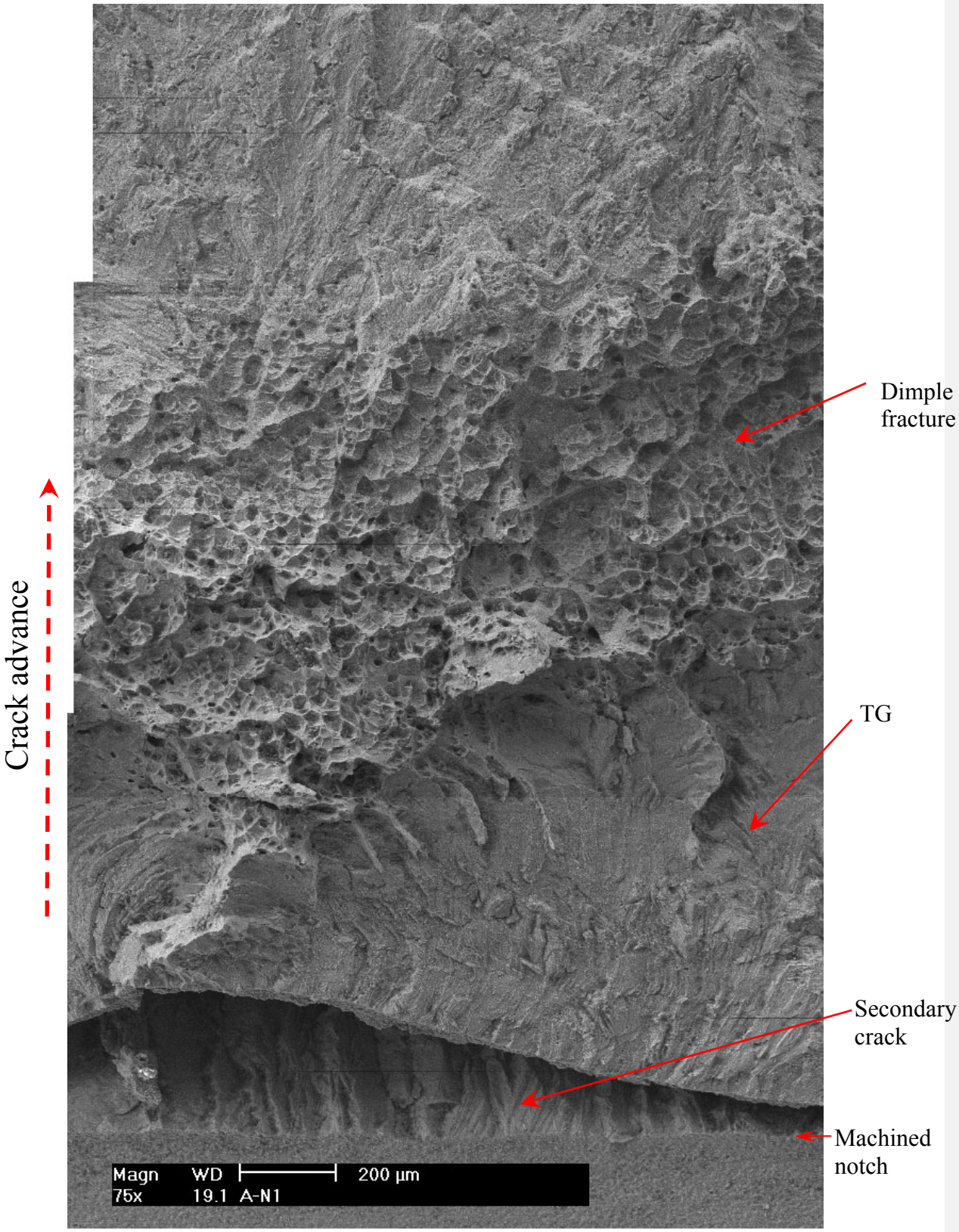

Figure 10. Fracture surface of specimen A-N1 along the sample central line.

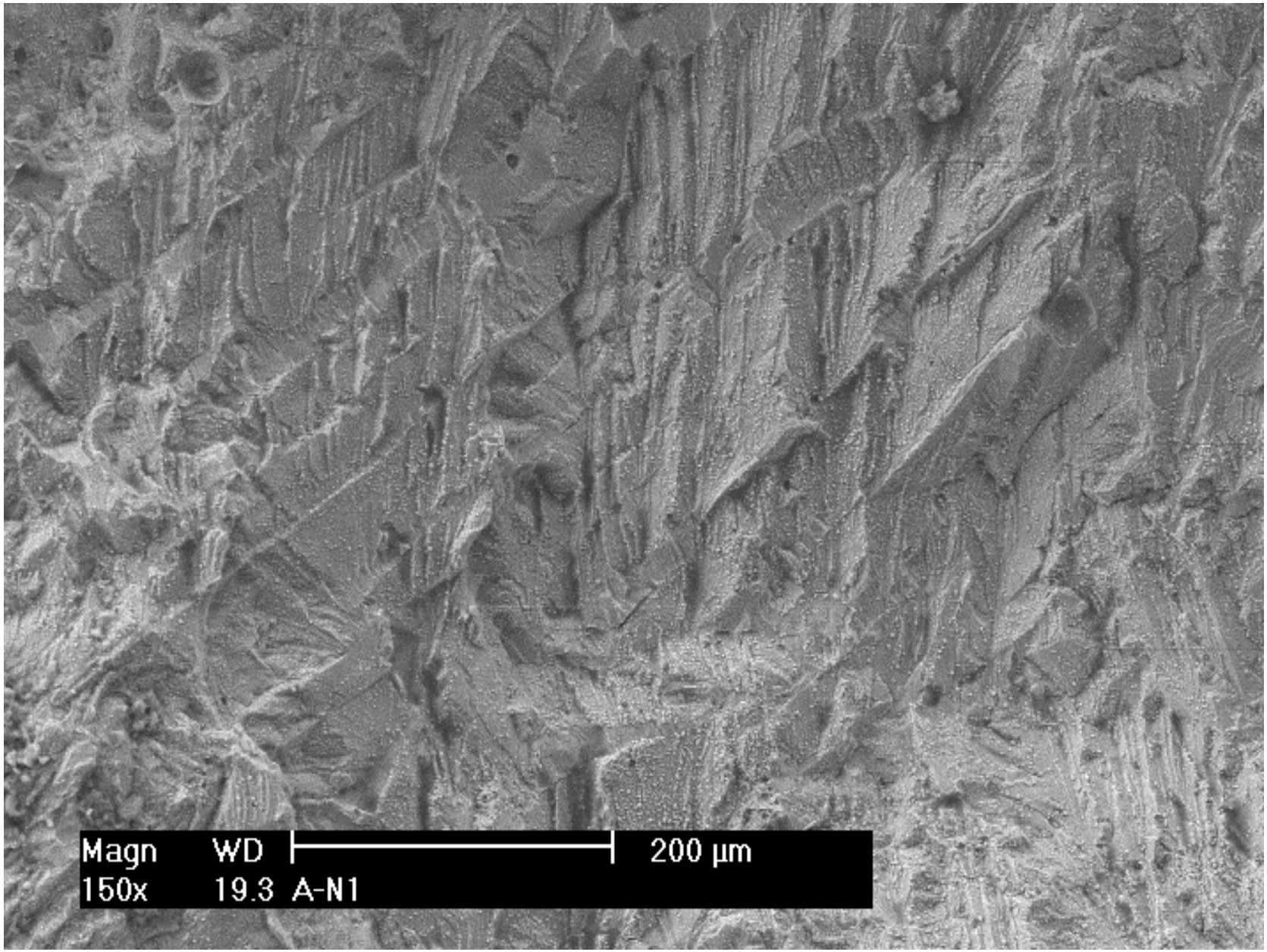

Figure 11. Transgranular fracture in the precracking region of specimen A-N1.

Field Co

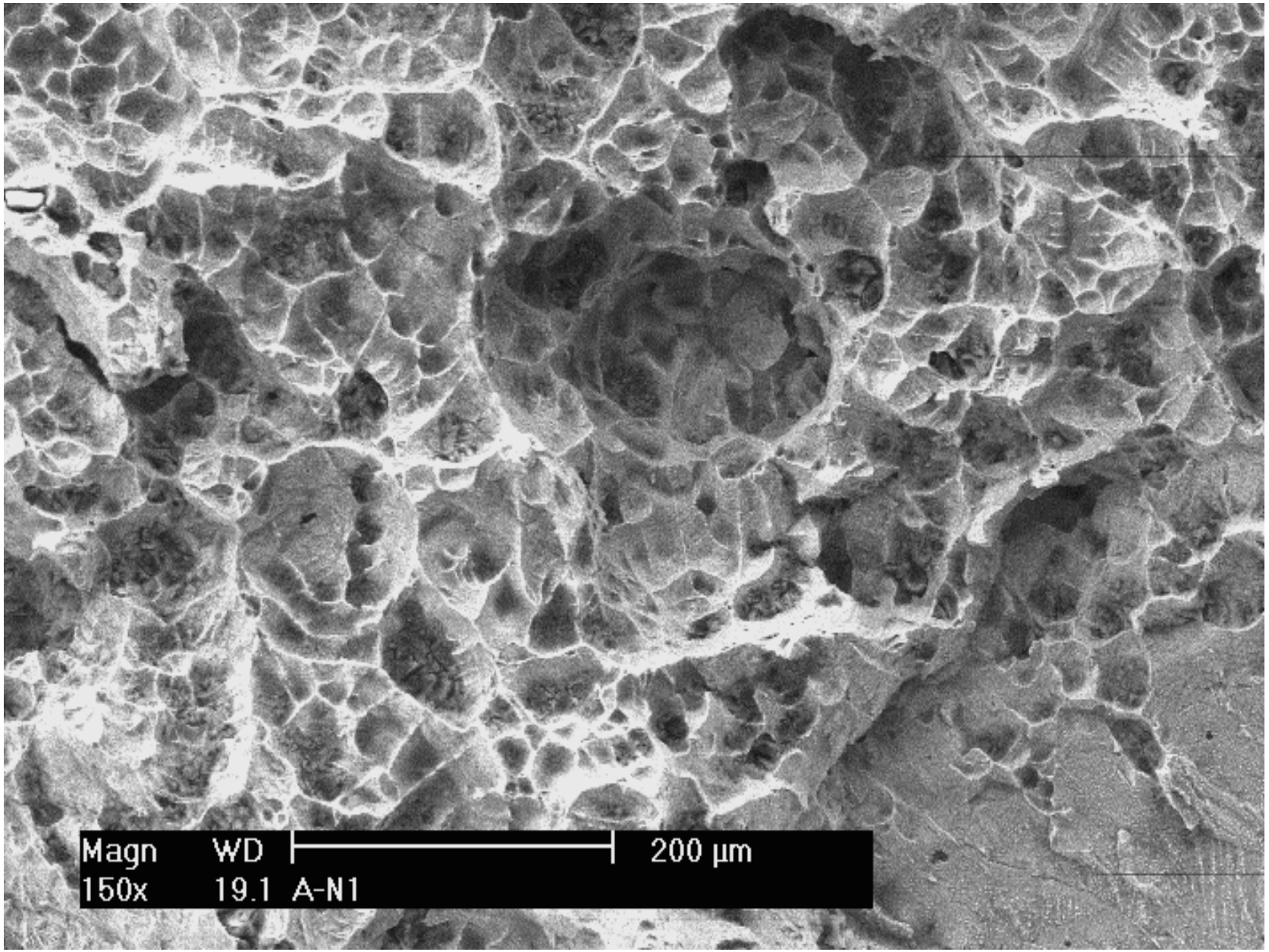

Figure 12. Ductile dimple fracture in JR test region of specimen A-N1.

Field Co

3.1.1.2 Irradiated specimen A-1 tested in simulated PWR water

Crack growth rate test

Specimen A-1 was an irradiated CF-3 CASS sample (Heat 69) tested in the simulated PWR water environment. The specimen had ~24% ferrite and was in the as-cast condition. The objective of this test was to compare the results with those from an identical test performed in low-DO high-purity water. Also, the CGR results of this sample were compared with those obtained from its thermally aged equivalent. The test conditions and results are summarized in Table 5, and a crack-length history plot is shown in Fig. 13. Note that the starting crack length for this sample was about 1 mm longer than that of a typical 1/4T-CT specimen. This larger-than-normal initial crack length was due to a restart of the pre-cracking to correct a loose DCPD lead. The initial crack size reported in Table 5 was determined with SEM images on the fracture surface after the test.

Table 5. Crack growth rates of specimen A-1 (0.08-dpa unaged CF-3 sample with 24% δ ferrite) in PWR water.[a]

Test Period	Test Time, h	Test Temp., °C	Load Ratio	Rise Time, s	Return Time, S	Hold Time, s	Kmax, MPa $m^{1/2}$	ΔK, MPa $m^{1/2}$	CGR in Env., m/s	CGR in Air, m/s	Crack Length, mm
Start	63.9										6.802 [b]
a	64.8	319	0.21	0.43	0.43	0.07	24.3	19.2	1.58E-07	2.04E-07	7.009
b	66	319	0.31	0.41	0.41	0.09	23.8	16.4	1.17E-07	1.43E-07	7.218
c	68.6	319	0.41	0.78	0.78	0.22	23.1	13.6	3.21E-08	4.47E-08	7.340
d	72.3	319	0.41	1.54	1.54	0.46	21.9	12.8	9.77E-09	1.89E-08	7.395
e	87.6	319	0.46	2.96	1.48	1.04	20.3	11.0	2.89E-10	6.18E-09	7.403
f	91	319	0.41	3.08	1.54	0.92	22.2	13.1	9.46E-09	1.01E-08	7.462
g	94.1	320	0.41	7.69	1.54	2.31	22.4	13.2	5.67E-09	4.17E-09	7.503
h	103	320	0.46	22.6	3.76	7.42	22.6	12.2	1.51E-09	1.16E-09	7.535
i	114.3	320	0.46	45.1	3.76	14.9	22.7	12.3	7.63E-10	5.86E-10	7.558
j	118.7	319	0.41	15.3	3.83	4.66	23.0	13.6	4.61E-09	2.27E-09	7.602
k	127.9	319	0.41	46.0	3.83	14.0	23.0	13.7	1.25E-09	7.72E-10	7.632
l	150.3	318	0.40	114.9	9.19	35.1	23.0	13.7	3.90E-10	3.13E-10	7.655
m	168.7	319	0.40	385.6	9.25	114.4	23.9	14.3	3.56E-10	1.05E-10	7.673
1	209	318	0.40	12	12	7200	23.9	14.4	4.83E-11	5.75E-12	7.684

[a] Simulated PWR water with 2 ppm Li and 1000 ppm B. DO<10 ppb. Conductivity ~20 μS/cm.

[b] Determined from the SEM image after the test.

The specimen was pre-cracked in the PWR environment with a triangular waveform at 1 Hz, a maximum stress intensity factor of ~24 MPa $m^{1/2}$, and load ratio of 0.2. After about 200 μm extension, the load ratio was increased while the stress intensity factor and cyclic frequency were reduced gradually. The measured CGRs in the initial stage of the pre-cracking (test periods *a-d*) followed closely with the fatigue growth rates in air. Next, several test periods were carried out with saw-tooth waveforms and increased rise times to stimulate environmentally assisted cracking. The environmental enhancement of CGRs started to appear and became stabilized after some additional crack extension. The cyclic CGR data obtained from this test are plotted against the estimated fatigue CGRs in air as shown in Fig. 14. The corrosion fatigue curve proposed by Shack and Kassner is also included in the figure as a reference. Obviously, the

corrosion fatigue response of this sample is lower than that of typical SSs, suggesting good IASCC resistance of CASS in PWR water.

After the cyclic CGR test, the specimen was subjected to a constant stress intensity factor of ~24 MPa $m^{1/2}$ with PPU every 2 hours. The measured SCC CGR was about 4.8×10^{-11} m/s, a factor of four lower than that of the NUREG-0313 curve,[3636] a SCC disposition curve based on unirradiated SSs tested in a high-DO environment. The SCC response of this sample will be discussed at the end of this section along with the other CGR data obtained from the same heat.

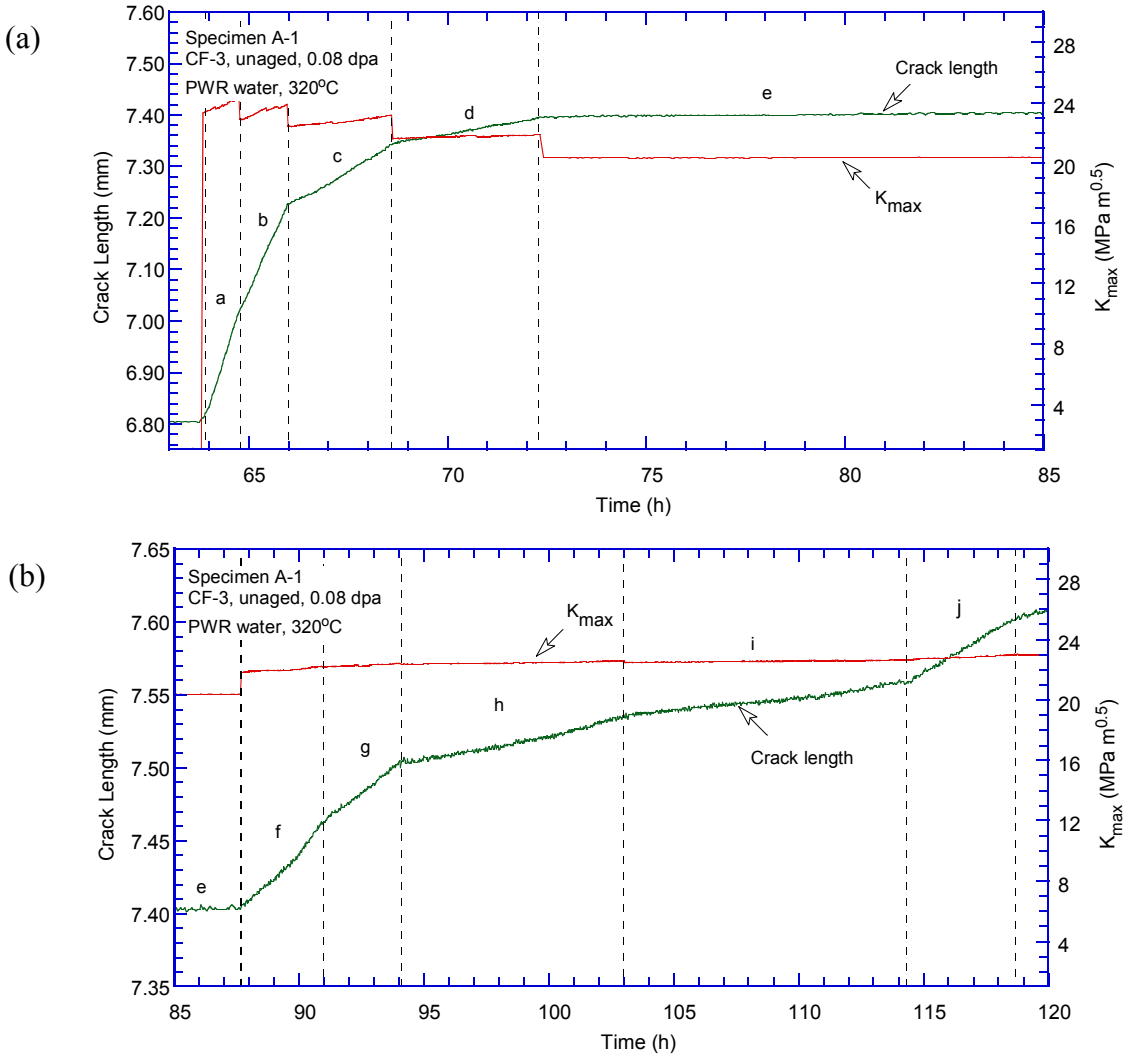

Figure 13. Crack-length-vs.-time plot for specimen A-1 (0.08-dpa unaged CF-3 with 24% ferrite): test periods (a) a-e, (b) f-j, (c) k-m, and (d) 1.

(c)

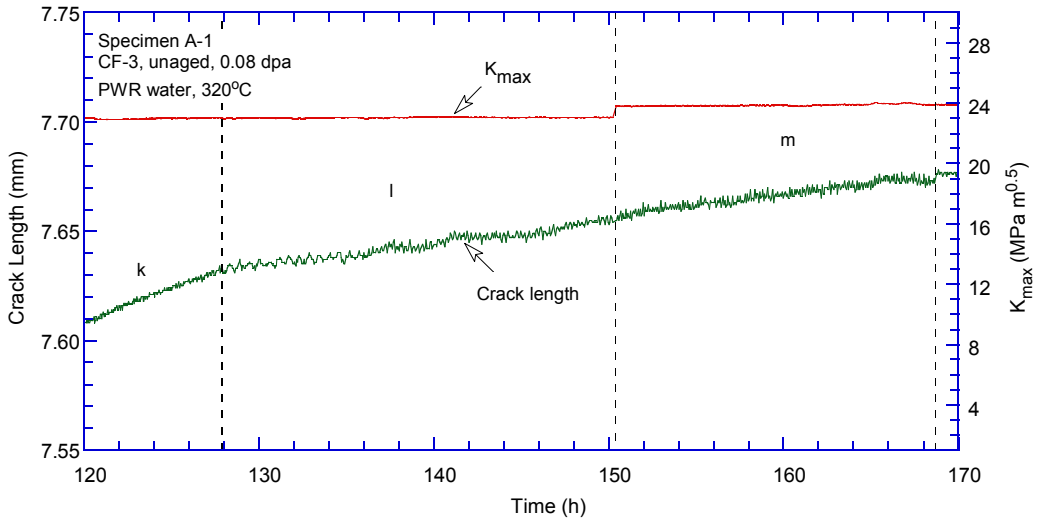

(d)

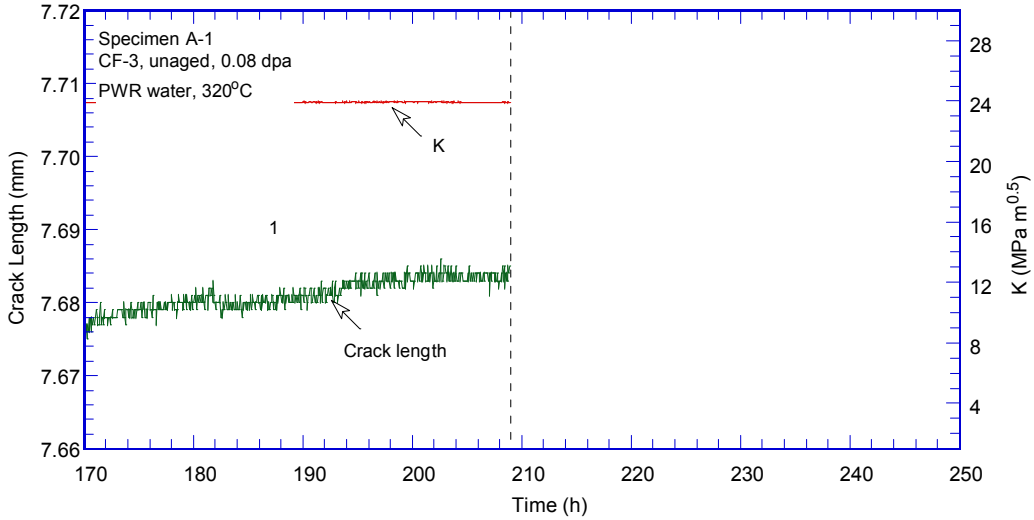

Figure 13. (Contd.)

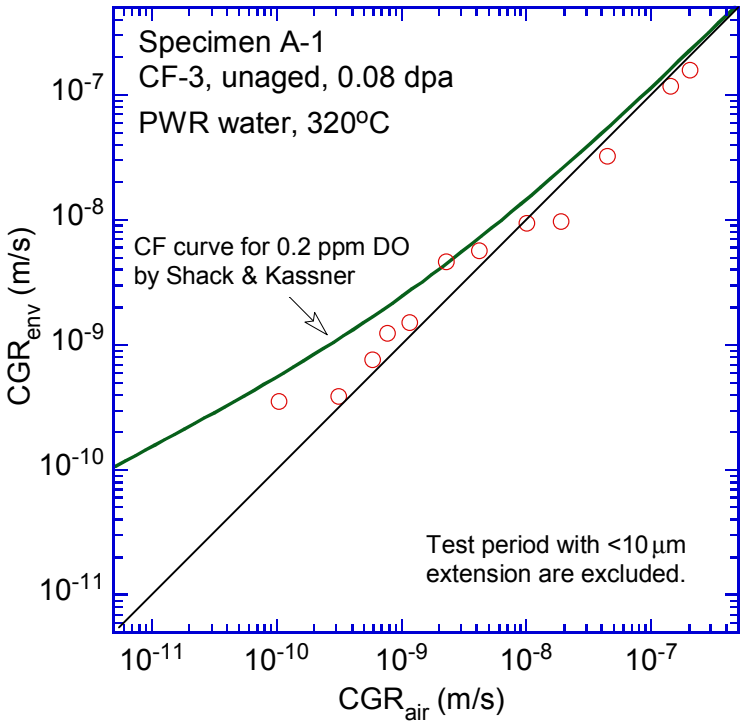

Figure 14. Cyclic CGRs of specimen A-1.

Field Co

Fractographic examination

After the test, the specimen was pulled apart in an air atmosphere at room temperature, and the fracture surface was examined with SEM. Figure 15 shows the entire crack front of specimen A-1. The straight line in the middle of the picture corresponds to the restart of the pre-cracking. Figure 16 is an enlarged view along the central section of the specimen. Transgranular cleavage-like fracture is the dominant morphology throughout the CGR region. Figure 17 shows the typical river pattern of cleavage cracking at the beginning and the end of the CGR test region. Vermicular ferrite at dendrite cores can also be seen in a few places on the fracture surface. As shown in Fig. 18, fewer slip ledges can be seen within ferrite, suggesting that the ferrite dendrite core might be deformed to a lesser extent than the surrounding austenite. Beyond the CGR test, the dominant fracture mode is ductile dimples resulting from microvoid coalescence.

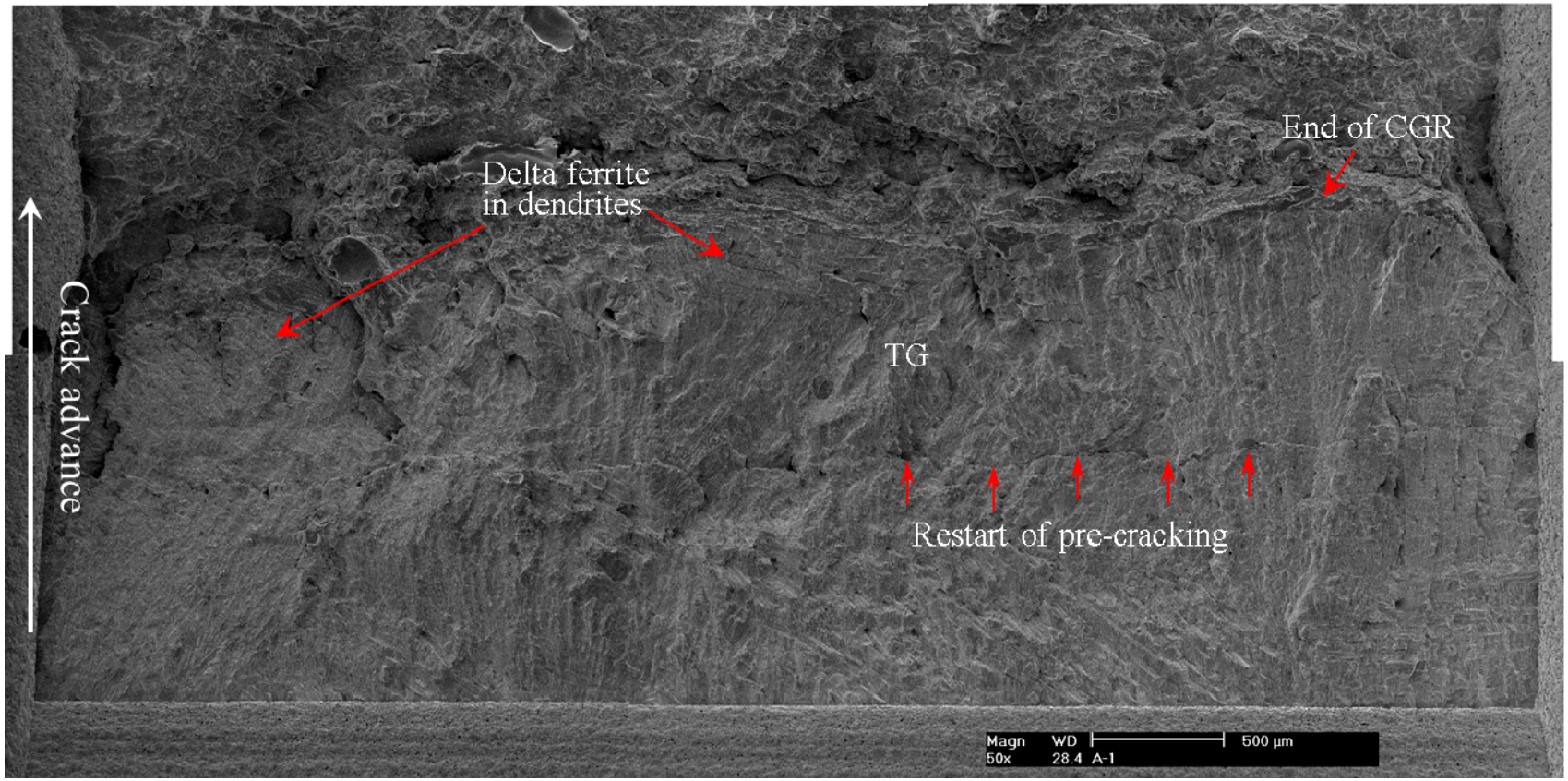

Figure 15. Fracture surface of specimen A-1 tested in PWR water.

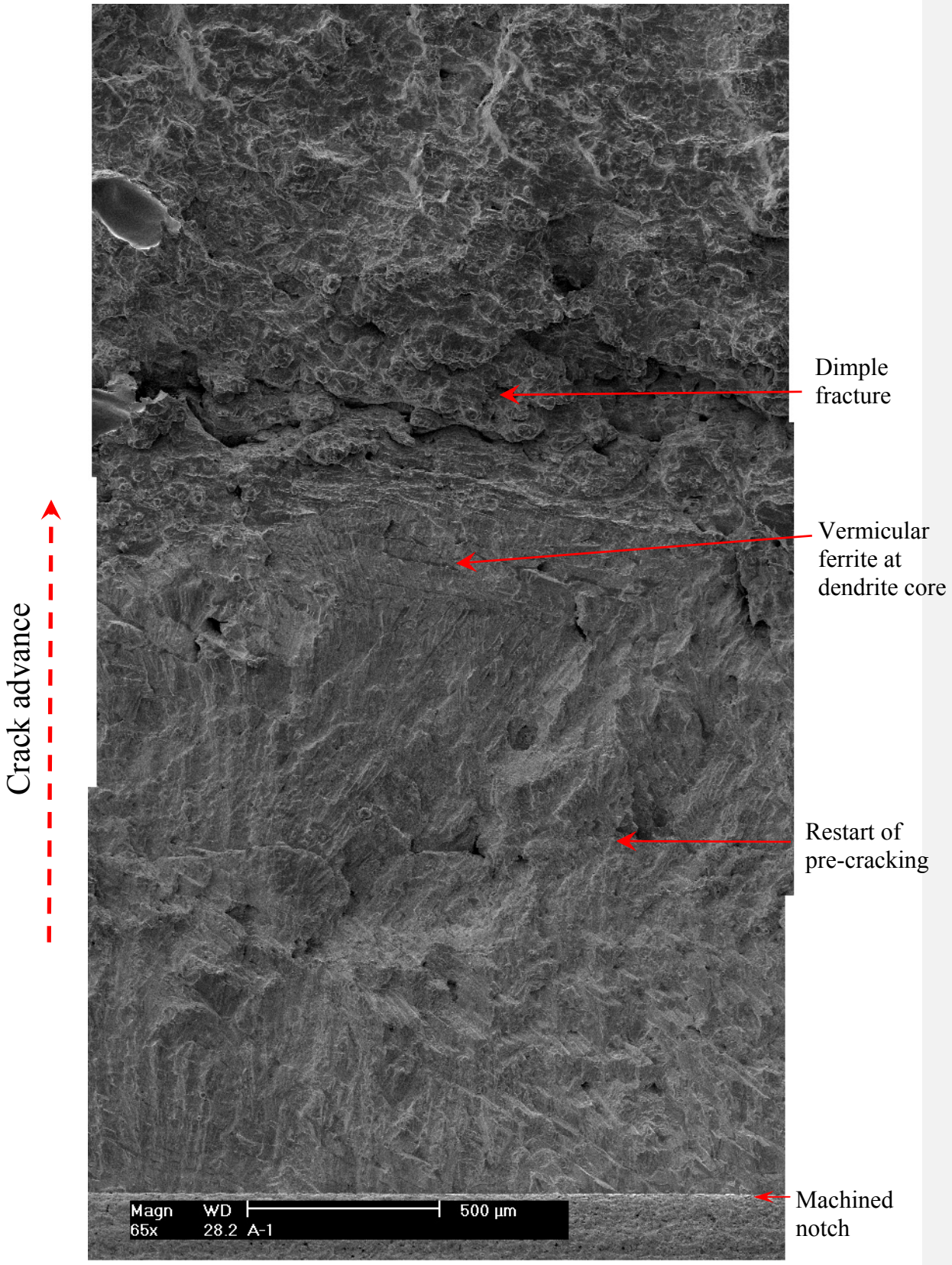

Figure 16. Fracture surface of specimen A-1 along the sample central line.

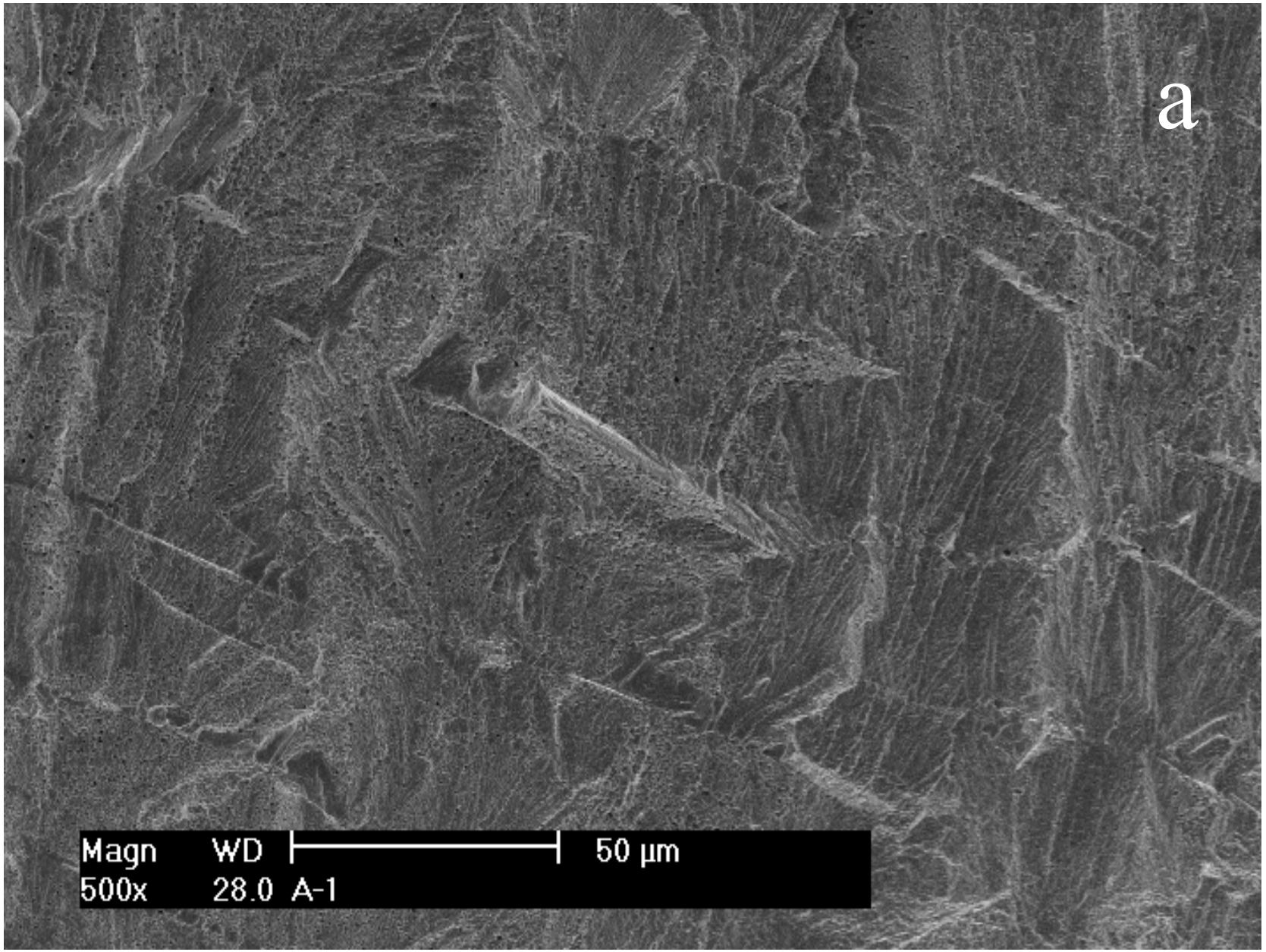

Figure 17. Cleavage-like fracture in specimen A-1: (a) pre-cracking, and (b) end of the CGR test. Crack propagation from bottom to top.

Field Co

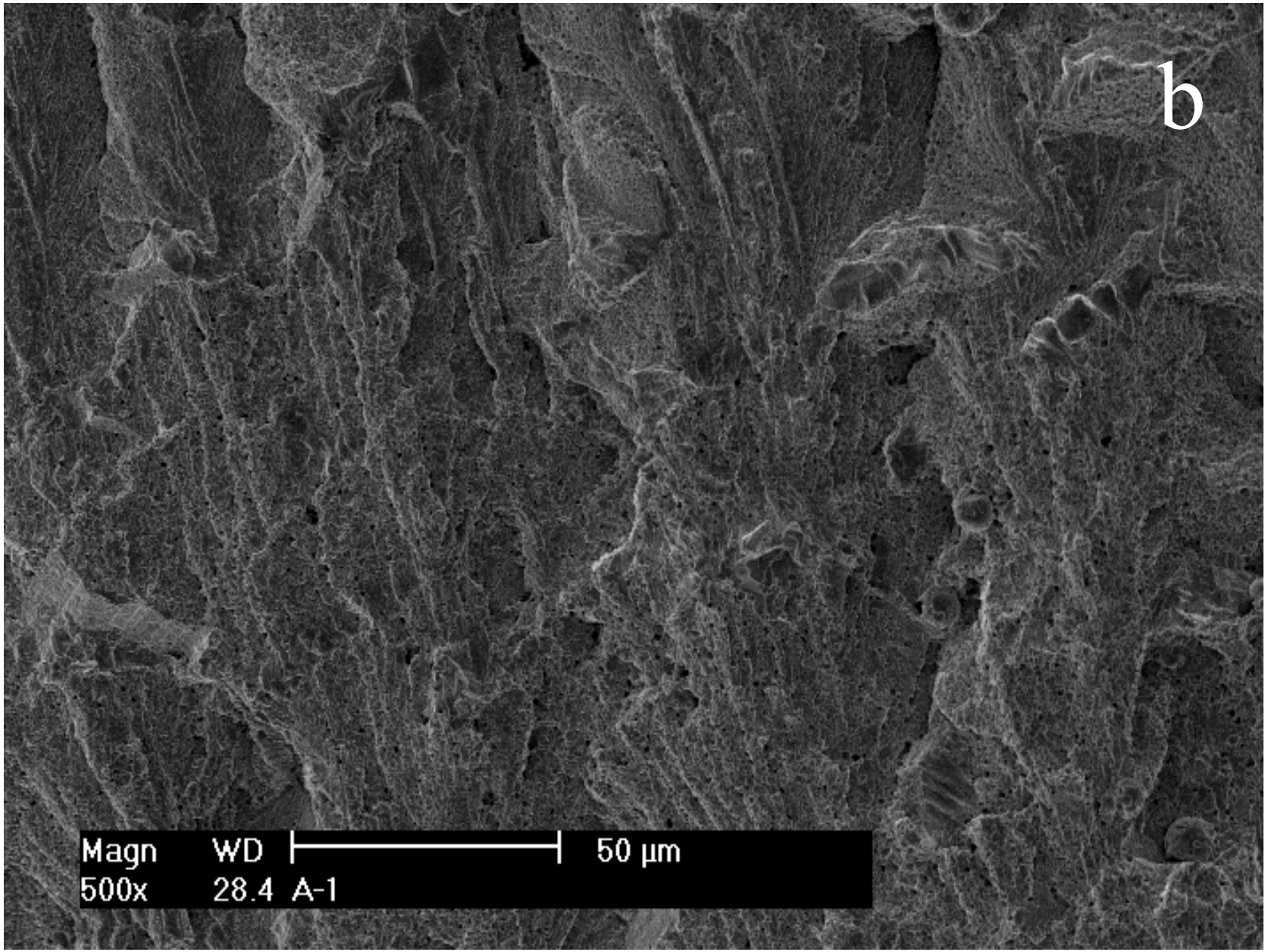

Figure 17. (Contd.)

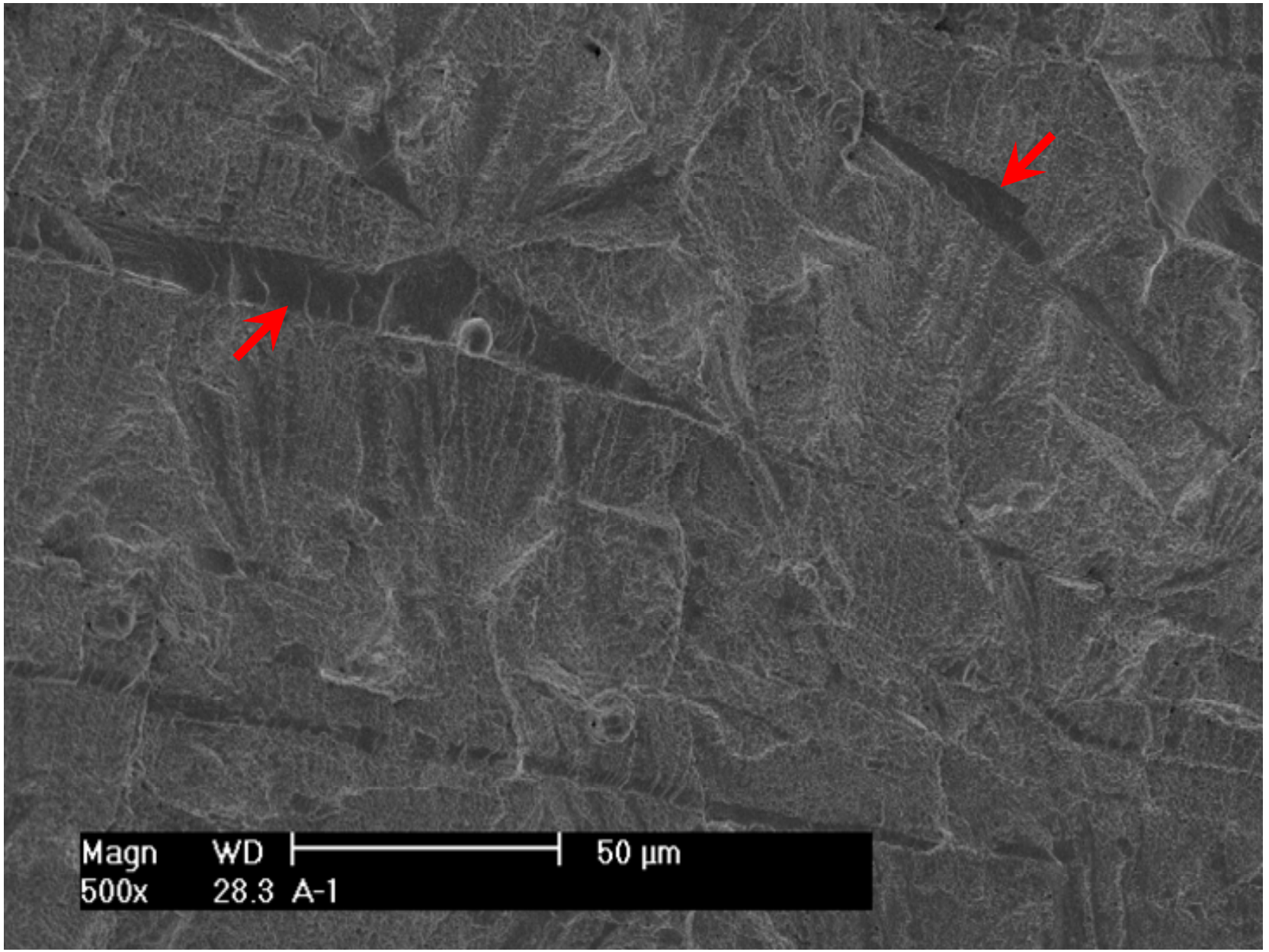

Figure 18. Fracture surface of specimen A-1 showing that delta ferrite deformed to a lesser extent than austenite. Crack propagation from bottom to top.

3.1.1.3 Irradiated specimen A-2 tested in low-DO high-purity water

Crack growth rate test

Specimen A-2 was an irradiated unaged CF-3 CASS with ~24% ferrite (Heat 69) tested in high-purity water with low DO. The objective of this test was to compare the irradiated specimen A-1 tested in PWR water. Also, the fracture toughness of this specimen was compared with that of thermally aged CF-3 CASS. The CGR test conditions and results are summarized in Table 6, and a crack-length history plot is shown in Fig. 19.

Table 6. Crack growth rates of specimen A-2 (0.08-dpa unaged CF-3 with 24% δ ferrite) in low-DO high-purity water environment.

Test Period	Test Time, h	Test Temp., °C	Load Ratio	Rise Time, s	Return Time, s	Hold Time, s	Kmax, MPa $m^{1/2}$	ΔK, MPa $m^{1/2}$	CGR in Env., m/s	CGR in Air, m/s	Crack Length, mm
Start	14.9										5.899
a[a]	18.1	319	0.34	0.45	0.45	0.05	17.3	11.4	4.09E-08	4.04E-08	6.041
b	20	319	0.41	0.45	0.45	0.05	17.1	10.1	3.21E-08	2.96E-08	6.141
c	21.6	319	0.50	0.43	0.43	0.07	15.7	7.8	1.94E-09	1.43E-08	6.151
d[a]	24.3	319	0.45	0.44	0.44	0.06	16.5	9.1	2.27E-08	2.16E-08	6.219
e	30.4	319	0.45	0.88	0.88	0.12	16.0	8.8	5.26E-09	9.85E-09	6.274
f	39.3	319	0.50	1.74	1.74	0.26	15.9	8.0	1.80E-09	3.82E-09	6.304
g	40.4	319	0.40	0.45	0.45	0.05	17.2	10.4	5.87E-08	3.21E-08	6.410
h	42.4	319	0.45	0.44	0.44	0.06	16.3	9.0	1.25E-08	2.13E-08	6.453
i	44.6	319	0.45	0.88	0.88	0.12	16.6	9.2	1.29E-08	1.14E-08	6.497
j	49.0	319	0.45	1.75	1.75	0.25	16.8	9.2	9.20E-09	5.84E-09	6.564
k	62.2	319	0.45	4.38	4.38	0.62	17.0	9.4	3.07E-09	2.45E-09	6.627
l	74.2	319	0.46	8.73	4.37	1.27	17.2	9.4	2.37E-09	1.23E-09	6.686
m	88.4	319	0.45	26.2	4.37	3.79	17.2	9.5	7.77E-10	4.25E-10	6.719
n	110.6	319	0.44	52.5	10.5	7.52	17.2	9.7	6.45E-10	2.24E-10	6.756
o	135.7	319	0.43	105.0	10.5	15.0	17.0	9.7	3.77E-10	1.13E-10	6.780
p	184.3	319	0.43	262.6	10.5	37.4	17.3	9.8	8.72E-11	4.69E-11	6.795
q	232.7	319	0.43	525.9	10.5	74.1	17.6	10.0	1.29E-10	2.49E-11	6.815
r	278.6	320	0.43	876.3	10.5	123.7	17.6	10.1	1.73E-10	1.52E-11	6.840
s	326.7	319	0.48	865.9	10.4	134.1	17.6	9.2	1.27E-10	1.21E-11	6.860
1	423.9	319	0.50	12	12	7200	17.6	8.8	2.33E-11	1.27E-12	6.875
2-a	575.3	320	0.50	12	12	7200	19.6	9.8	4.89E-11	1.80E-12	6.907
2-b	687.3	321	1	-	-	-	19.8	-	4.94E-12	-	6.912
2-c	784	321	0.50	12	12	3600	19.8	9.9	4.26E-11	3.73E-12	6.924

[a] The CGR value was obtained from the later part of the test period.

Pre-cracking in this sample was started with a triangle waveform at 1 Hz. The applied maximum stress intensity factor and load ratio were ~17 MPa $m^{1/2}$ and ~0.35, respectively. The initial cyclic CGRs were comparable to fatigue growth rates but were quickly diminished as the load ratio was increased to 0.5. After lowering the load ratio of 0.4 and increasing the frequency to 1 Hz, the high growth rate was re-established in test period *g* over a 100-μm crack extension. Next, the rise time was increased gradually while the maximum stress intensity factor and load ratio were kept approximately the same. In the following test periods, environmentally enhanced cracking started to appear and became evident with further increases in rise time and load ratio. By the end of test period *s*, the measured CGR was more than one order of magnitude higher than the fatigue growth rate in air. All cyclic CGRs obtained from this sample are plotted in

Fig. 20 along with the corrosion fatigue curve for unirradiated SSs in water with 0.2 ppm DO. A comparison between Figs. 14 and 20 shows that the cyclic CGRs of specimen A-1 is slightly lower than that of specimen A-2.

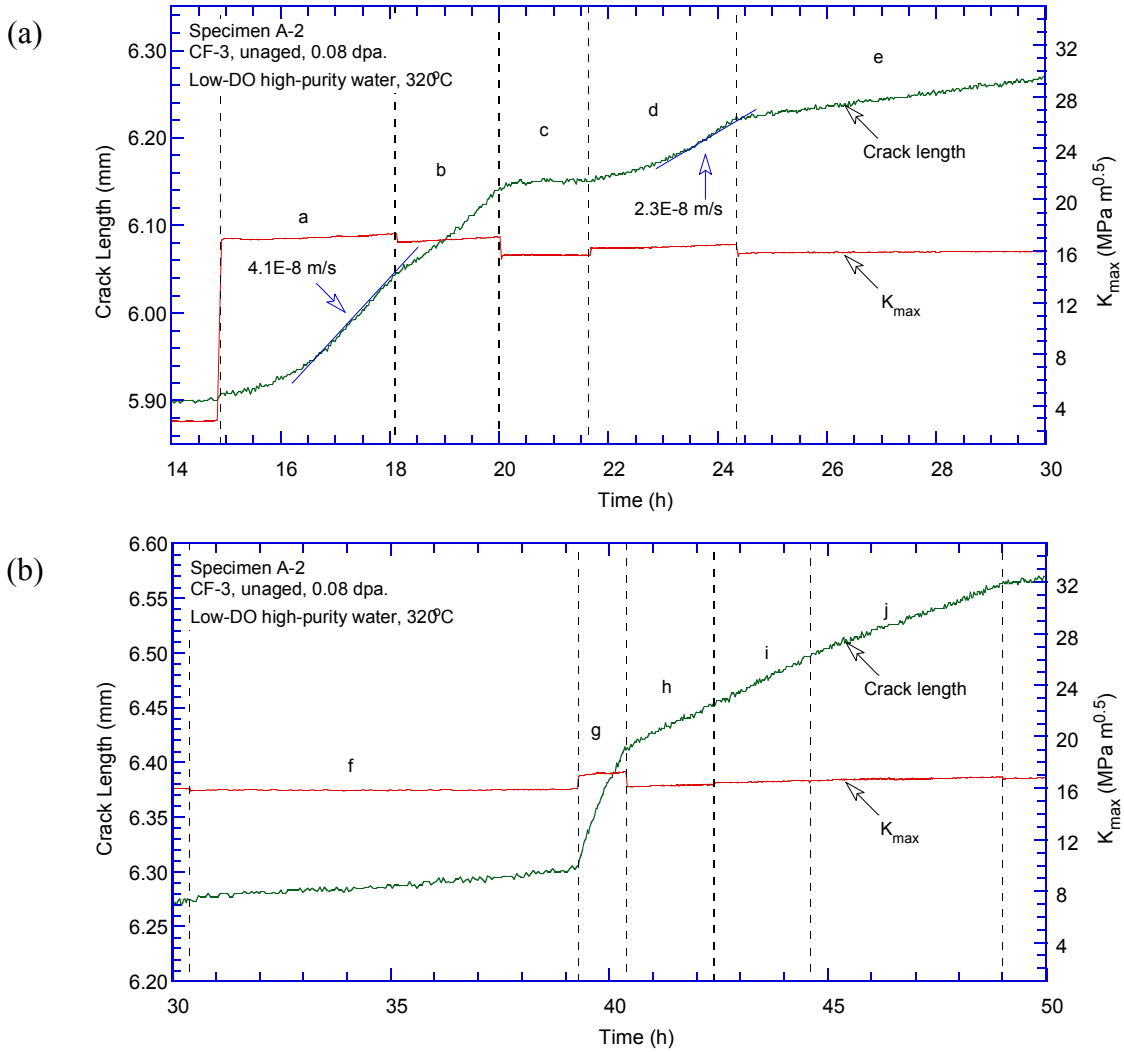

Figure 19. Crack-length-vs.-time plot for specimen A-2 (0.08-dpa unaged CF-3 with 24% ferrite) tested in low-DO high-purity water environment: test periods (a) a-e, (b) f-j, (c) k-o, (d) p-s, and (e) 1-2.

(c)

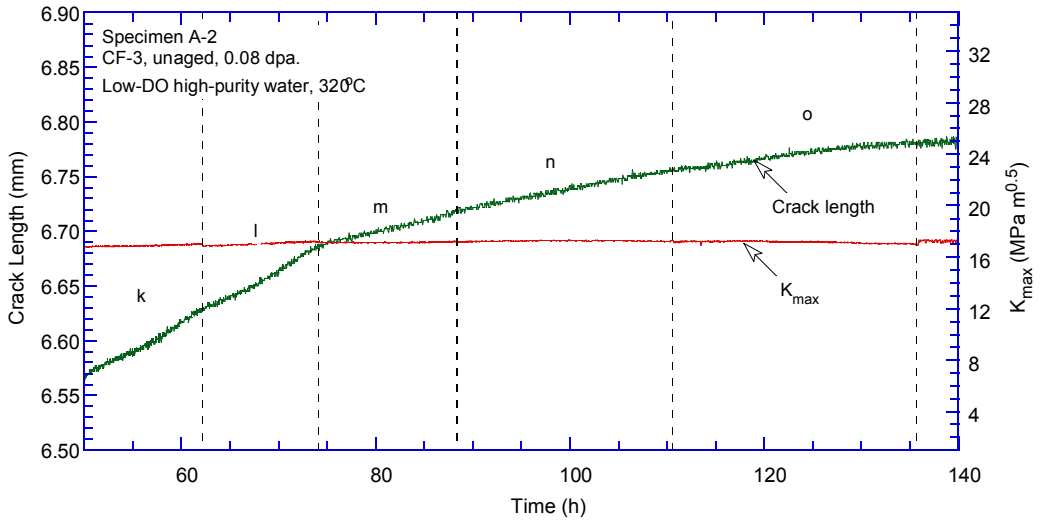

(d)

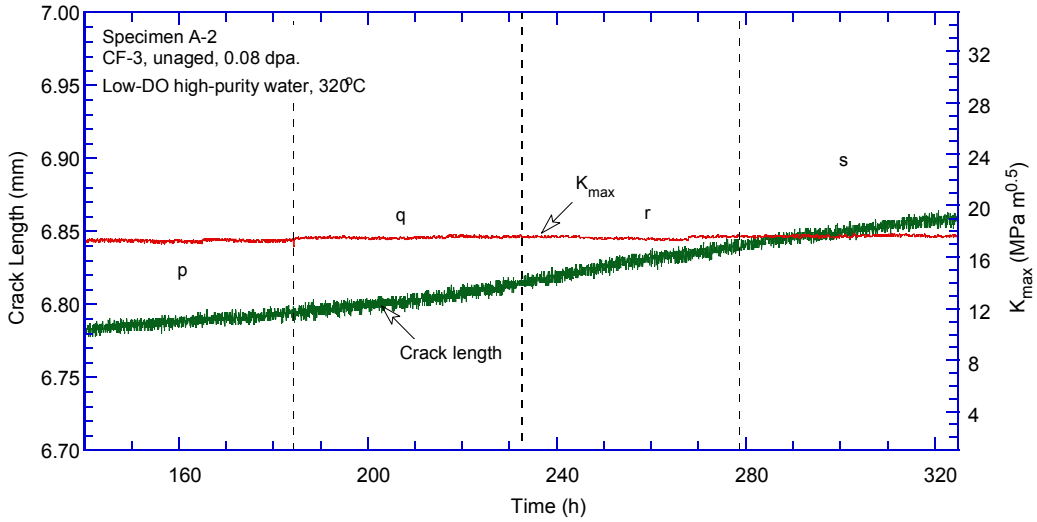

(e)

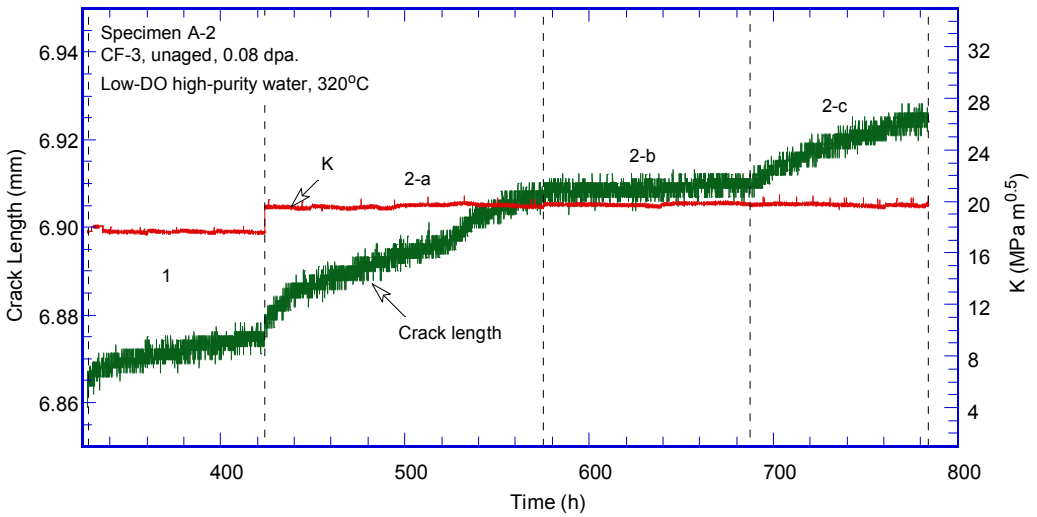

Figure 19. (Contd.)

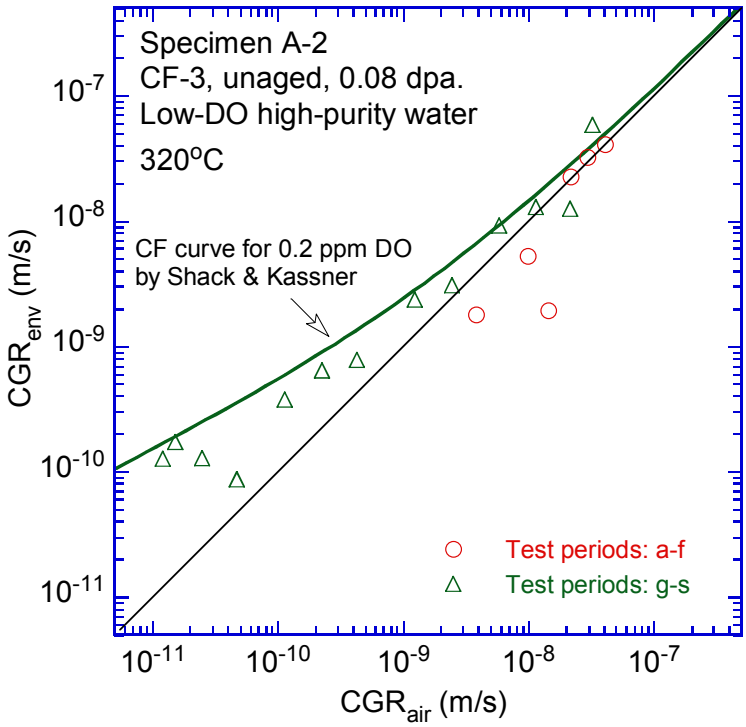

Figure 20. Cyclic CGRs of specimen A-2.

The first constant-load test period was conducted at 17.6 MPa $m^{1/2}$ with PPU every 2 hr (test period *1*). After nearly 100 hr, a CGR of 2.3 x 10^{-11} m/s was measured over ~15-µm crack extension. The load was increased to 19.6 MPa $m^{1/2}$ for the second constant-load test period. Again, PPU was applied every 2 hr. A CGR of 4.9 x 10^{-11} m/s was obtained over 150 hr. After the PPU was removed in test period *2-b*, the measured CGR decreased one order of magnitude. Constrained by test time, only 5-µm crack extension was accumulated for this test period. In test period *2-c*, the PPU was re-introduced but with 1-hour interval. The measured CGR was nearly identical to that obtained in test period *2-a*. It appears that the hold time between PPU does not affect the SCC response of CF-3 at this stress intensity level.

Fracture toughness J-R curve test

After the crack growth test, a fracture toughness J-R curve test was conducted on this sample in the low-DO high-purity water environment. The sample was loaded at a constant extension rate of 0.43 µm/s while the load and load-line displacement were recorded. During the test, loading was interrupted periodically to measure the crack extension by DCPD. The obtained J and crack extension data are plotted in Fig. 21. A power-law curve fitting of the data gives a relationship of $J = 430\Delta a^{0.64}$. The estimated J value at the 0.2-mm offset line is about 204 kJ/m^2. Note that the J-R curve data cannot be validated for this sample because one of the nine measurements of the final crack size was above the limit, and the J_{max} requirement was omitted in this analysis.

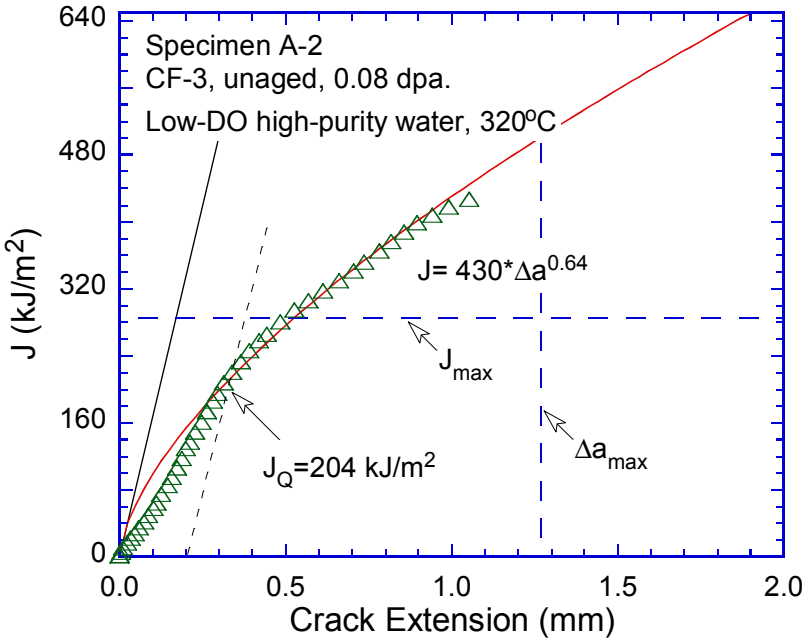

Figure 21. The J-R curve for specimen A-2.

Field Co

Fractographic examination

After the J-R curve test, the sample was cyclically loaded at room temperature in an air atmosphere to break the ligament. The fracture surface was then examined with the replication technique using SEM. Figure 22 shows the entire fracture surface of specimen A-2. Note that the round smooth areas on the SEM image are air bubbles trapped during replication, not the original morphology of the fracture surface. Both the CGR and post-JR fatigue regions are relatively flat, clearly contrasting with the heavily deformed JR region. The crack front of the CGR test is straight, indicating a well-controlled loading condition during the CGR test. A curved crack front due to a non-constant constraint can be seen for the JR test region.

Figure 23 shows an enlarged view of specimen A-2 along its central line. Similar to specimen A-1, which was tested in PWR water, transgranular cleavage-like fracture was also the dominant morphology during the CGR test. Figure 24~~24~~ shows the cleavage-like cracking at the initial part of the CGR test, and deformation steps resulting from brittle fracture can be seen in some places. An area of delta ferrite at the dendrite cores can be seen close to the end of the CGR test (see Fig. 25~~25~~). Similar to that found in the specimen A-1, less plastic deformation activities were observed in the ferrite phase. Beyond the CGR test, ductile dimples were the only fracture morphology on the fracture surface, as shown in Fig. 26~~26~~.

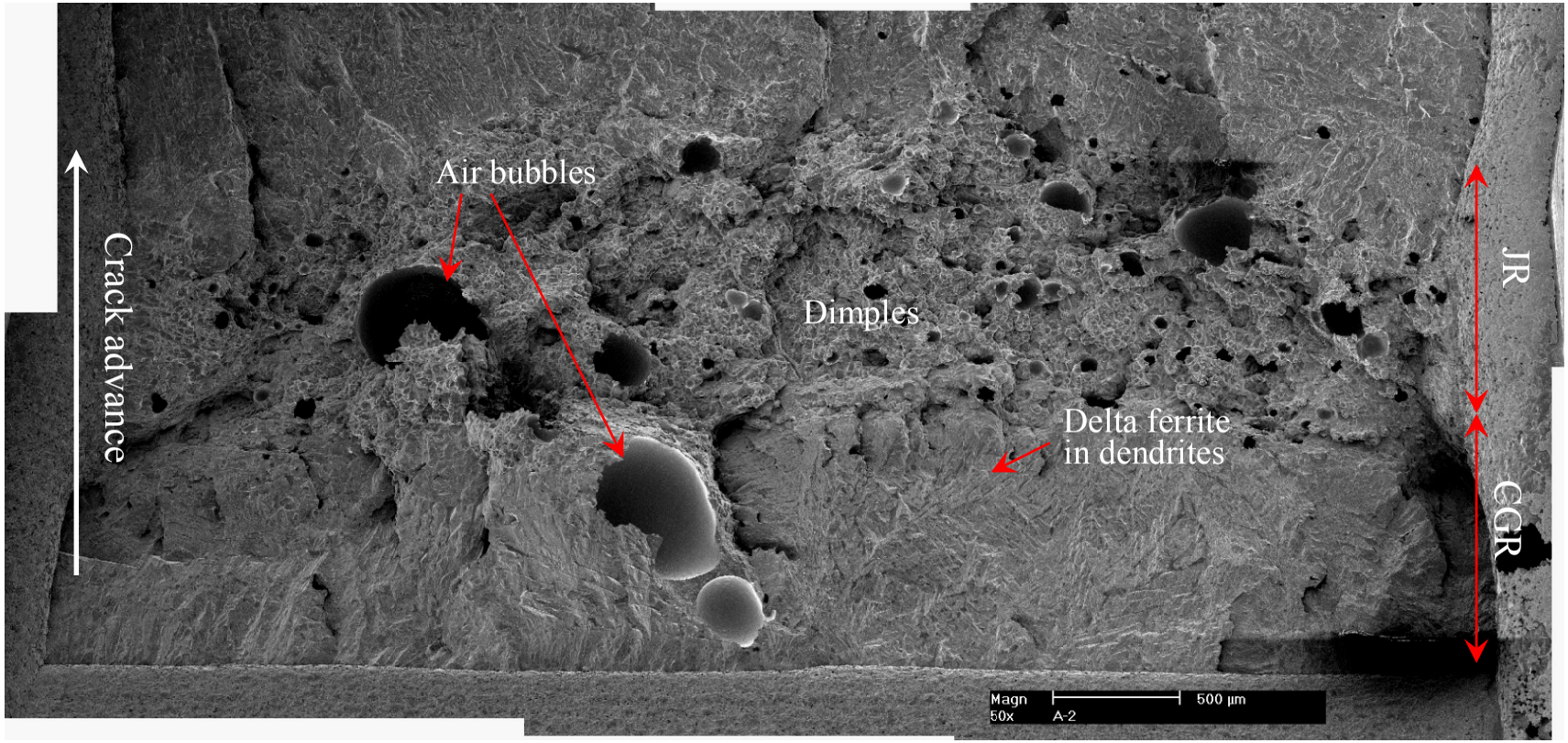

Figure 22. Fracture surface of specimen A-2 tested in low-DO high-purity water.

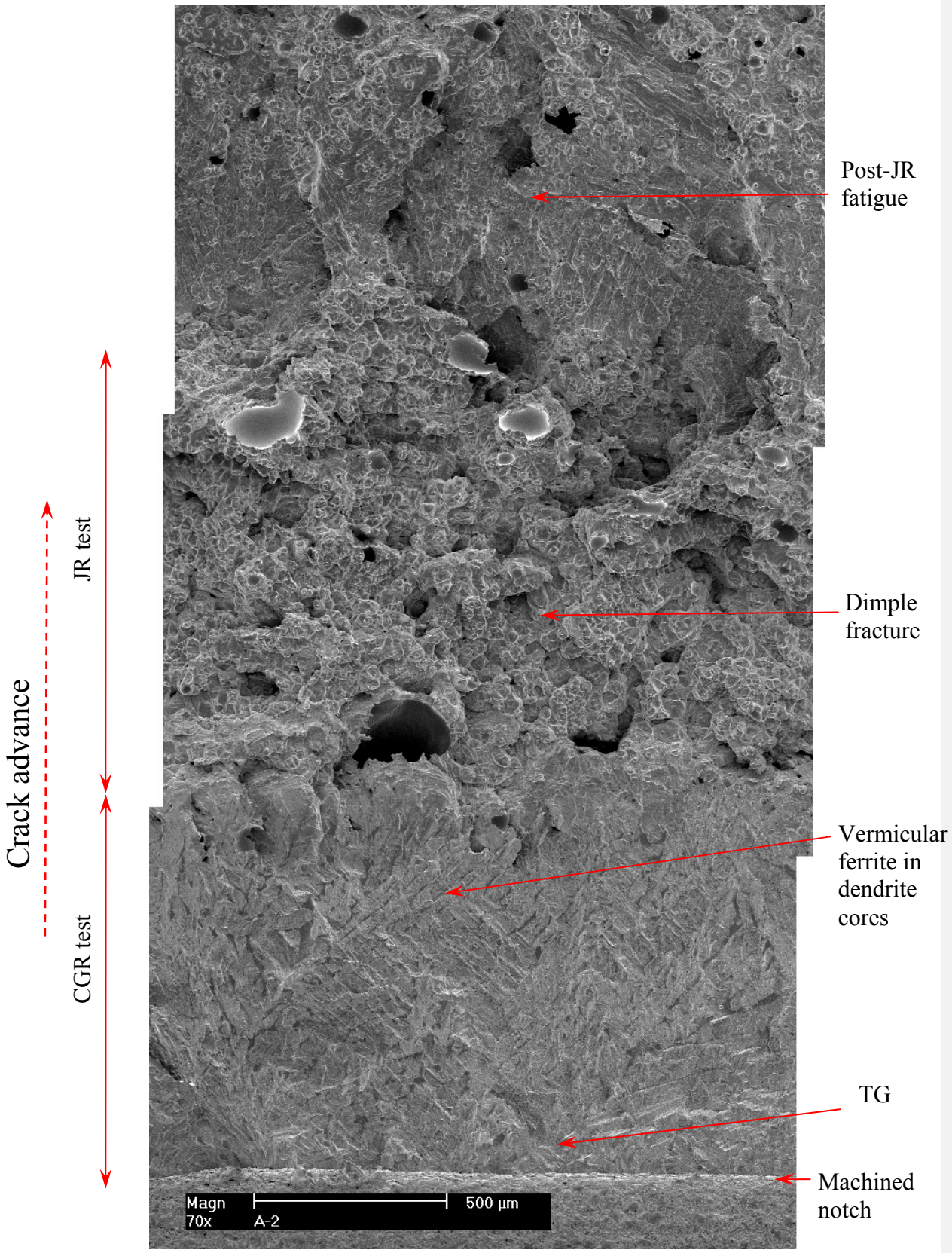

Figure 23. Fracture surface of specimen A-2 along the sample central line.

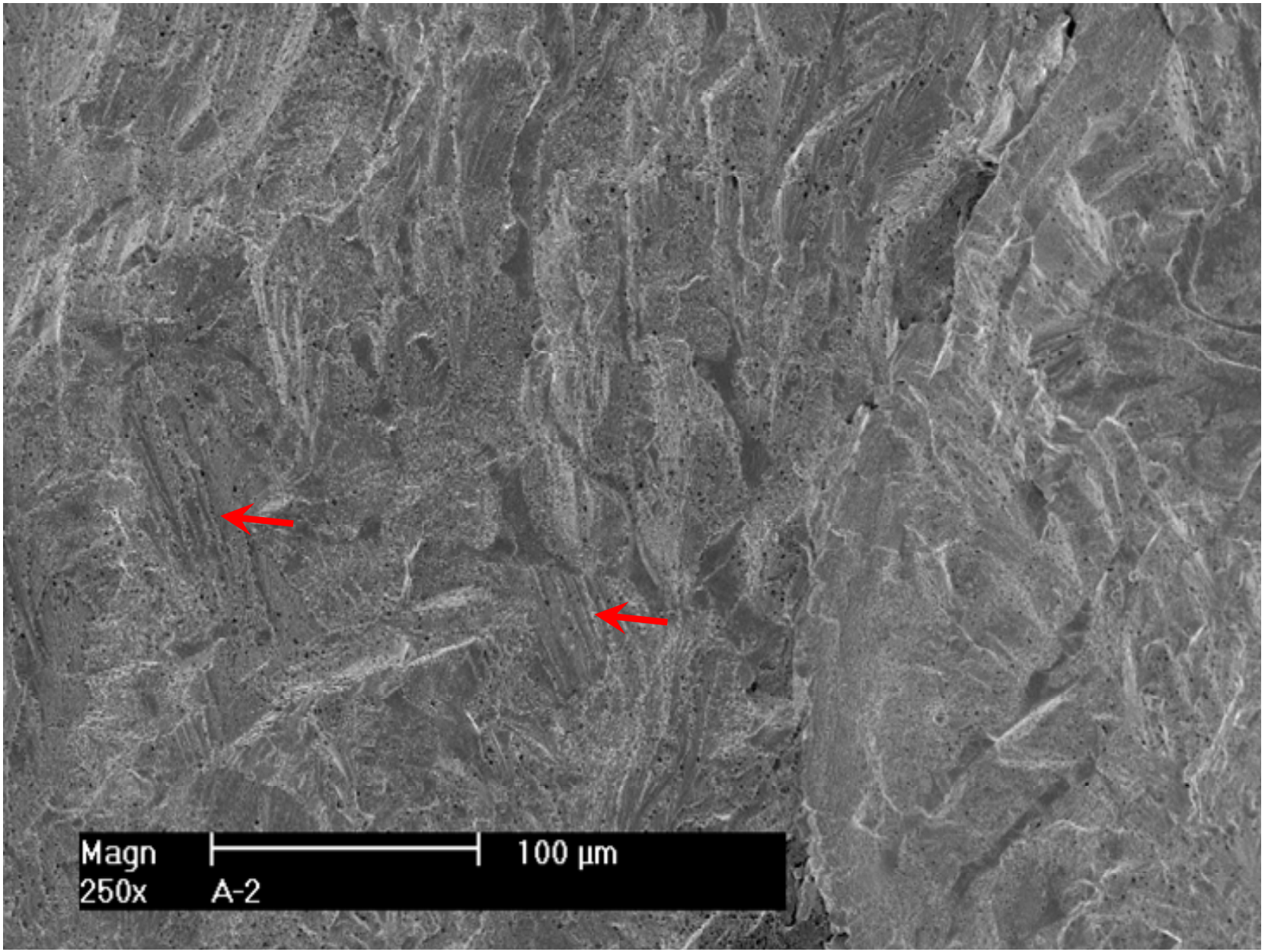

Figure 24. Cleavage-like steps at the beginning of CGR test of specimen A-2. Crack propagation from bottom to top.

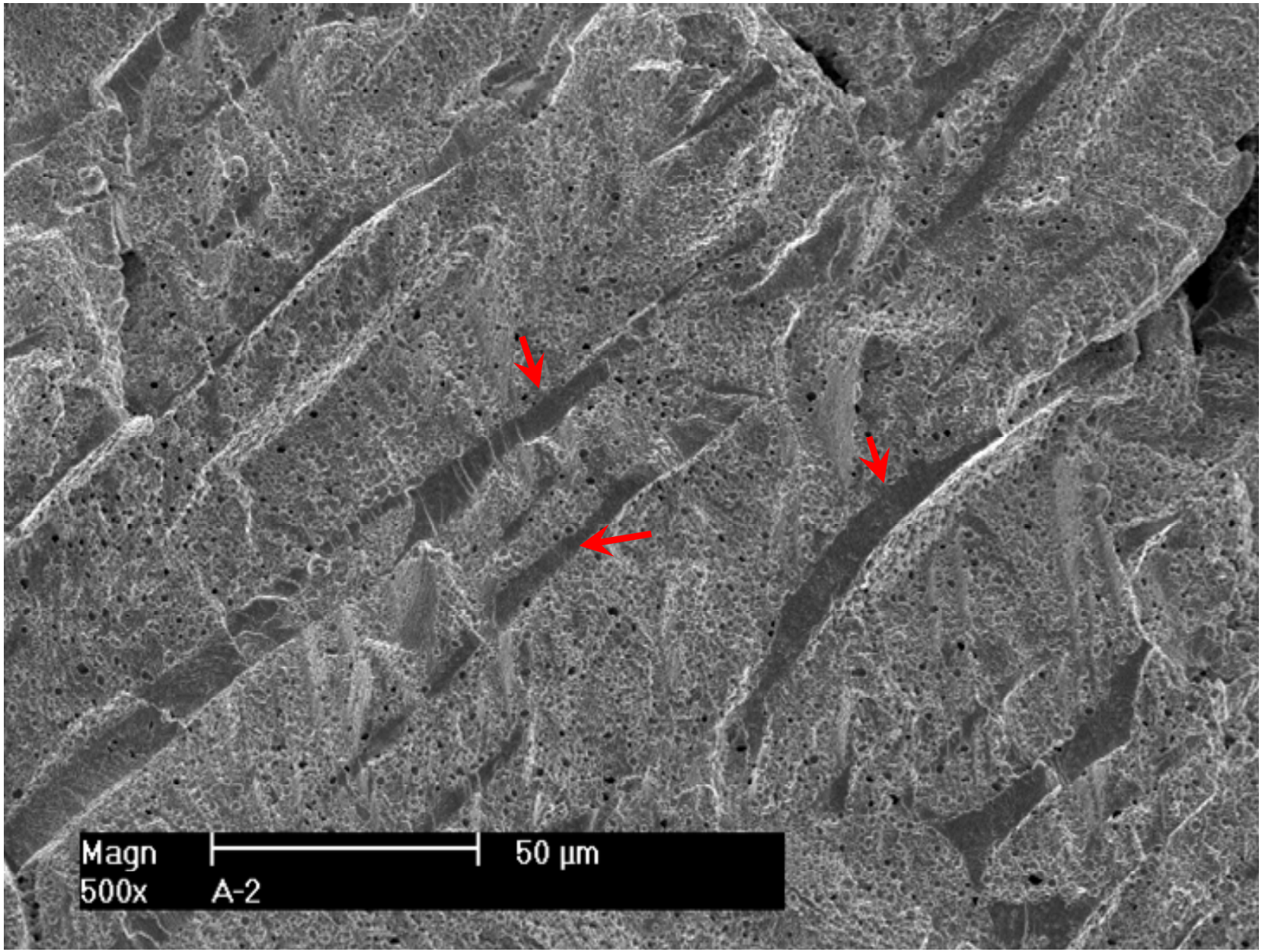

Figure 25. Fracture surface of specimen A-2 showing that ferrite deformed to a lesser extent than austenite. Crack propagation from bottom to top.

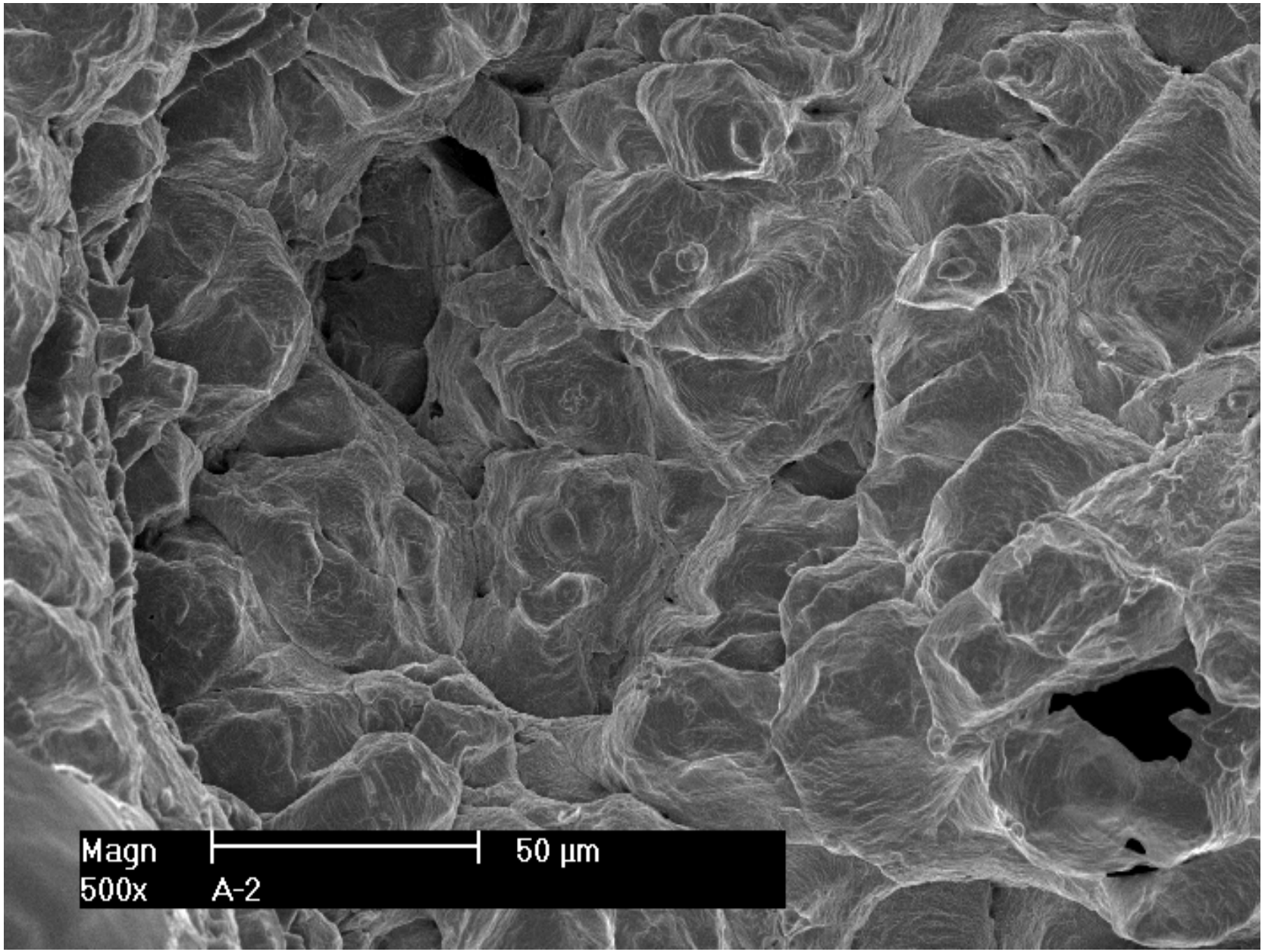

Figure 26. Ductile dimple morphology in the JR test region of specimen A-2. Crack propagation from bottom to top.

3.1.2 Thermally Aged CF-3 CASS

3.1.2.1 Unirradiated specimen B-N1 tested in PWR water

Crack growth rate test

Specimen B-N1 was an unirradiated control sample tested in PWR water. The material was a thermally aged CF-3 with ~24% ferrite. The objective of the test was to provide a baseline for irradiated tests on thermally aged specimens. The CGR test conditions and results of this sample are summarized in Table 7, and a crack-length history plot is shown in Fig. 27.

Table 7. CGR test of specimen B-N1 (unirradiated, thermally aged CF-3 with 24% δ ferrite) in PWR water.[a]

Test Period	Test Time, h	Test Temp., °C	Load Ratio	Rise Time, s	Return Time, s	Hold Time, s	Kmax, MPa $m^{1/2}$	ΔK, MPa $m^{1/2}$	CGR in Env., m/s	CGR in Air, m/s	Crack Length, mm
Start	0.3										5.997
a [b]	3.0	319	0.20	0.43	0.43	0.07	14.8	11.9	5.57E-08	4.04E-08	6.182
b [b]	7.2	319	0.35	0.42	0.42	0.08	15.0	9.8	3.25E-08	2.67E-08	6.353
c [b]	13.3	319	0.49	0.40	0.40	0.10	15.1	7.7	2.19E-08	1.45E-08	6.474
d	23	319	0.54	0.77	0.77	0.23	15.0	6.9	4.85E-09	5.50E-09	6.538
e	47	319	0.54	1.92	1.92	0.58	15.0	6.9	1.63E-09	2.24E-09	6.597
f	71.2	319	0.54	3.82	1.53	1.18	15.0	6.8	1.53E-10	1.07E-09	6.608
g [b]	76.9	319	0.54	0.77	0.77	0.23	15.3	7.0	4.78E-09	5.77E-09	6.641
h	101.8	319	0.55	2.29	0.76	0.71	15.1	6.8	1.64E-10	1.79E-09	6.649
i	123.9	319	0.54	3.83	3.83	1.17	15.3	7.0	7.97E-11	1.14E-09	6.652
j	143.8	319	0.52	1.93	1.93	0.57	15.3	7.3	1.76E-09	2.64E-09	6.690
k [c]	152.8	320	0.53	3.85	1.54	1.15	15.2	7.2	5.86E-10	1.25E-09	6.701
l	192.1	320	0.52	7.72	1.54	2.28	15.3	7.3	1.77E-10	6.60E-10	6.714
m	200.2	319	0.49	1.96	1.96	0.54	15.6	7.9	2.31E-09	3.22E-09	6.744
n	215	320	0.49	3.91	3.91	1.09	15.7	7.9	2.54E-09	1.66E-09	6.794
o	224	320	0.49	7.81	1.56	2.19	15.7	7.9	8.81E-10	8.30E-10	6.813
p	241.5	319	0.49	15.6	3.91	4.37	15.8	8.0	7.40E-10	4.27E-10	6.841
q	270.9	319	0.49	23.4	3.91	6.56	15.8	8.0	1.21E-10	2.87E-10	6.850
r	289.5	319	0.49	46.9	3.91	13.1	15.7	8.1	3.27E-11	1.45E-10	6.852
s	311.3	319	0.49	11.7	3.90	3.30	15.7	8.0	7.10E-11	5.65E-10	6.855
t	316.3	320	0.32	12.4	4.14	2.59	16.5	11.1	9.66E-09	1.33E-09	6.957
u	320	319	0.35	24.6	4.10	5.37	16.5	10.7	2.99E-09	6.14E-10	6.983
v	334.4	319	0.37	48.9	4.08	11.1	16.8	10.5	1.35E-09	2.98E-10	7.037
w	347.5	319	0.42	96.3	9.63	23.7	16.8	9.7	4.65E-10	1.23E-10	7.054
x	368.1	320	0.42	241.0	9.64	59.0	16.9	9.8	2.09E-10	5.02E-11	7.065
y	383.7	319	0.41	401.9	9.65	98.1	16.8	9.9	1.26E-10	3.05E-11	7.071
z	408.5	319	0.42	804.3	9.65	195.7	17.1	9.9	1.43E-10	1.57E-11	7.083
aa	436.2	319	0.42	1206.2	9.65	293.8	17.2	10.0	7.73E-11	1.05E-11	7.090
1a	512.5	319	0.50	12	12	7200	17.2	8.6	2.72E-11	1.17E-12	7.106
1b	647.5	319	1.00	-	-	-	17.1	-	2.29E-13	-	7.107

[a] Simulated PWR water with 2 ppm Li and 1000 ppm B. Conductivity ~20 µS/cm.

[b] The CGR of the later part of the test period is reported.

[c] The CGR of the initial part of the test period is reported.

Fatigue pre-cracking was started at ~15 MPa $m^{1/2}$ with a triangle waveform of 1 Hz and a load ratio of 0.2. A CGR close to the fatigue growth rate in air was quickly established in this sample after about 1-hr cycling. After about 180-µm crack extension, the load ratio was increased in the next two test periods. The observed CGRs decreased as expected with the reduced contribution of mechanical fatigue (as shown in Fig. 28). However, the crack stalled in test period *f* after the triangle waveform was replaced with a saw-tooth waveform. After the crack was re-activated, several attempts were made to induce environmentally assisted cracking. The environmental effect became evident after a CGR of ~1.4 x 10^{-9} m/s was established in test period *v*. The load ratio and rise time were then increased simultaneously to stabilize the environmentally enhanced cracking. By the end of the cyclic loading test, the observed CGR in water was about a factor of seven higher than the fatigue growth rate in air. All cyclic CGRs obtained from this sample are plotted in Fig. 28 along with the corrosion fatigue curve for SSs in high-purity water with 0.2 ppm DO.

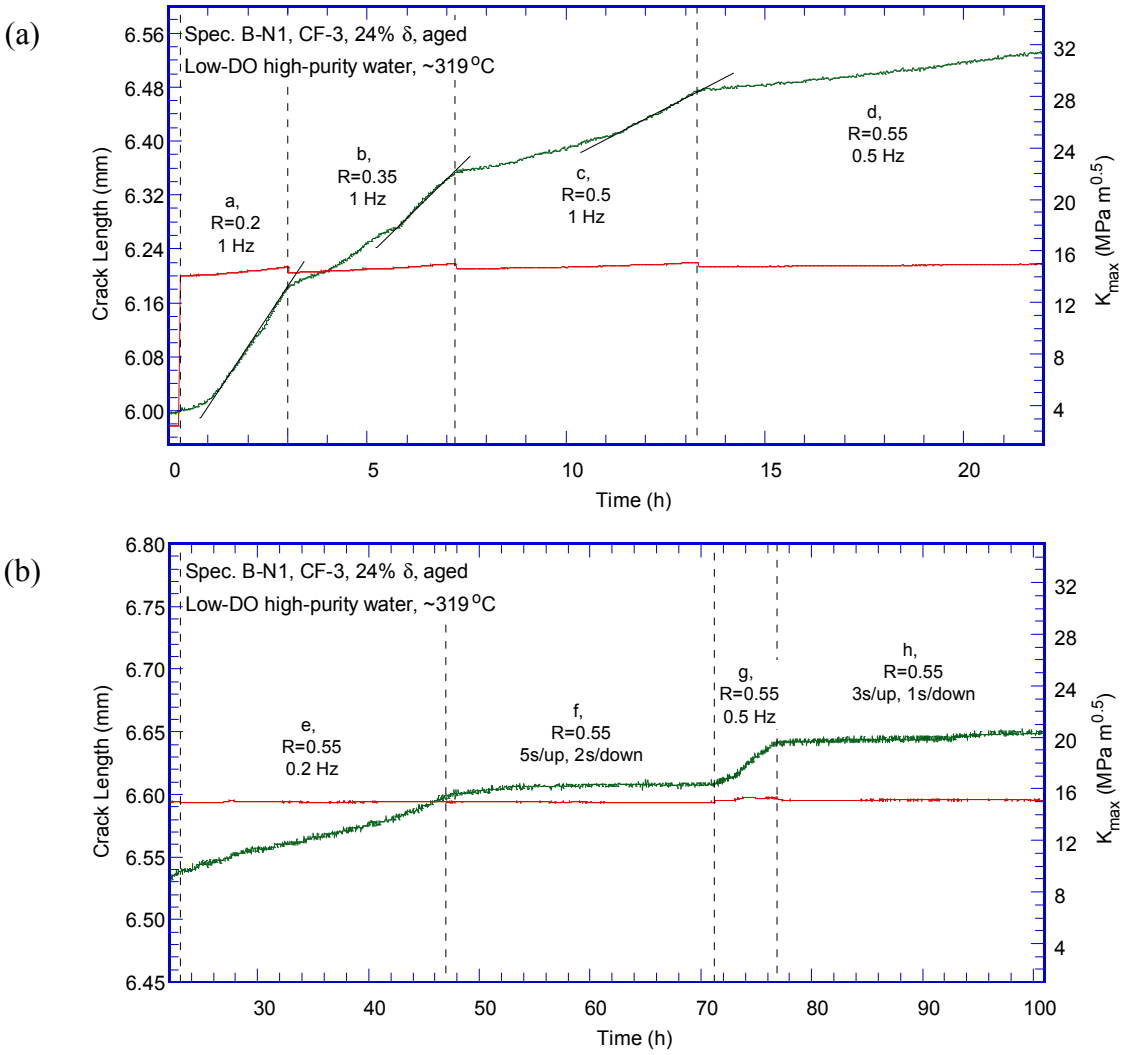

Figure 27. Crack-length-vs.-time plot for specimen B-N1 (unirradiated, aged CF-3 with 24% ferrite) in PWR water: test periods (a) a-d, (b) e-h, (c) i-n, (d) o-s, (e) t-w, (f) x-aa, and (g) 1a-1b.

(c)

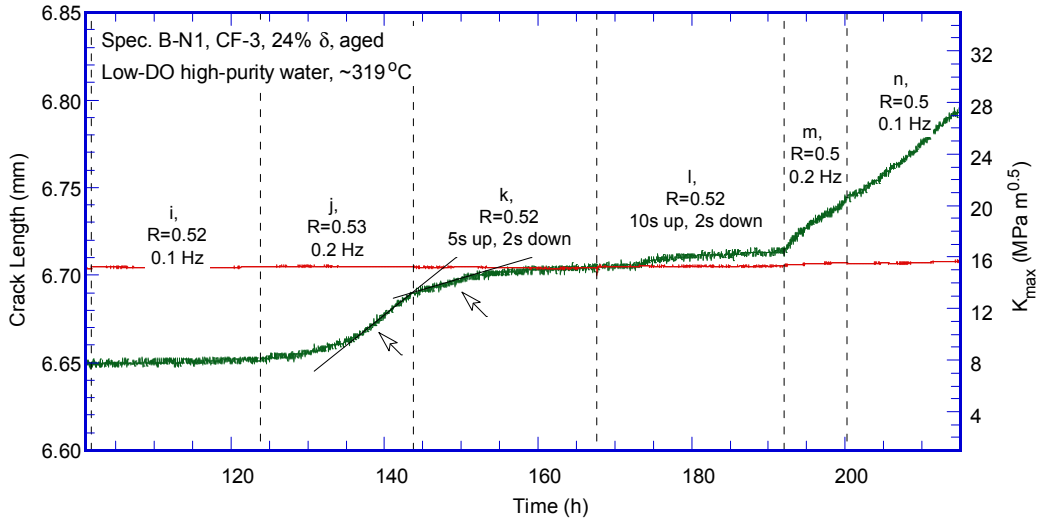

(d)

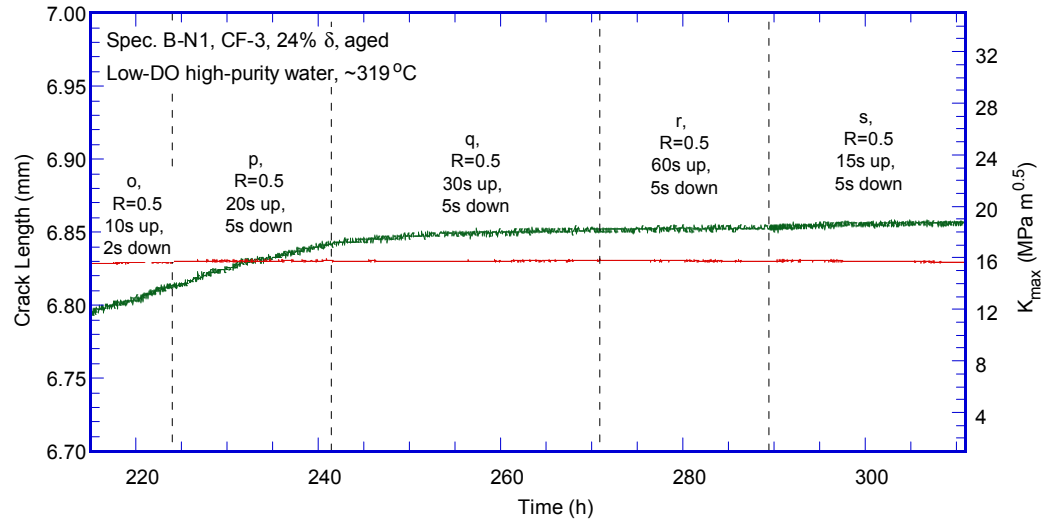

(e)

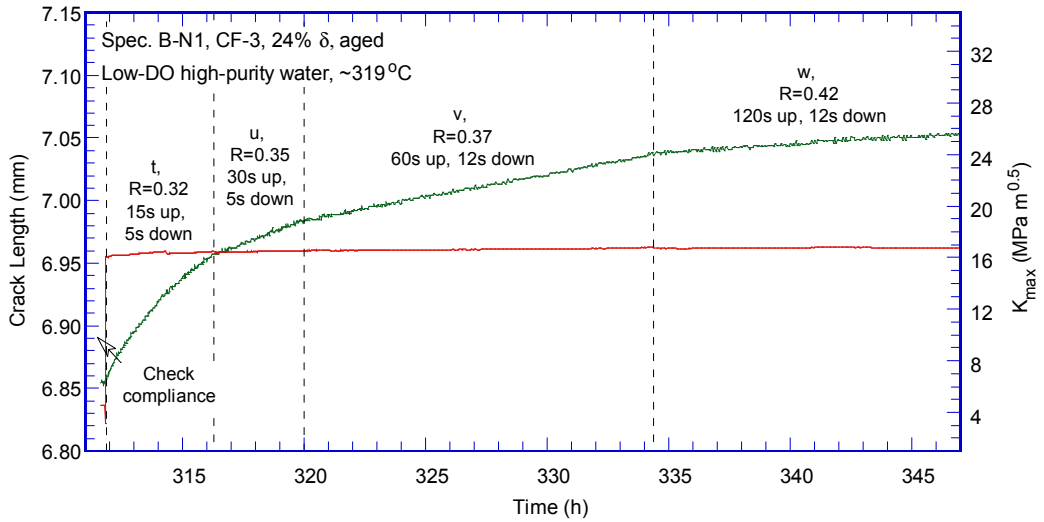

Figure 27. (Contd.)

(f)

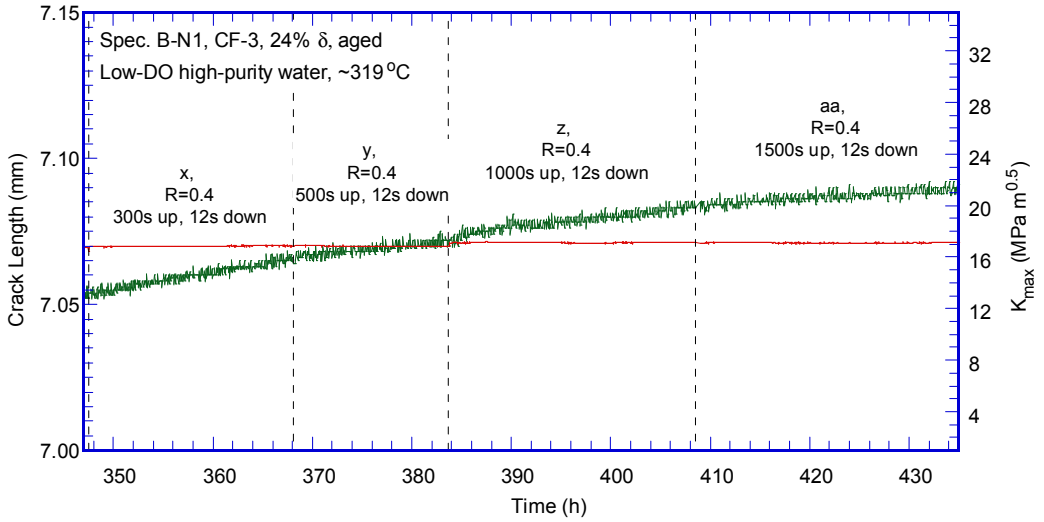

(g)

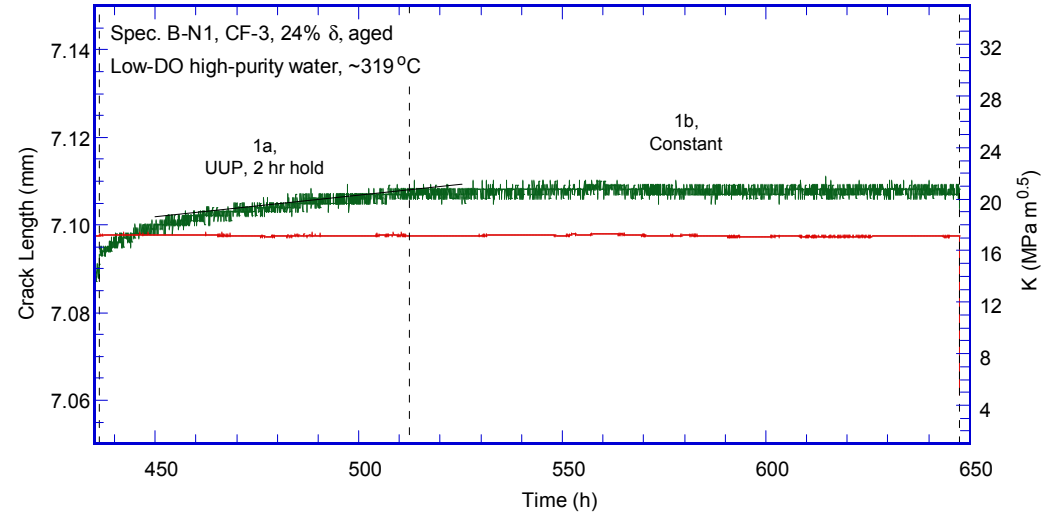

Figure 27. (Contd.)

After the environmentally assisted cracking was stabilized, the test was set to a constant stress intensity factor (~17 MPa $m^{1/2}$) with PPU every 2 hr. Following a short period of rapid growth, a CGR about 2.7 x 10^{-11} m/s was measured over 16-µm crack extension. Without PPU, the observed CGR dropped more than two orders of magnitude under a near constant-K condition. Limited by the test time, the CGR test was terminated after 135 hr with just 1-µm crack extension.

Fracture toughness J-R curve test

The fracture toughness J-R curve test was performed in the same PWR water environment. The test was conducted at a constant strain rate of 0.43 µm/s, and the crack extension was measured with the DCPD method. Before each DCPD measurement, the stress was allowed to relax for 30 s at a constant displacement. The obtained J-R curve is shown in Fig. 29. The estimated J

value at 0.2 mm offset line is about 170 kJ/m^2. Note that the J-R curve data cannot be validated for this test because the requirements of the crack straightness and J_{max} were not met.

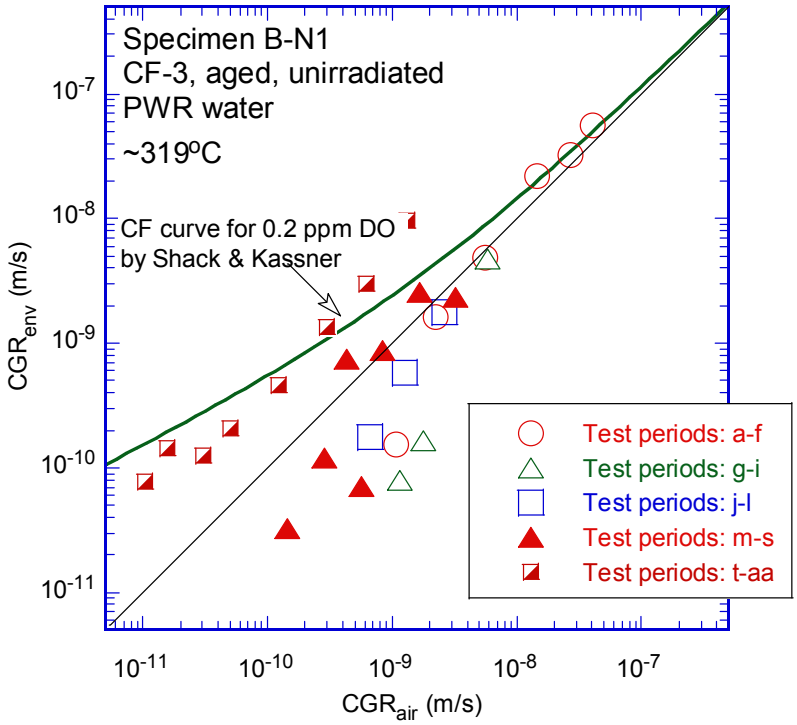

Figure 28. Cyclic CGRs of specimen B-N1.

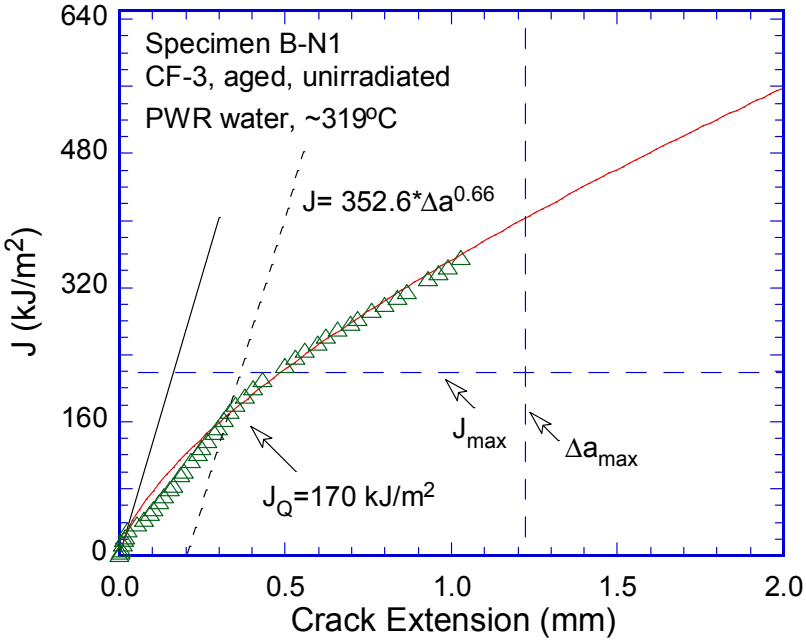

Figure 29. The J-R curve for specimen B-N1.

Fractographic examination

After the JR test, the sample was broken open at room temperature in air. The fracture surface of the tested sample was examined with SEM. Figure 30 is a global view of the entire fracture surface of the CGR and JR test regions. The crack front of the CGR test is quite straight, indicating a well-controlled loading condition. Figure 31 shows more details of the fracture along the central line of the specimen. The CGR test region shows a transganular morphology, and the JR test region is a ductile dimple fracture. A significant crack extension can be seen during the JR test, which is consistent with the low fracture resistance observed in this sample. In the CGR test region, the initial fracture close to the machined notch is characterized by coarse ledges resulting from fatigue fracture (Fig. 32), while at the later stage of the CGR test, the fracture surface is smoother (Fig. 33). Details of ductile dimple fracture in the JR test region can be seen in Fig. 34.

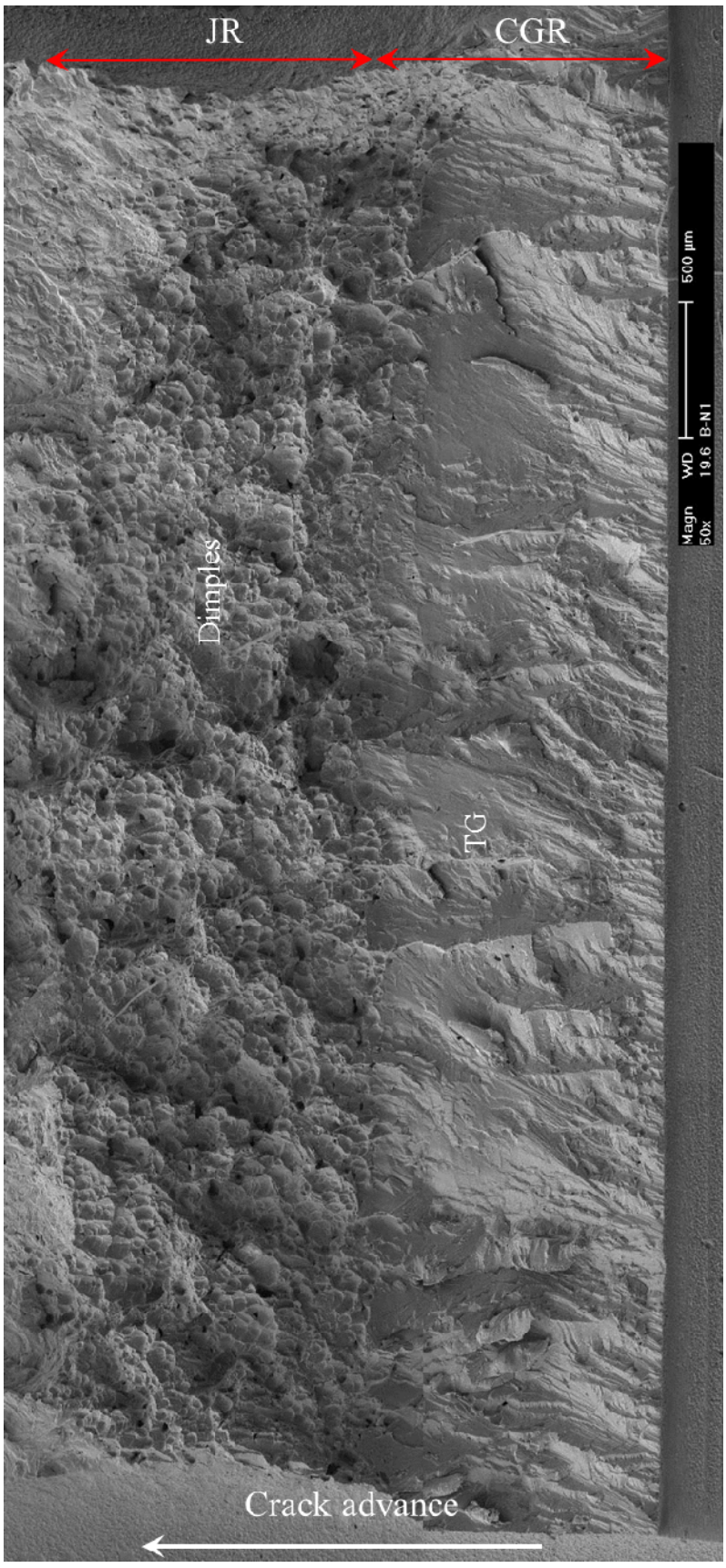

Figure 30. Fracture surface of specimen B-N1 tested in PWR water.

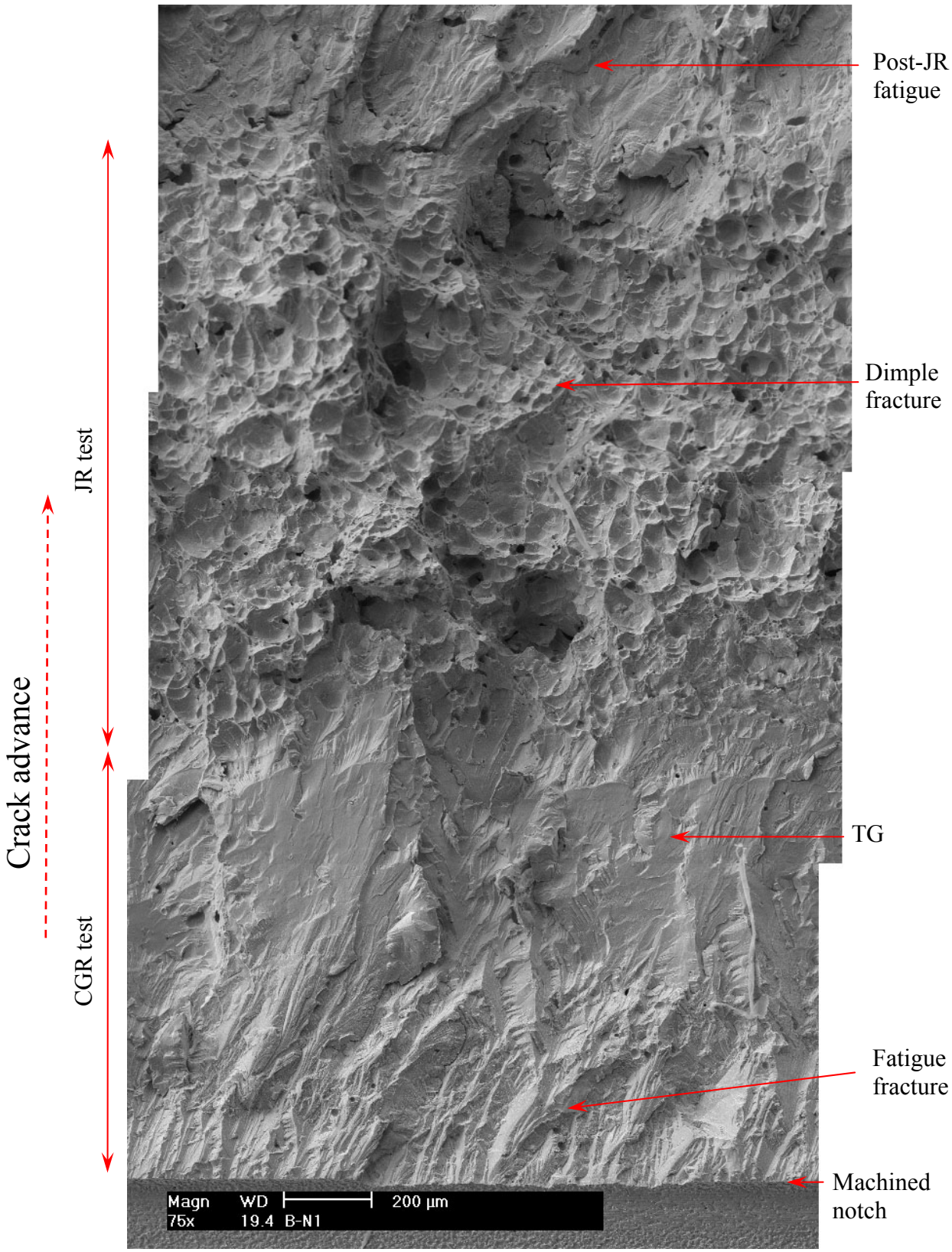

Figure 31. Fracture surface of specimen B-N1 along the sample central line.

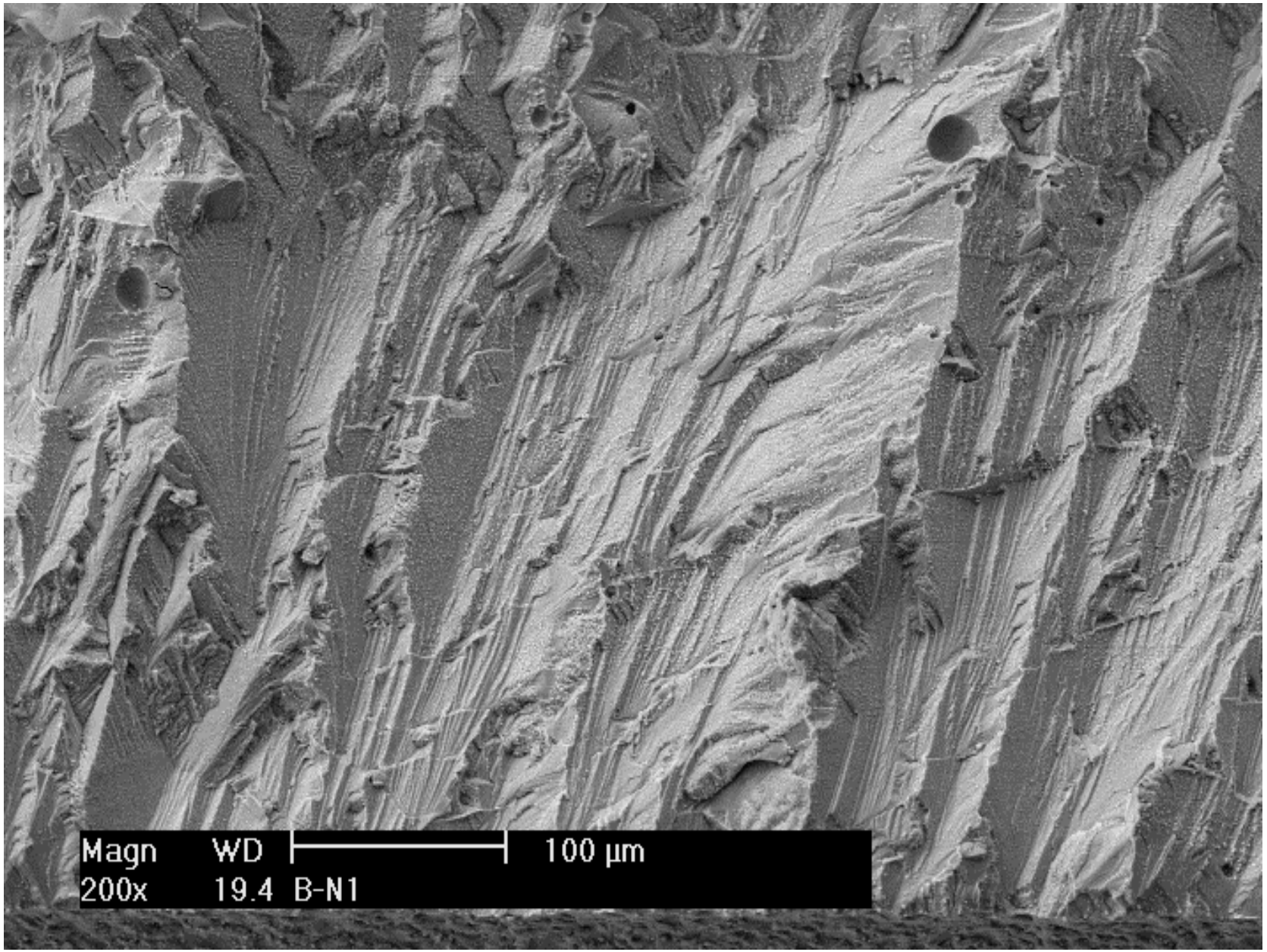

Figure 32. Transgranular fracture in specimen B-N1 at the beginning of the precracking. Crack propagation from bottom to top.

Field Co

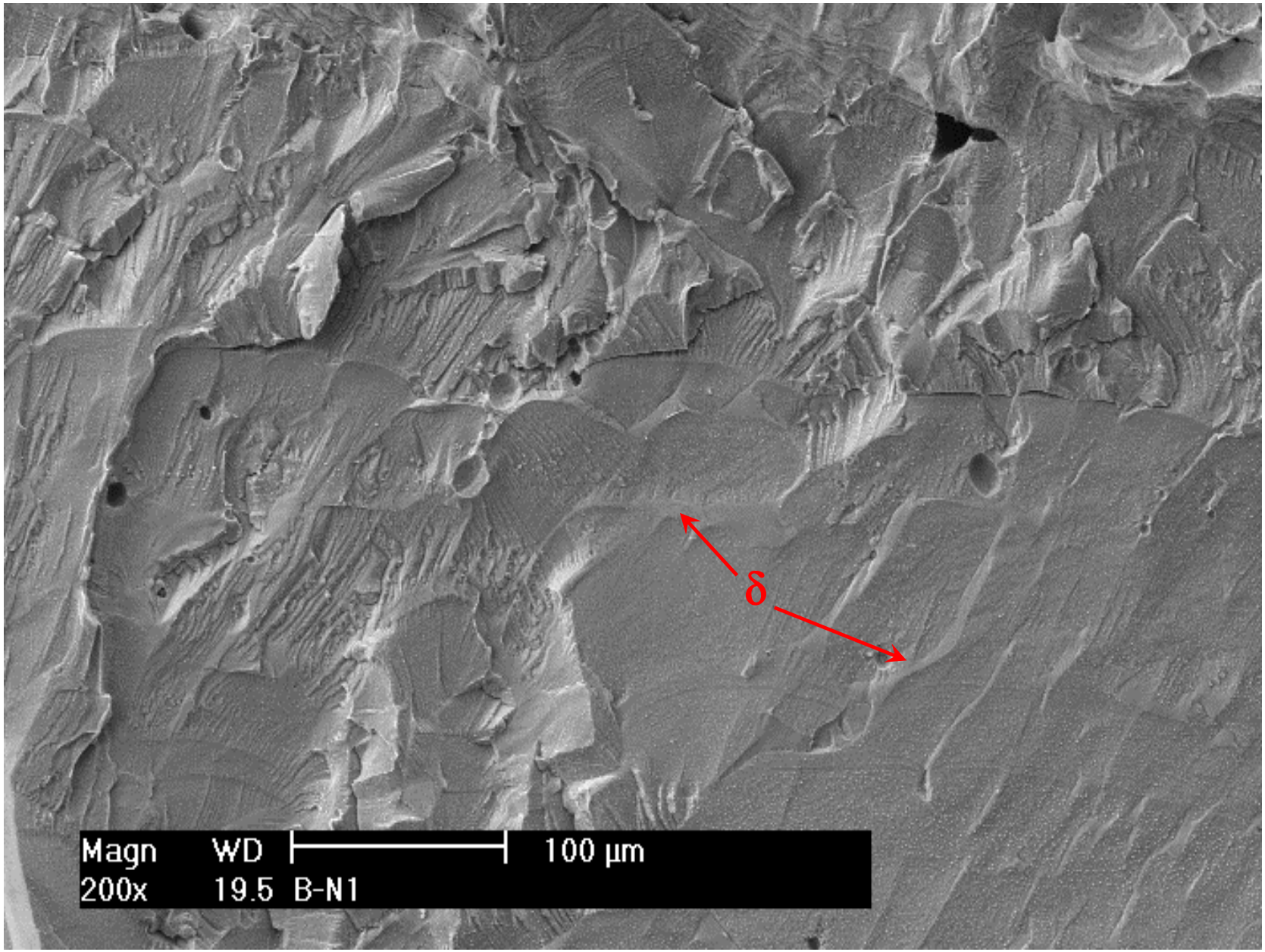

Figure 33. Transgranular fracture in specimen B-N1 at the end of the precracking. Crack propagation from bottom to top.

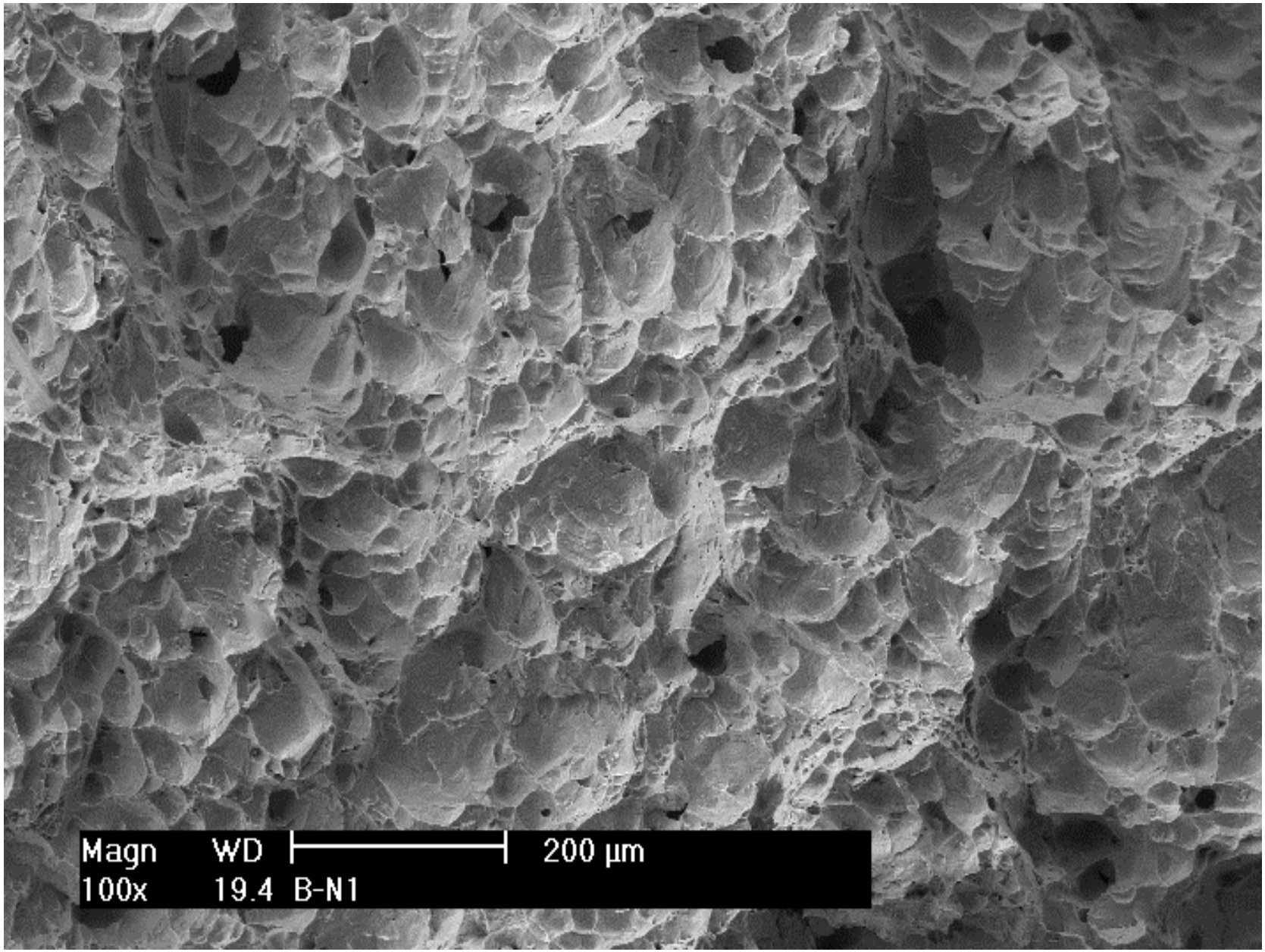

Figure 34. Ductile dimple fracture in the JR test region of specimen B-N1. Crack propagation from bottom to top.

3.1.2.2 Irradiated specimen B-1 tested in PWR water

Crack growth rate test

Specimen B-1 was a 0.08-dpa thermally aged CF-3 CASS with ~24% ferrite. This sample was obtained from the same heat (Heat 69) as specimens A-1 and A-2. The thermal aging condition was 400°C and 10,000 hr. The objective was to compare the results with those of the unaged CF-3 at the same dose level. The CGR test conditions and results are summarized in Table 8, and a crack-length history plot is shown in Fig. 35.

The test was started with fatigue pre-cracking at a maximum stress intensity factor of ~18 MPa $m^{1/2}$ and a load ratio of 0.3. A triangular waveform was used with a frequency of 1 Hz. Upon successful crack initiation, the maximum stress intensity factor was lowered to prepare for transitioning. In the following test periods, the load ratio and rise time were increased slowly to stimulate environmentally enhanced cracking. Despite the effort, the measured CGRs fell well below the fatigue growth rate line. A more aggressive loading condition was applied to re-activate the fatigue crack. Following that, repeated attempts (test periods *e-j*, *k-q*, and *r-af*) were made to induce environmental enhanced cracking. However, no elevated CGRs could be maintained. It appears that cracking cannot be sustained with a load ratio higher than 0.4 and a stress intensity factor less than 19 MPa $m^{1/2}$ in this sample. Environmentally enhanced cracking was only observed after increasing the stress intensity factor to about 22 MPa $m^{1/2}$. At this stress intensity, the measured CGR by the end of the cyclic test (period *ao*) was a factor of three higher than the fatigue crack growth rate in air. Subsequently, the test was set at constant load with PPU every 2 hr in test period *1*. A CGR of 2.8×10^{-11} m/s was obtained at a stress intensity factor of 22 MPa $m^{1/2}$.

Table 8. CGR test of specimen B-1 (0.08-dpa aged CF-3 with 24% δ ferrite) in PWR water.[a]

Test Period	Test Time, h	Test Temp., °C	Load Ratio	Rise Time, s	Return Time, s	Hold Time, s	Kmax, MPa $m^{1/2}$	ΔK, MPa $m^{1/2}$	CGR in Env., m/s	CGR in Air, m/s	Crack Length, mm
Start	0.52										6.019
a	3.0	319	0.27	0.38	0.38	0.12	17.6	12.8	7.88E-08	6.55E-08	6.250
b	6.7	320	0.39	0.35	0.35	0.15	17.0	10.4	4.11E-08	4.06E-08	6.442
c	10.5	320	0.50	0.64	0.64	0.36	15.8	7.9	2.75E-09	9.97E-09	6.460
d	20.1	320	0.45	1.32	1.32	0.68	15.9	8.8	3.63E-10	6.50E-09	6.466
e	23.3	320	0.27	0.37	0.37	0.13	17.9	13.1	5.89E-08	7.29E-08	6.698
f	25.4	320	0.27	0.36	0.36	0.14	17.1	12.4	4.86E-08	6.25E-08	6.822
g	27.8	320	0.38	0.34	0.34	0.16	16.8	10.4	2.77E-08	4.22E-08	6.905
h	32.2	320	0.38	0.66	0.66	0.34	16.3	10.1	8.33E-09	1.93E-08	6.950
i	44.2	319	0.44	3.20	3.20	1.80	16.2	9.2	2.63E-10	3.07E-09	6.955
j	47.5	320	0.38	1.32	1.32	0.68	16.2	10.0	7.00E-10	9.49E-09	6.958
k[b]	52.3	320	0.37	0.67	0.67	0.33	17.1	10.8	1.01E-08	2.32E-08	7.000
l	59.1	320	0.37	3.36	1.34	1.64	17.2	10.9	4.05E-09	4.80E-09	7.048
m	69	320	0.37	6.71	1.34	3.29	17.4	11.0	2.24E-09	2.48E-09	7.092
n	82.8	320	0.42	13.0	3.25	6.99	17.3	10.1	3.18E-10	1.01E-09	7.102
o	95.2	320	0.36	13.4	3.35	6.60	17.3	11.0	4.09E-11	1.23E-09	7.104
p	105	320	0.36	6.73	3.37	3.27	17.5	11.2	1.01E-10	2.59E-09	7.107
q	116.8	320	0.36	13.6	3.40	6.41	17.8	11.5	9.16E-11	1.40E-09	7.107
r	124.2	320	0.36	1.36	1.36	0.64	18.0	11.5	3.85E-09	1.43E-08	7.142
s	130.6	320	0.36	3.39	1.36	1.61	18.1	11.6	2.66E-09	5.86E-09	7.171
t	142.5	320	0.36	6.77	1.35	3.23	18.2	11.7	1.21E-09	3.00E-09	7.201
u	145.9	319	0.35	13.5	3.38	6.46	18.1	11.7	9.45E-11	1.49E-09	7.202
v	164.7	319	0.35	13.6	3.40	6.40	18.3	11.9	1.23E-10	1.56E-09	7.207
w	170	319	0.35	10.2	3.40	4.80	18.4	11.9	1.53E-10	2.09E-09	7.208
x	188.7	319	0.35	10.2	3.42	4.75	18.9	12.3	1.39E-09	2.28E-09	7.251
y	199	319	0.35	20.5	3.42	9.51	18.9	12.3	7.57E-10	1.15E-09	7.265
z	238	319	0.35	41.0	3.41	19.0	19.1	12.3	2.14E-10	5.88E-10	7.287
aa	284.5	319	0.36	81.8	8.18	38.2	19.3	12.4	2.61E-10	3.00E-10	7.318
ab	356.3	319	0.35	204.4	8.18	95.6	19.2	12.4	4.36E-11	1.20E-10	7.325
ac	442.2	318	0.35	413.0	8.26	187.0	19.9	12.9	2.88E-11	6.65E-11	7.331
ad	501.5	319	0.35	693.0	8.32	307.0	20.2	13.2	1.41E-11	4.26E-11	7.334
ae	527.8	318	0.46	78.0	7.80	42.0	19.9	10.8	5.94E-12	2.23E-10	7.336
af	574.5	318	0.45	39.4	7.88	20.6	20.6	11.3	2.11E-10	4.98E-10	7.356
ag	644.4	318	0.45	78.8	7.88	41.2	20.6	11.2	negligible	2.48E-10	7.355
ah	648	318	0.29	3.97	3.97	1.03	22.5	15.9	2.93E-08	1.30E-08	7.477
ai	650	318	0.34	11.7	3.89	3.32	22.3	14.7	7.43E-09	3.61E-09	7.509
aj	653.2	318	0.41	22.6	3.76	7.43	21.5	12.8	2.97E-09	1.27E-09	7.532
ak	671.3	318	0.39	45.8	9.16	14.2	22.6	13.8	1.02E-09	7.91E-10	7.577
al	693.8	318	0.39	91.5	9.15	28.5	22.8	14.0	7.29E-10	4.09E-10	7.618
am	717	318	0.46	194.0	7.76	106.0	22.1	11.9	4.90E-10	1.22E-10	7.644
an	747.7	319	0.46	387.7	7.75	212.3	22.0	11.9	1.66E-10	6.16E-11	7.655
ao	788.7	319	0.46	645.4	7.74	354.6	22.1	11.9	1.20E-10	3.71E-11	7.667
1	837.5	318	0.40	12	12	7200	22.1	13.3	2.81E-11	4.42E-12	7.675

[a] Simulated PWR water with 2 ppm Li and 1000 ppm B. Conductivity ~20 µS/cm.

[b] The CGR value was obtained from the later part of the test period.

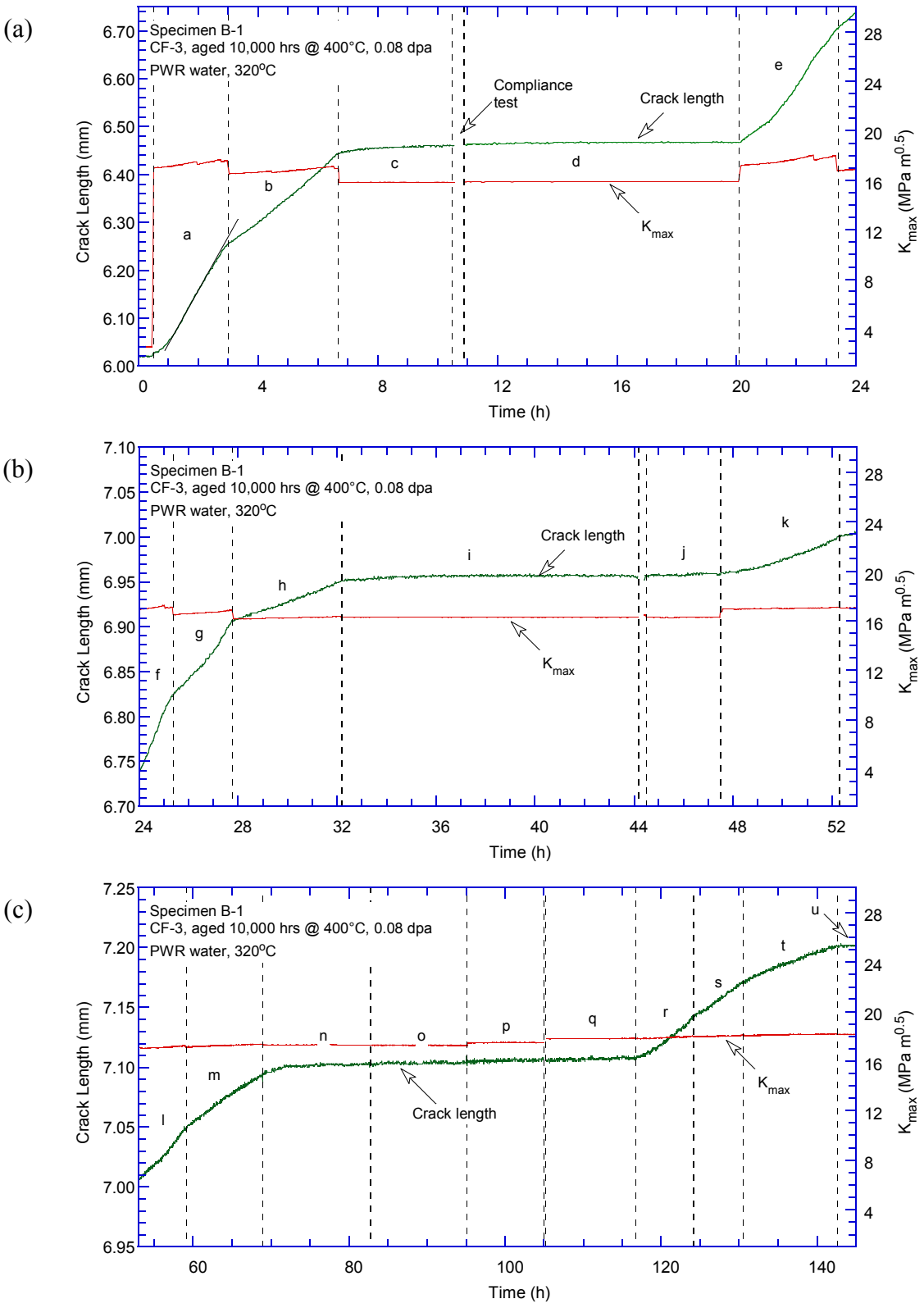

Figure 35. Crack-length-vs.-time plot for specimen B-1 (0.08-dpa aged CF-3 with 24% ferrite) in PWR water: test periods (a) a-e, (b) f-k, (c) l-u, (d) v-y, (e) z-ac, (f) ad-ag, (g) ah-al, and (h) am-1.

(d)

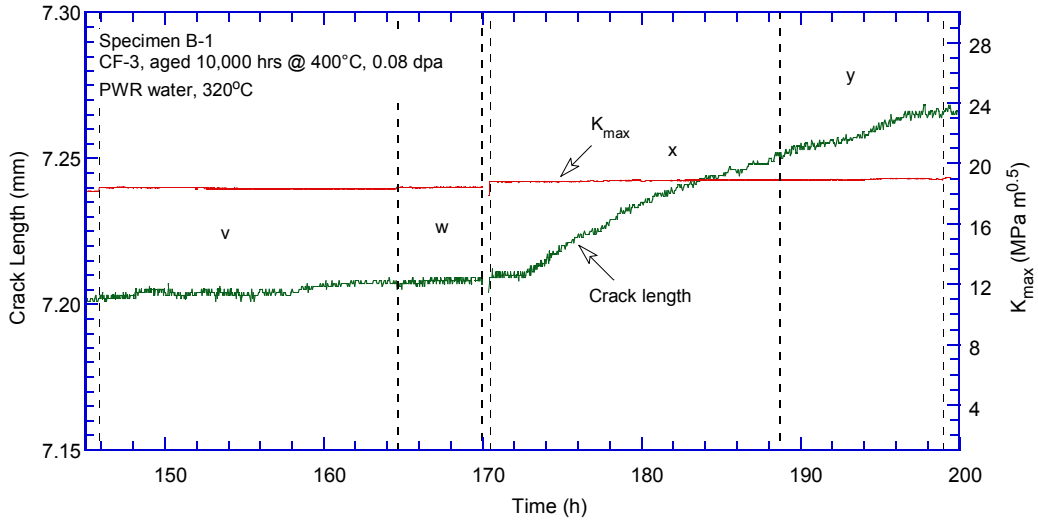

(e)

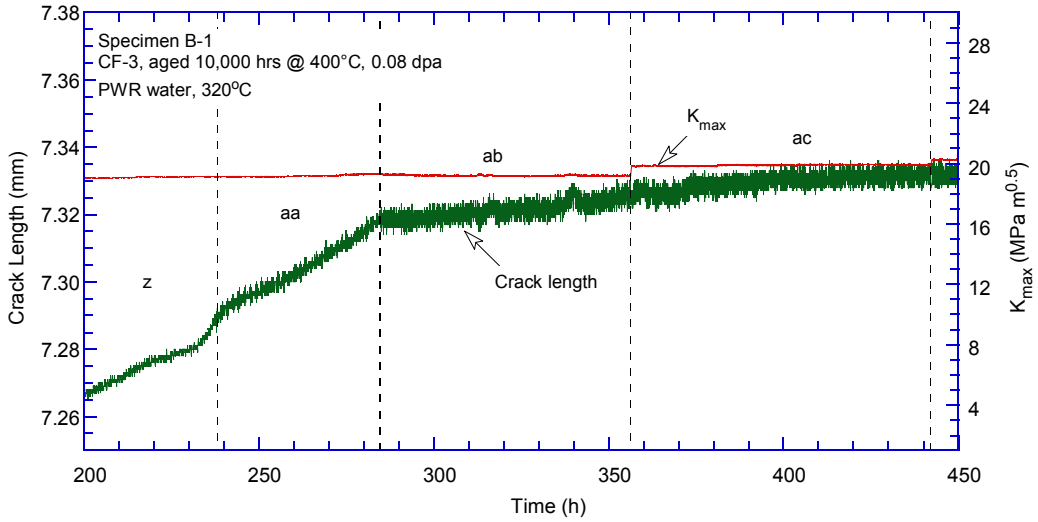

(f)

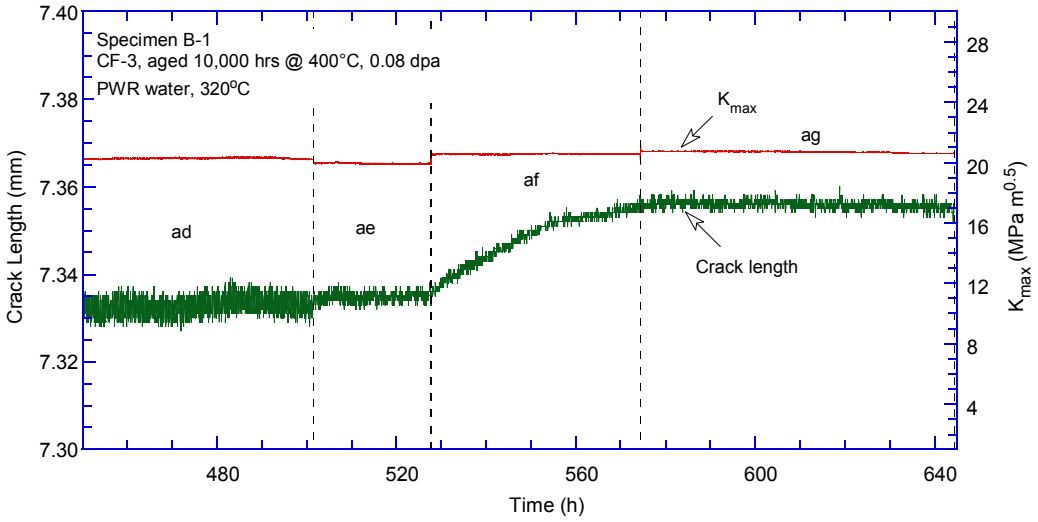

Figure 35. (Contd.)

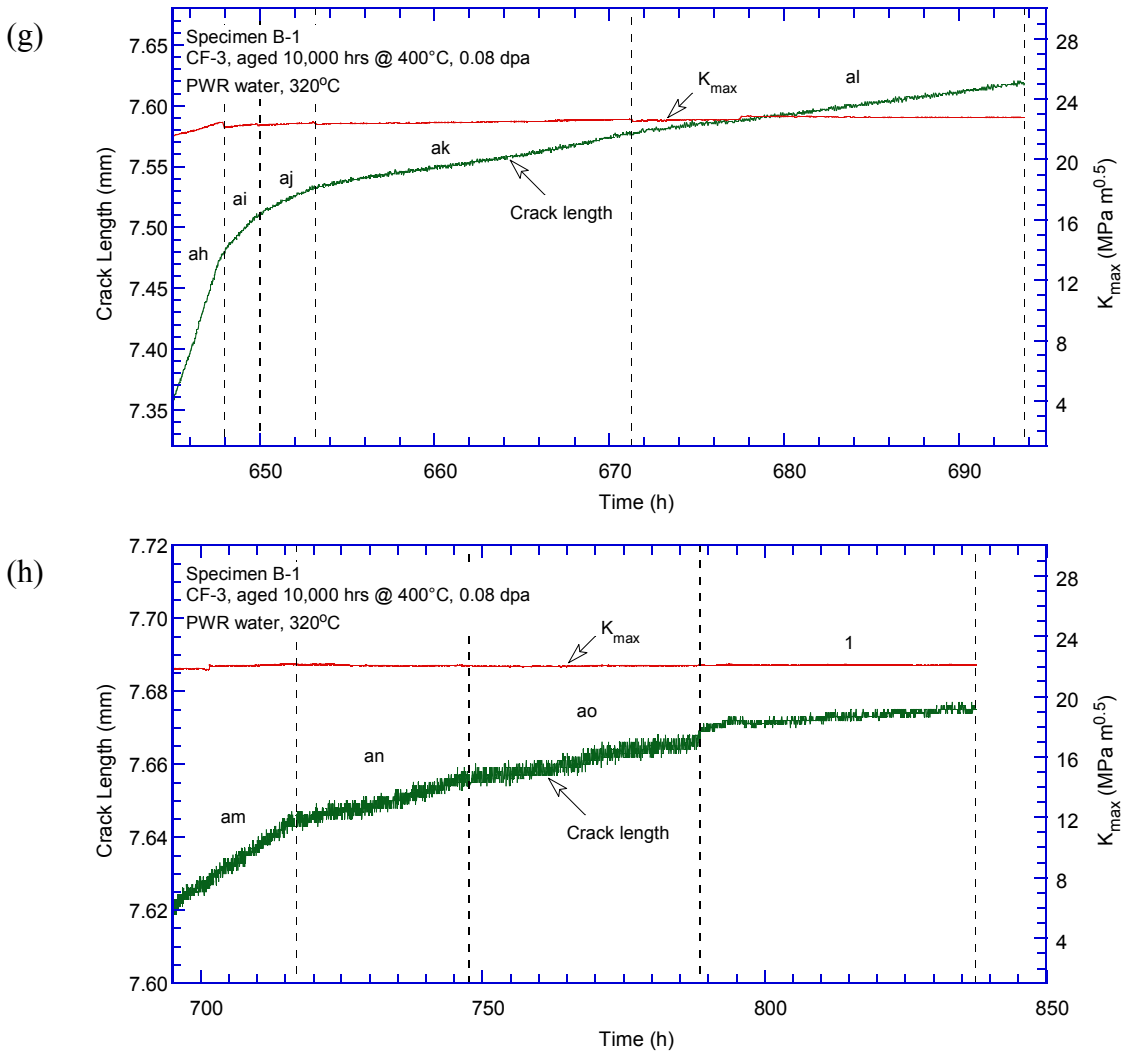

Figure 35. (Contd.)

The cyclic CGRs with a significant crack extension (defined as >10 μm) from this sample are plotted in Fig. 36 along with the corrosion fatigue curve for unirradiated SSs. No elevated corrosion fatigue response can be seen for this material despite its thermal aging condition. Comparing Figs. 14 and 36, we found the corrosion fatigue behaviors of unaged and aged CF-3 to be similar in PWR water. It seems that a combination of irradiation damage and thermal aging does not increase cracking susceptibility of CF-3 at 0.08 dpa, as would be expected.

All SCC CGRs obtained from specimens A-N1, A-1, A-2, B-N1, and B-1 are shown in Fig. 37. The open and closed symbols are for the unaged and thermally aged CF-3, and the blue and red symbols are for the unirradiated and irradiated specimens, respectively. The data points are all well below the NUREG-0313 curve, as expected in such low-corrosion-potential environments. No obvious difference can be seen between the unirradiated and irradiated specimens. The SCC CGRs of the unaged CF-3 (specimens A-1 and A-2) are also similar for the low-DO high-purity water and PWR water environments. The thermally aged specimen (B-1) has a slightly lower

CGR than that of unaged CF-3. However, given the large scatter of the SCC CGR data, this difference is considered insignificant.

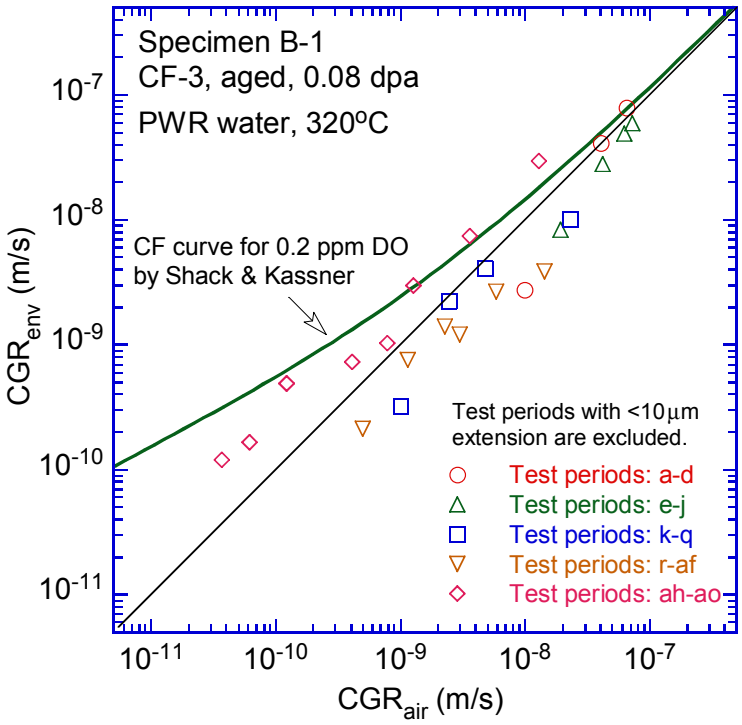

Figure 36. Cyclic CGRs of specimen B-1.

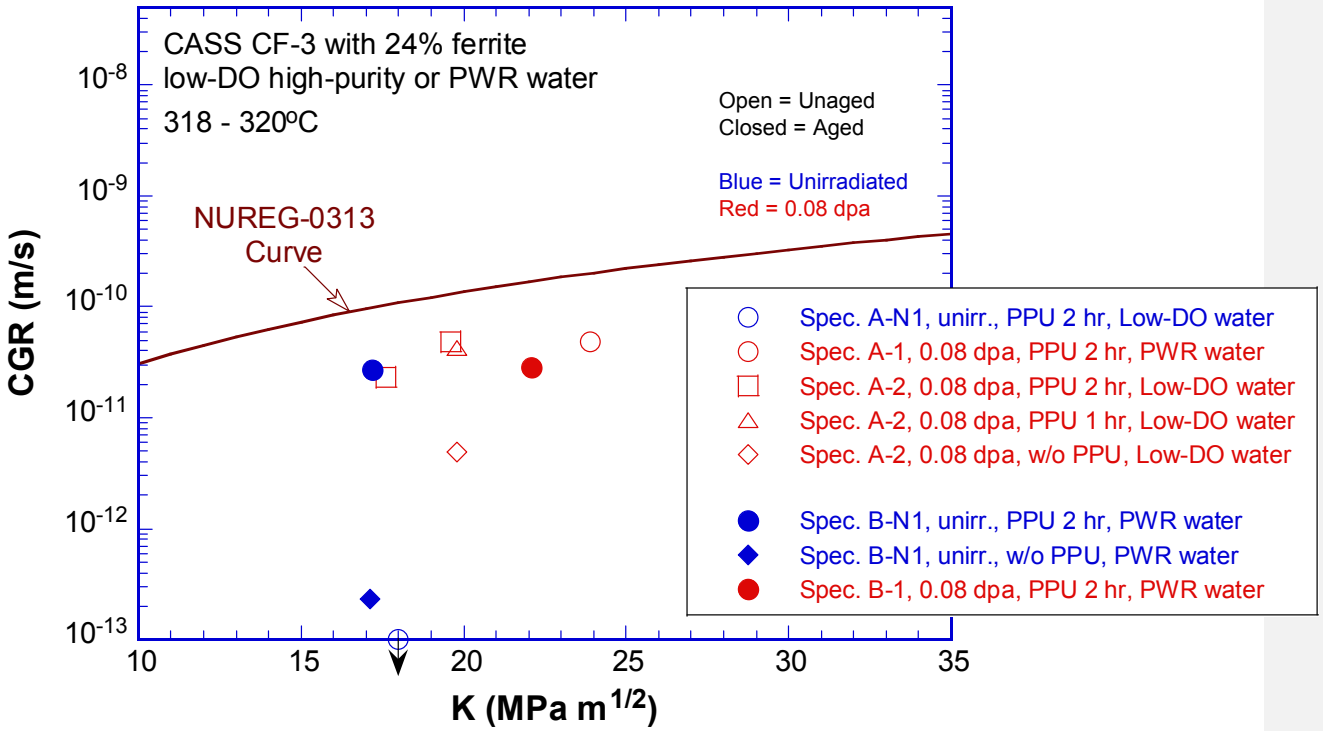

Figure 37. SCC CGRs of unaged and thermally aged CF-3 with 24% ferrite.

Fracture toughness J-R curve test

After the CGR test, a fracture toughness J-R curve test was conducted on the same sample at 320°C in PWR water. The obtained J-R curve is shown in Fig. 38. A power-law fitting of the JR data gives a relationship of $J = 362\Delta a^{0.85}$. The estimated J value is about 116kJ/m^2 at the 0.2-mm offset line. The J-R curve data cannot be validated with the ASTM standard because both measurements of the initial and final crack size did not meet the requirements. The data points above the J_{max} limit were also used in the analysis.

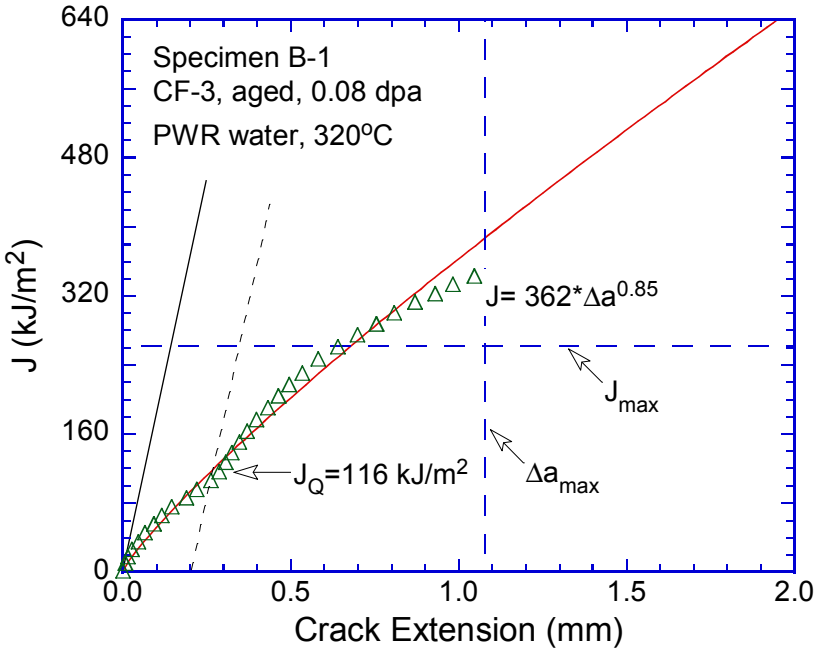

Figure 38. The J-R curve for specimen B-1.

Fractographic examination

Fractographic analysis of specimen B-1 was carried out with replicas, and Fig. 39 shows the entire fracture surface. Transgranular cleavage-like cracking is the dominant fracture morphology in the CGR test region. The overall crack extension for the CGR test is a little more on one side of the sample than the other, leading to a slightly skewed crack front. Figure 40 shows an enlarged view of the fracture surface along the sample central line. The CGR and JR test regions can be clearly distinguished by their appearance. The CGR region is relatively flat, and the JR region indicates heavily deformed ductile tearing. Note that air bubbles trapped in the replica are more excessive in the JR test region, a rough and dimpled fracture surface, than the flat CGR test region. Casting dendrite morphology with ferrite cores was seen at the end of the CGR test.

Cleavage-like morphology dominated the fatigue pre-cracking region, as shown in Fig. 41. Deformation steps are clearly visible on the fracture surface. With the advance of the crack, an area with delta ferrite at dendrite cores started to appear (Fig. 42). Compared with the surrounding austenitic phase, fewer deformation steps can be seen within the ferrite phase, as shown in Fig. 43.

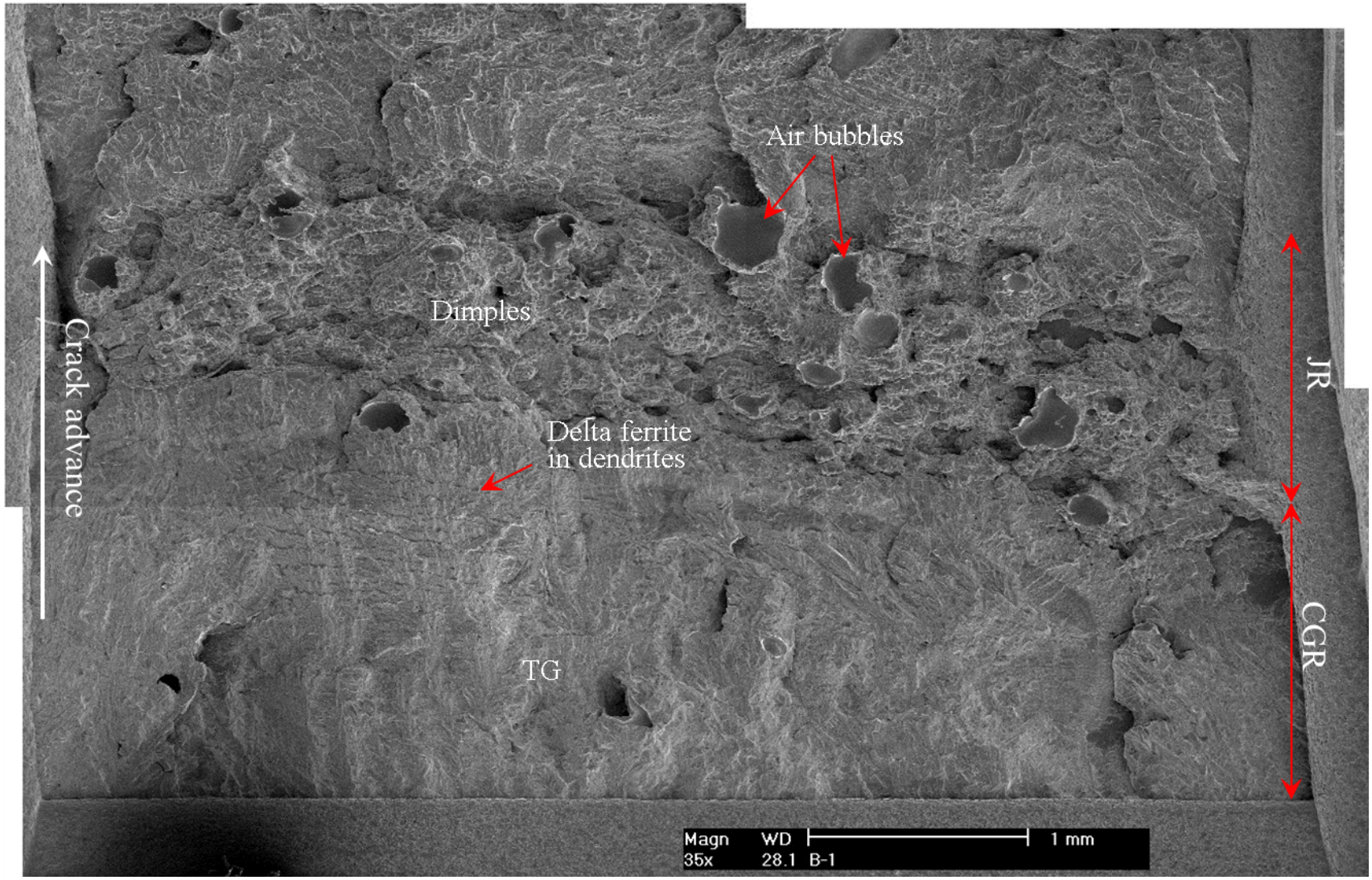

Figure 39. Fracture surface of specimen B-1 tested in PWR water.

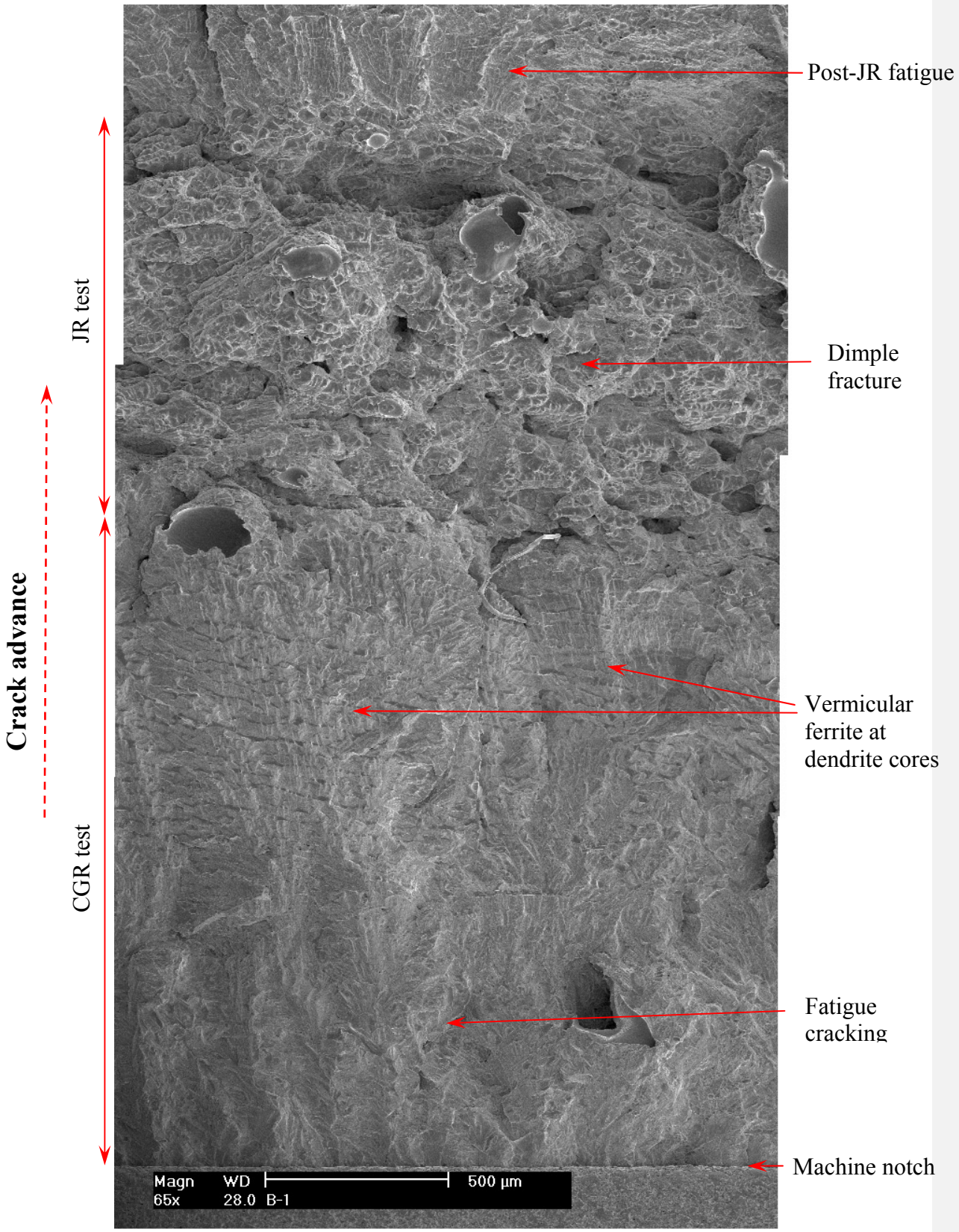

Figure 40. Fracture surface of specimen B-1 along the sample central line.

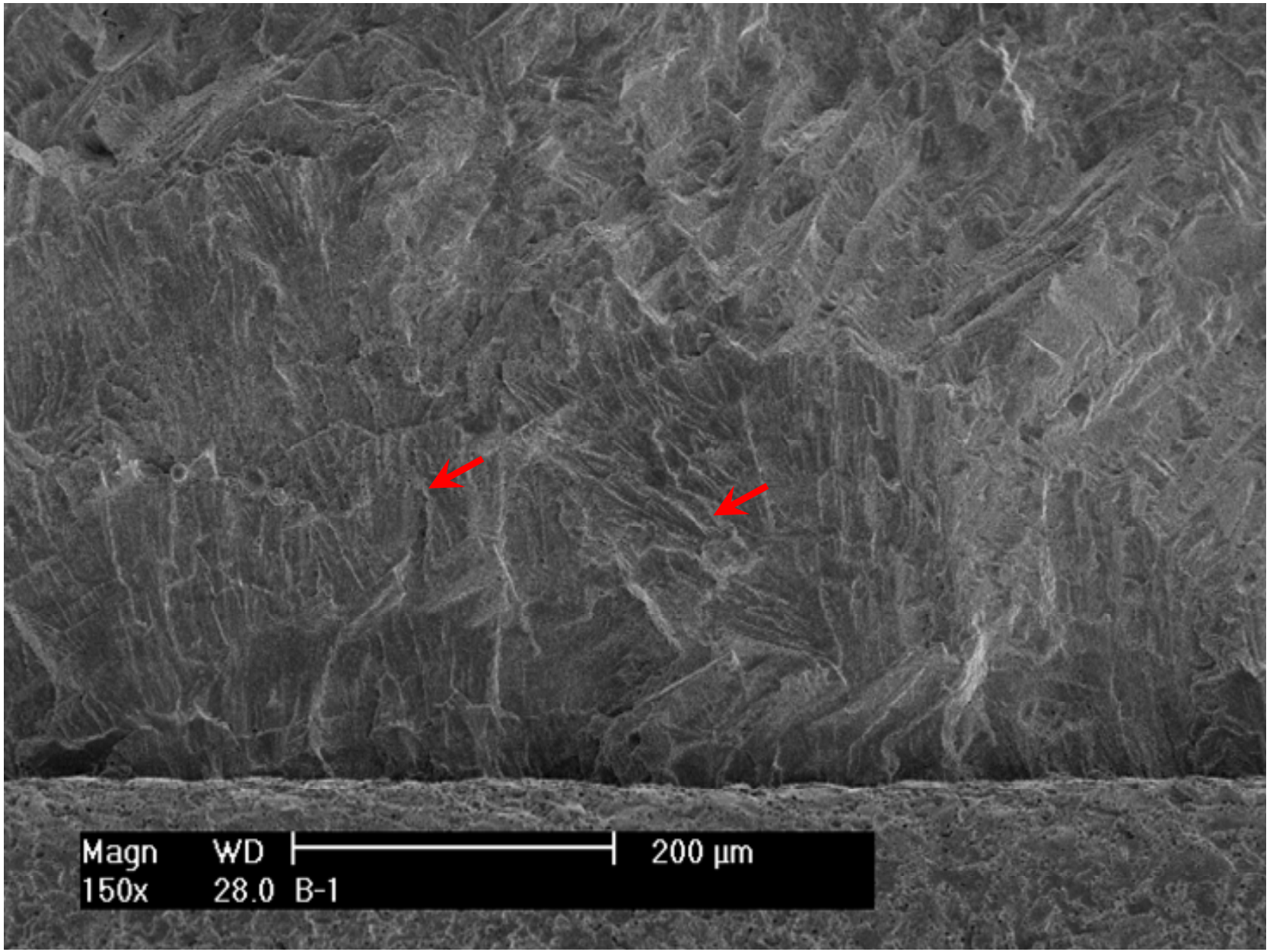

Figure 41. Deformation steps in the pre-cracking region of specimen B-1. Crack propagation from bottom to top.

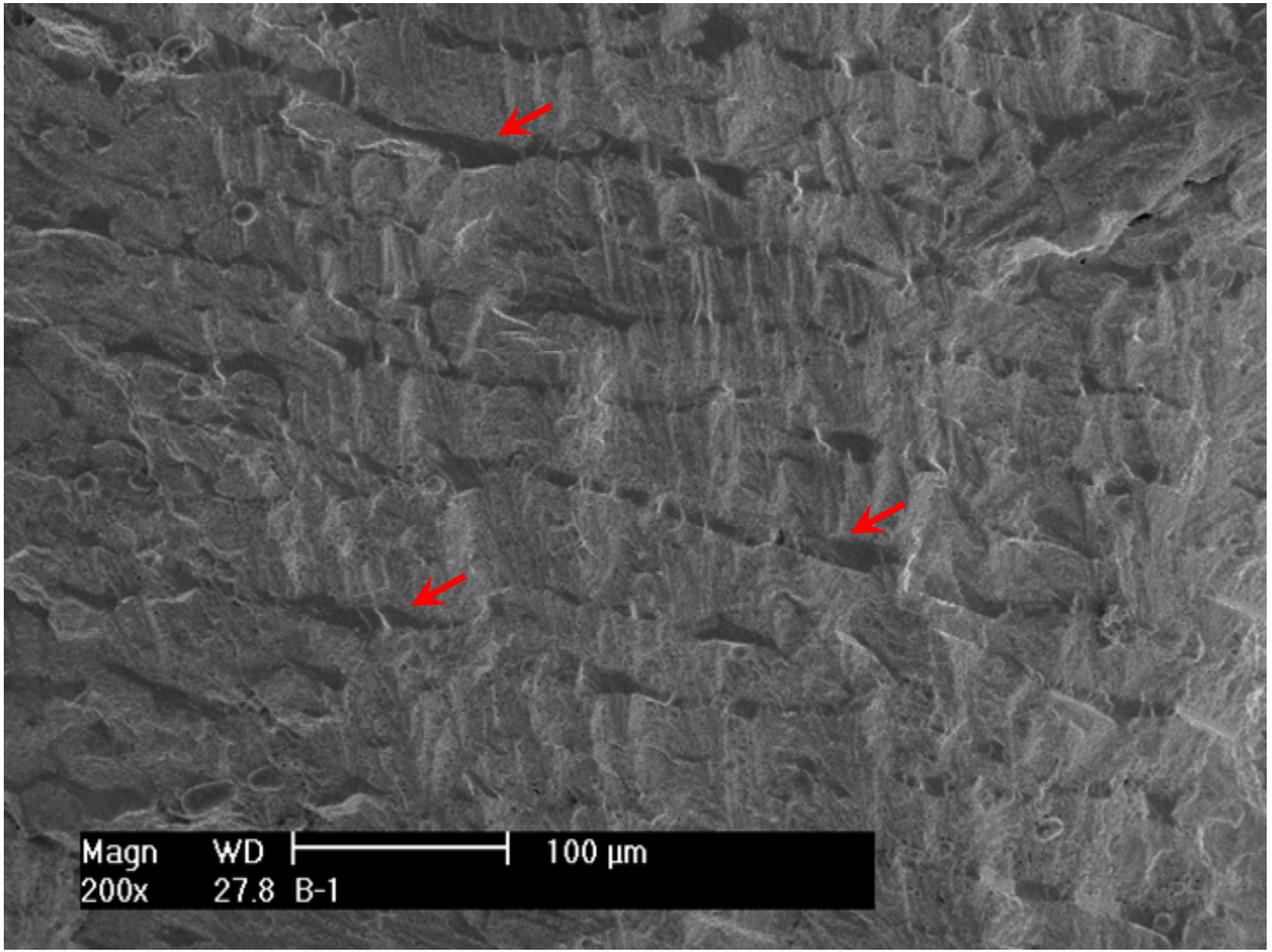

Figure 42. Delta ferrite at dendrite cores in specimen B-1. Crack propagation from bottom to top.

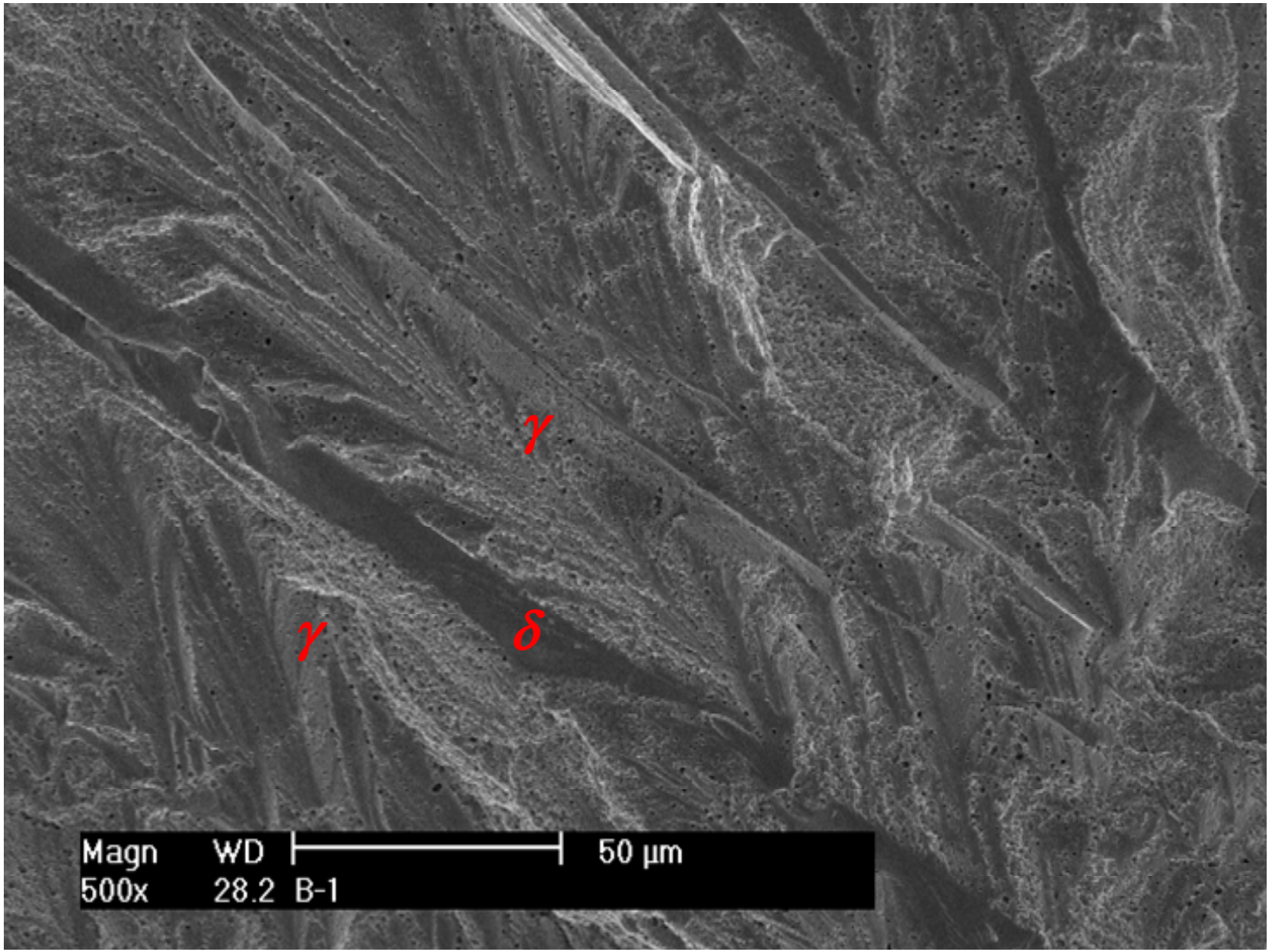

Figure 43. Fracture surface of specimen B-1 showing that delta ferrite is surrounded by heavily deformed austenite phase. Crack propagation from bottom to top.

Field Co